

Rogue Wave Impact on Marine Structures

von
Diplom-Ingenieur
Christian E. Schmittner
aus Berlin

von der Fakultät V – Verkehrs- und Maschinensysteme
der Technischen Universität Berlin
zur Erlangung des akademischen Grades

Doktor der Ingenieurwissenschaften
– Dr.-Ing. –

genehmigte Dissertation

Promotionsausschuss:

Vorsitzender: Prof. Dr.-Ing. Wolfgang Nitsche
Berichter: Prof. Dr.-Ing. Günther F. Clauss
Berichter: Prof. Dr.-Ing. Paul Uwe Thamsen

Tag der wissenschaftlichen Aussprache: 2. Dezember 2005

Berlin 2005

D 83

Abstract

In this work, the mystery of Rogue Waves is revealed and the impact of these waves on marine structures is investigated. The aim of this thesis is the development and application of methods for the analysis of Rogue Wave impacts. Examples of recorded Rogue Waves are given and the frequency of occurrence is examined by analyzing a five day storm measured in the North Sea.

For the realization of deterministic Rogue Waves scenarios in the model basin a *linear optimization* approach is proposed, synthesizing extreme wave sequences based on predefined parameters. In order to improve the accuracy of the generated wave sequences an *experimental optimization* method is introduced fitting the wave sequences measured in the wave basin precisely to the target parameter.

Resultant wave environments of the optimizations are applied for the analysis of Rogue Wave impacts on different marine structures. In particular, the motions and bending moments of an FPSO and of a crane vessel as well as the motions and splitting forces of a semisubmersible due to Rogue Waves are investigated. The *New Year Wave*, a Rogue Wave that was recorded at the *Draupner* platform located in the North Sea, is realized at model scale and varied in experiment with respect to the local wave height and period. The responses of the structures are assessed by numerical simulations applying state of the art ship motion codes and model test. Resultant motions and structural responses are compared to frequency-domain methods for design and to rules from classification societies and discussed with regard to their applicability to Rogue Wave impacts.

For the precise numerical simulation of nonlinear wave propagation, numerical wave tanks based on potential theory and on the Navier-Stokes equations are presented. A new coupling approach for the fast and accurate simulation of nonlinear wave evolution is proposed, combining the advantages of two different numerical strategies.

Zusammenfassung

In der vorliegenden Arbeit wird dem Mysterium so genannter Rogue Waves, zu deutsch "Schurkenwellen", auf den Grund gegangen und die Wirkung dieser Wellen auf Offshore-Strukturen untersucht. Das Ziel der Arbeit ist es, Verfahren zur Analyse der Auswirkungen von Rogue Waves zu entwickeln und anzuwenden. Es werden Beispiele gemessener Rogue Waves präsentiert und ihre Auftrittshäufigkeit durch die Analyse eines fünftägigen Sturms in der Nordsee untersucht.

Für die Realisierung von deterministischen Rogue Waves im Wellenkanal wird eine *lineare Optimierung* vorgestellt, mit der es möglich ist, extreme Wellensequenzen unter Einhaltung vordefinierter Parameter zu synthetisieren. Zur Verbesserung der Genauigkeit dieser Wellensequenzen wird eine *experimentelle Optimierung* entwickelt und angewandt, welche die im Wellenkanal gemessenen Wellen an die Zielparameter anpasst.

Die so erzeugten Wellenszenarien werden für die Untersuchung der Wirkung von Rogue Waves auf verschiedene maritime Strukturen eingesetzt. Es werden die Bewegungen und Biegemomente eines FPSOs und eines Kranschiffs sowie die Bewegungen und Splitting Forces einer Halbtaucherplattform untersucht. Die *New Year Wave*, eine an der *Draupner* Plattform in der Nordsee gemessene Rogue Wave, wird im Modellmaßstab realisiert. Zudem werden die lokalen Eigenschaften Wellenhöhe und Wellenperiode dieser Extremwelle im Versuch variiert. Die daraus resultierenden Bewegungen und strukturellen Belastungen werden sowohl gemessen als auch mit Programmen zur Seegangssimulation berechnet. Die Ergebnisse werden mit gängigen Frequenzbereichsverfahren für den Entwurf und mit Bauvorschriften verglichen, um festzustellen, ob diese auf Rogue Wave impacts anwendbar sind.

Für die präzise numerische Berechnung der nichtlinearen Wellenausbreitung, werden numerische Wellenkanäle basierend auf der Potentialtheorie und den Navier-Stokes Gleichungen vorgestellt. Eine neu entwickelte Kopplung der beiden Methoden eröffnet dabei die Möglichkeit, nichtlineare Effekte wie

Wellenbrechung und Welle-Struktur-Interaktionen zeiteffizient und präzise zu berechnen.

Contents

Abstract	iii
Zusammenfassung	v
List of figures	xxi
List of tables	xxvii
1 Introduction	1
1.1 Reports and records of Rogue Waves	2
1.2 Design of offshore structures	4
1.3 Analysis of storm data recorded at <i>North Alwyn</i>	6
1.4 Objectives and Outline of the thesis	7
1.5 General remarks	8
2 Optimization of Rogue Wave Sequences	9
2.1 Linear optimization of Rogue Waves	11
2.2 Experimental optimization of Rogue Waves	14
2.3 Transfer of the wave signal	21
2.4 Phase-amplitude iteration scheme	25
2.5 Comparison of optimization approaches	27

3	Investigation of Offshore Structures	29
3.1	Investigated structures	30
3.1.1	FPSO	30
3.1.2	Crane vessel	31
3.1.3	Semisubmersible	32
3.2	Experimental setup	33
3.2.1	Setup for the FPSO and for the crane vessel	33
3.2.2	Setup for the semisubmersible	34
3.3	Numerical simulation of motions and loads	38
3.3.1	WAMIT	38
3.3.2	SEAWAY	41
3.3.3	IST TIME-DOMAIN CODE	42
4	Bending Moments and Motions of Ships	43
4.1	Results for the FPSO	43
4.1.1	Transfer functions of bending moments and motions of the FPSO	44
4.1.2	Frequency-domain approach and statistical analysis of loads and motions of the FPSO	46
4.1.3	Comparison to classification rules	49
4.1.4	Time-domain investigation of the FPSO encountering the <i>New Year Wave</i>	50
4.1.5	Variation of the location of encounter between the <i>New Year Wave</i> and the FPSO	53
4.1.6	Variation of period and height of the <i>New Year Wave</i> sequence	56
4.1.7	FPSO in Rogue Waves integrated in storm seas	59
4.2	Results for the crane vessel	68
4.2.1	Transfer functions of bending moments and motions of the crane vessel	68

4.2.2	Frequency-domain approach and statistical analysis of loads and motions of the crane vessel	69
4.2.3	Comparison to classification rules	71
4.2.4	Time-domain investigation of the crane vessel encountering the <i>New Year Wave</i>	73
4.2.5	Variation of the location of encounter between the crane vessel and the <i>New Year Wave</i>	75
4.2.6	Crane vessel in Rogue Waves integrated in storm seas .	76
4.3	Discussion of the FPSO and the crane vessel results	85
5	Splitting Forces, Airgap and Motions	87
5.1	Morison equation	88
5.2	Transfer functions determined by WAMIT	91
5.3	Statistical analysis of <i>GVA 4000</i>	94
5.4	Investigation of the <i>New Year Wave</i> impact	99
5.5	<i>GVA 4000</i> encountering Rogue Waves	101
5.6	Discussion of semisubmersible results	110
6	Numerical Simulation of Wave Propagation	111
6.1	WAVETUB	112
6.2	Numerical wave tanks based on RANSE solvers	115
6.2.1	FLUENT	115
6.2.2	COMET	120
6.3	Coupling of Pot/ FE and RANSE solver	122
6.4	Comparison of numerical wave tanks	124
7	Conclusions and Perspectives	127
	Bibliography	131
	Nomenclature	137

Optical System for the Registration of Motions	143
Registration of Forces and Moments	147
Design of a Wave Maker for the Small Wave Tank	151

List of Figures

1.1	Record of a Rogue Wave, the so-called <i>New Year Wave</i> , measured in the North Sea at the <i>Draupner</i> jacket platform on January 1st, 1995 (Haver and Anderson (2000)), $H_s = 11.92$ m, $H_{max} = 25.63$ m = $2.15 \cdot H_s$, $\zeta_c = 18.5$ m = $0.72 \cdot H_{max}$, water depth $d = 70$ m.	3
1.2	Registration of another Rogue Wave recorded in the Japanese Sea off Yura harbor by the Japanese National Maritime Institute (Mori et al. (2000)), $H_s = 5.09$ m, $H_{max} = 13.6$ m = $2.67 \cdot H_s$; $\zeta_c = 8.2$ m = $0.6 \cdot H_{max}$, $d = 43$ m.	3
1.3	Record of Rogue Wave measured at <i>North Alwyn</i> on November 19th, 1997, $H_s = 8.64$ m, $H_{max} = 22.03$ m = $2.55 \cdot H_s$, $T_p = 13.11$ s, $d = 126$ m. From statistics, such an extreme wave with $H_{max} = 2.55 \cdot H_s$ would be expected in a storm lasting 51 days.	6
1.4	Analysis of a storm recorded at <i>North Alwyn</i> on November 16th till 21st, 1997, maximum $H_s = 10.67$ m, maximum $H_{max} = 22.03$ m, maximum $H_{max}/H_s = 2.55$ (20-minute records). Within five days, 21 waves with $H_{max}/H_s > 2$ are observed, confirming that Rogue Waves are rather normal events.	7
2.1	Target parameters of a Rogue Wave group integrated in irregular seas.	12
2.2	Result of the <i>linear optimization</i> for the generation of an initial control signal ($H_s = 13$ m, $T_p = 13$ s).	13
2.3	Comparison of the recorded <i>Yura wave</i> presented in chapter 1 to the wave tank realization. The control signal for the experiment is generated by the <i>linear optimization</i> approach.	15

- 2.4 Evolution of the *Yura wave* in the wave tank at selected positions. The wave train is synthesized based on target parameters using the *linear optimization* approach at scale 1:112. Full-scale wave data have been collected by National Maritime Research Institute, Japan, Mori et al. (2000). The Rogue Wave develops from a rather unsuspecting looking wave group. 16
- 2.5 Initial control signal ($x_c(t)$) of the optimization process and associated 3-scale discrete wavelet transform. For the *experimental optimization* of the embedded Rogue Waves 90 wavelet coefficients are considered (coefficients 85–129 and 404–448). 17
- 2.6 Computer controlled optimization of waves: The wave sequence is automatically created, measured, evaluated and modified until convergence is achieved, i. e. the target wave train is generated. 18
- 2.7 Improved wave train and corresponding zero-downcrossing wave characteristics: Final step 1690 of the *experimental optimization* in the small wave tank at scale 1:303. The optimized wave train (blue) satisfies all predefined target characteristics: $H_s = 13$ m, $T_p = 13$ s, $H_{target} = 2 \cdot H_s$, $T_{target} = T_p$, $\zeta_{c target} = 0.6 \cdot H_{target}$ and $t_{target} = 55$ s. 19
- 2.8 Synthesis of the wave sequence showing 50 iteration steps. Blue: Starting signal for the *experimental optimization* – Red: Final wave sequence satisfying the predefined parameters: $H_s = 13$ m, $T_p = 13$ s, $H_{target} = 2 \cdot H_s$, $T_{target} = T_p$, $\zeta_{c target} = 0.6 \cdot H_{target}$ and $t_{target} = 55$ s. 20
- 2.9 Comparison of the control signals of the small and the large wave tank. Although the signals look different an identical wave sequence is generated in both tanks. 22
- 2.10 Comparison of realized wave in the small wave basin (flap type wave generator, $d = 0.4$ m) to the same (scaled) wave in the large wave basin (piston type wave generator, $d = 1.5$ m) after transformation of the control signals. Good agreement between both wave sequences is observed. 23
- 2.11 Optimized and scaled wave train, measured in the large wave tank (scale 1:81). The embedded Rogue Wave satisfies the predefined target parameters (red circles). 24

2.12	Optimized wave train at target position ($x = 30$ m, water depth $d = 1.5$ m) after two iteration steps of the phase-amplitude iteration scheme in comparison to recorded <i>New Year Wave</i> sequence (wave tank simulation at scale 1:81, presented as full scale data).	26
2.13	Optimized wave train at target position ($x = 6$ m, water depth $d = 0.4$ m) after 23 iteration steps in comparison to recorded <i>New Year Wave</i> sequence (wave tank simulation at scale 1:175, presented as full scale data).	26
2.14	Optimized wave train at target position ($x = 6$ m, water depth $d = 0.4$ m) after ten iteration steps in comparison to recorded <i>New Year Wave</i> sequence (wave tank simulation at scale 1:250, presented as full scale data).	27
3.1	Segmented model of the FPSO during tests in the wave tank, scale 1:81. Bending moments are registered at midship and at quarter length from bow.	34
3.2	Model of the crane vessel with the halves of the hull connected by strain gauges for the registration of the bending moments.	35
3.3	Side view of the FPSO at midship: The vertical position of the connecting steel elements, which are equipped with strain gauges for the registration of the bending moments, can be changed (photo: measuring device for bending moments at water line level).	36
3.4	The main hulls of the semisubmersible <i>GVA 4000</i> are connected by a cross bracing equipped with strain gauges to register the splitting forces in waves. The ballast weights can be changed for different displacements and positioned at different heights.	37
3.5	Discretization of the FPSO for the numerical analysis of motions and bending moments.	39
3.6	Crane vessel discretization for the analysis using WAMIT.	39
3.7	Discretization of semisubmersible <i>GVA 4000</i> at drilling draft for the analysis of seakeeping behavior and splitting forces using WAMIT.	41

- 4.1 Transfer function of the vertical bending moments of the FPSO at midship position, measured and calculated at water line level. Maximum responses are observed if the wave length equals L_{pp} corresponding to hogging and sagging cases. 45
- 4.2 Transfer function of the vertical bending moment of the FPSO at midship position, measured and calculated at deck level. The amplitude of maximum response is clearly lower than in the case with connecting elements at water line level. 46
- 4.3 Frequency-domain analysis of the bending moments at midship section of the FPSO ship: Sea spectra – response amplitude operator – response spectra – significant bending moment double amplitude. Maximum bending moments are expected in sea states with $T_0 = 11$ s. 47
- 4.4 Frequency-domain analysis of the heave motion of the FPSO: Sea spectra – response amplitude operator – response spectra – significant heave motion double amplitude. Due to the large dimensions of the FPSO the heave motions are kept low for sea states with short periods. 48
- 4.5 Frequency-domain analysis of the pitch motion of the FPSO: Sea spectra – response amplitude operator – response spectra – significant pitch double amplitude. The pitch transfer function shows a similar characteristic as the transfer functions of the bending moments. Thus the sagging and hogging case – wave length equals L_{pp} – gives also the largest pitch motions. 49
- 4.6 Comparison of experimental and numerical simulation of the FPSO facing the *New Year Wave*: Wave elevation – vertical bending moment at midship (at waterline level) – heave motion – pitch motion. The Rogue Wave impact results in responses larger than predicted by statistical means and classification rules. 51
- 4.7 *New Year Wave* measured at different positions in the wave tank (left) and associated vertical bending moments of the FPSO due to the Rogue Wave impact (right). Maximum bending moments are observed $-1/4L_{pp}$ upstream for sagging and $+1/4L_{pp}$ downstream for hogging, revealing that the *New Year Wave* is more severe at these positions than at the original one. 54

4.8 *New Year Wave* (black), *New Year Wave* with elongated period (blue), and *New Year Wave* with elongated period and increased wave height (red) as well as resultant heave and pitch motion and vertical bending moments at midship and at quarter length from bow. The wave history is kept unchanged, thus enabling the relation of changes in response to the modifications introduced into the *New Year Wave*. 58

4.9 FPSO in storm sea with embedded Rogue Wave generated by the *experimental optimization* process presented in chapter 2, $H_{max}/H_s = 2$, $H_s = 13$ m, $T_p = 13$ s, $\gamma = 1$. Although the ratio of $H_{max}/H_s = 2$ is frequently observed during a storm, responses are significantly larger than estimated by statistics. 60

4.10 Responses of the FPSO due to storm scenario A: $T_p = 15$ s, $H_s = 13$ m, $H_{max} = 31.85$ m and $H_{max}/H_s = 2.45$. Although this wave sequence has the second smallest ratio of H_{max}/H_s of the four wave sequences synthesized by the *linear optimization* process, the bending moments as well as the pitch motions are the largest observed in the model tests. 62

4.11 Responses of the FPSO due to storm scenario B: $T_p = 15$ s, $H_s = 13$ m, $H_{max} = 32.56$ m and $H_{max}/H_s = 2.50$. Both numerical methods have difficulties to model the consequences of the Rogue Wave impact, i. e. to model the maximum responses precisely. 63

4.12 Responses of the FPSO due to storm scenario C: $T_p = 14$ s, $H_s = 12$ m, $H_{max} = 28.83$ m and $H_{max}/H_s = 2.40$. Surprisingly, the wave sequence with the smallest ratio of H_{max}/H_s gives heave motions 48% larger than estimated by frequency-domain analysis. 64

4.13 Responses of the FPSO due to storm scenario D: $T_p = 14$ s, $H_s = 12$ m, $H_{max} = 32.15$ m and $H_{max}/H_s = 2.68$. Unexpectedly, the worst wave scenario with a ratio of $H_{max}/H_s = 2.68$ gives not the worst responses. 65

4.14 Transfer function of the bending moment of the crane vessel, comparing experimental and numerical results. The maximum responses are lower than for the FPSO due to the smaller dimensions of the crane vessel. 69

- 4.15 Frequency-domain analysis of the bending moments at midship section of the crane vessel: Sea spectra – response amplitude operator – response spectra – significant bending moment double amplitude. Maximum significant amplitudes are observed in the range of $T_0 = 10$ s. 70
- 4.16 Frequency-domain analysis of the heave motion of the crane vessel: Sea spectra – response amplitude operator – response spectra – significant heave motion double amplitude. The significant heave motion converges towards 1 for large periods. Thus, the ship follows the wave motion in long waves. 71
- 4.17 Frequency-domain analysis of the pitch motion of the crane vessel: Sea spectra – response amplitude operator – response spectra – significant pitch double amplitude. The pitch transfer function looks similar to the transfer function of the bending moments, resulting in an similar transfer function of the significant pitch motion. 72
- 4.18 Crane vessel encountering the *New Year Wave*: Comparison of experimental and numerical results: *New Year Wave* – vertical bending moment at midship – heave motion – pitch motion. The *New Year Wave* causes bending moments just within limitation of classification rules. 73
- 4.19 Impression of the crane vessel model facing the *New Year Wave* in the wave tank. Beside extreme bending moments, encountering the *New Year Wave* causes also high impact loads on the bow and green water on deck. 76
- 4.20 Storm sea with embedded Rogue Wave generated by the *experimental optimization* approach and associated responses of the crane vessel, $H_{max}/H_s = 2$, $H_s = 13$ m, $T_p = 13$ s, $\gamma = 1$. The observed responses are significantly larger than estimated by statistics. Thus, the *experimental optimization* approach proves its potential for the synthesization and investigation of extreme wave scenarios. 77
- 4.21 Responses of the crane vessel due to storm scenario A, generated by the *linear optimization* approach: $T_p = 15$ s, $H_s = 13$ m, $H_{max} = 31.85$ m and $H_{max}/H_s = 2.45$. The bending moments as well as the heave and pitch motions are well predicted by the seakeeping codes, although this codes are based on linear wave theory. 79

- 4.22 Responses of the crane vessel due to storm scenario B: $T_p = 15$ s, $H_s = 13$ m, $H_{max} = 32.56$ m and $H_{max}/H_s = 2.50$. The time-domain analysis reveals the significant impact of the Rogue Wave, as statistical methods underestimate the consequences of these extreme events. 80
- 4.23 Responses of the crane vessel due to storm scenario C: $T_p = 14$ s, $H_s = 12$ m, $H_{max} = 28.83$ m and $H_{max}/H_s = 2.40$. Storm scenario C appears to be the worst for the crane vessel since the exceedance of the statistical values is largest. This is surprising, as this storm scenario has the lowest ratio of $H_{max}/H_s = 2.40$ of the four Rogue Wave sequences synthesized by the *linear optimization* approach. 81
- 4.24 Responses of the crane vessel due to storm scenario D: $T_p = 14$ s, $H_s = 12$ m, $H_{max} = 32.15$ m and $H_{max}/H_s = 2.68$. The largest wave causes not inevitably the highest responses, rather the local wave characteristics as well as the wave pattern determine the reactions. 82
- 5.1 Horizontal forces on the semisubmersible *GVA 4000*. The splitting forces (green line) are at a maximum, where the sum of the external forces (red line, denoted as total forces) vanishes, i. e. structural forces are maximal when the horizontal motions are minimal and vice versa. 90
- 5.2 Transfer function of the splitting forces of the semisubmersible *GVA 4000* at drilling draft as a result of model tests and calculations in beam seas. For comparison, the blue line gives the transfer function of the splitting forces at survival draft. At survival draft structural responses are larger than for the drilling draft, since the hulls are closer to the water surface with the consequence of higher wave forces. 92
- 5.3 Transfer functions of the heave motion of the semisubmersible *GVA 4000* at drilling draft and survival draft for wave angles 90° and 180° . For comparison the experimentally obtained heave transfer function is also given and agrees well with calculations by WAMIT. 93

- 5.4 Transfer function of the variation in airgap of the semisubmersible *GVA 4000* comparing results from numerical simulations and model tests. The resultant airgap in time-domain is the sum of still water airgap and variation of airgap. The transfer function is derived from the heave transfer function presented in Fig. 5.3. 94
- 5.5 Frequency-domain analysis of the splitting forces of the semi-submersible *GVA 4000*: Sea spectra – response amplitude operators – response spectra – significant double amplitudes of splitting forces for drilling and survival draft. The differences observed between drilling and survival draft in the significant transfer functions are only small. Largest responses are expected for sea states with short periods. 95
- 5.6 Frequency-domain analysis of the heave motion of the semi-submersible *GVA 4000*: Sea spectra – response amplitude operators – response spectra – significant heave double amplitudes. The significant heave transfer function of the *GVA 4000* is very similar to the significant heave transfer function of the FPSO and crane vessel. 96
- 5.7 Frequency-domain analysis of the airgap of the semisubmersible *GVA 4000*: Sea spectra – transfer function for operation and survival draft – response spectra – significant airgap double amplitudes. The significant responses are relatively insensitive to the zero-upcrossing period of the sea state. 97
- 5.8 Frequency-domain analysis of airgap of semisubmersible *GVA 4000* applying the JONSWAP spectrum with $\gamma = 3.3$: Sea spectra – response amplitude operators – response spectra – significant airgap double amplitudes. The statistical analysis based on the JONSWAP spectrum gives smaller significant amplitudes for the airgap in the range of 9 s – 14 s, but larger responses below and above this frequency range. 98
- 5.9 Comparison of model test data and calculated splitting forces, heave motions and airgap of the semisubmersible *GVA 4000* in the *New Year Wave*. Fortunately, the airgap remains positive when the Rogue Wave passes beneath the main deck. 100

- 5.10 Semisubmersible *GVA 4000* in storm sea with embedded Rogue Wave generated by the *experimental optimization* approach as proposed in chapter 2, $H_{max}/H_s = 2$, $H_s = 13$ m, $T_p = 13$ s, $\gamma = 1$. The splitting forces of the semisubmersible are of impressive dimensions of $4.57 \cdot 10^4$ kNm, which equals the gravitational force corresponding to a mass of 4570 t. Without cross bracings taking up these enormous forces, the resultant moments would be cracking the column deck joint. 102
- 5.11 Responses of the semisubmersible *GVA 4000* due to storm scenario A generated by the *linear optimization* approach: $T_p = 15$ s, $H_s = 13$ m, $H_{max} = 31.85$ m and $H_{max}/H_s = 2.45$. Although this wave sequence causes very large bending moments of the FPSO and the crane vessel, the splitting forces of the semisubmersible are small and well covered by statistics. 104
- 5.12 Responses of the semisubmersible *GVA 4000* due to storm scenario B: $T_p = 15$ s, $H_s = 13$ m, $H_{max} = 32.56$ m and $H_{max}/H_s = 2.50$. This wave scenario gives the maximum decrease in airgap of -15.61 m. Nevertheless, the airgap remains still sufficient with 9.19 m. 105
- 5.13 Responses of the semisubmersible *GVA 4000* due to storm scenario C: $T_p = 14$ s, $H_s = 12$ m, $H_{max} = 28.83$ m and $H_{max}/H_s = 2.40$. The wave sequence with the smallest ratio of H_{max}/H_s gives the largest heave motion. This phenomena is also observed for the FPSO and the crane vessel. 106
- 5.14 Responses of the semisubmersible *GVA 4000* due to storm scenario D: $T_p = 14$ s, $H_s = 12$ m, $H_{max} = 32.15$ m and $H_{max}/H_s = 2.68$. The largest splitting forces are caused by the extremely high Rogue Wave. 107
- 6.1 WAVETUB – Comparison of numerical (Pot/ FE) and experimental wave sequence generated by the same wave maker signal ($T_p = 14.6$ s, $H_s = 15.3$ m): registrations at different positions at the Hamburg Ship Model Basin (double flap wave generator). 113
- 6.2 WAVETUB – *New Year Wave* – Comparison of wave tank simulation at TUB, piston type wave generator, and numerical wave tank calculation by means of Pot/ FE at scale 1:81. . . . 114

6.3	Definition of the boundary conditions for the numerical wave tanks based on FLUENT and COMET.	116
6.4	FLUENT – Numerical simulation of irregular sea based on a JONSWAP spectrum applying the RANSE/ VOF method, $T_P = 2.2$ s and $H_s = 0.1$ m, with integrated wave packet, $H_{max} = 0.35$ m, $H_{max}/H_s = 2.3$, as Three Sisters wave, at different positions in the wave tank in comparison to wave tank realization (scale 1:81).	117
6.5	FLUENT – Numerical simulation of irregular sea based on JONSWAP spectrum, $T_P = 2.2$ s, $H_s = 0.1$ m, with integrated wave packet, $H_{max} = 0.35$ m, as Rogue Wave, at different positions in the wave tank (scale 1:81). Numerical simulation based on RANSE/ VOF.	118
6.6	FLUENT – Numerical simulation based on RANSE/ VOF of a wave packet, with same JONSWAP spectrum as in Fig. 6.5, in comparison to wave tank realization (scale 1:81).	119
6.7	Computational block structured grid for all simulations using COMET with 26.260 control volumes. Smaller cells are generated near the free surface in order to improve the accuracy of the simulations.	120
6.8	COMET – Numerical simulation of the wave packet based on JONSWAP spectrum, $T_P = 2.2$ s and $H_s = 0.1$ m, with time step size $dt = 0.005$ s, in comparison to experimental data. . .	121
6.9	COMET – Numerical simulation of irregular sea based on JONSWAP spectrum, $T_P = 2.2$ s, $H_s = 0.1$ m, with integrated wave packet, $H_{max} = 0.35$ m, at different positions in the wave tank. The simulation applies the RANSE/ VOF method with time step size of $dt = 0.002$ s.	122
6.10	Coupling of WAVETUB and COMET at position 25 m from wave board. Showing a wave packet advancing from the Pot/ FE solver domain (left hand side) to the RANSE/ VOF solver COMET domain (right hand side) at five instants.	123
1	Active markers mounted on the model of the semisubmersible <i>GVA 4000</i> . The red LEDs are easy detectable by the motion tracking algorithm since they are surrounded by a black area giving a high contrast.	144

- 2 Deflection of force and moment transducer and arrangement of resistive type strain gauges in a wheatstone bridge configuration for force measurement. 148
- 3 Deflection of force and moment transducer and arrangement of resistive type strain gauges in a wheatstone bridge configuration for the measurement of bending moments. Along the different arrangement of the strain gauges in the wheatstone bridge makes the difference between moment and force transducer. 149
- 4 Most common types of wave generators: Piston type, flap type, duplex type, double flap type and plunger type (from left to right, top to bottom). 152
- 5 Maximum wave height restricted by the wave breaking limit depending on wave frequency for a water depth of 0.4 m (blue line). The maximum feasible wave height is smaller than the water depth. The red line gives the maximum reasonable wave height for the small wave tank at TUB. 153
- 6 Biésel transfer function for the piston type (magenta line) as well as the flap type (blue line) wave generator for the small wave tank at TUB for a water depth of 0.4 m. With identical stroke, the piston type wave board generates larger waves due to the constant velocity profile over depth bringing more energy into the water. 154
- 7 Stroke amplitude of the piston type wave maker. For the generation of long waves the stroke goes to infinity and is therefore restricted to 0.1 m. 155
- 8 Maximum wave height that can be generated in the small wave tank by the piston type wave generator with a maximum stroke amplitude of 0.1 m. 156
- 9 Added mass for the small wave tank at TUB. For small waves the added mass becomes dramatically large, resulting in an enormous power requirement for wave generation. 158
- 10 Design power diagram for the wet back piston type wave generator at the small wave tank of TUB with a water depth of 0.4 m and a tank width of 0.3 m. In consequence, the minimum required engine power of the electrical motor is 560 W indicated by the orange circle. 159

List of Tables

4.1	Bending moments, heave and pitch motion of the FPSO due to the <i>New Year Wave</i> comparing statistical values and results from model tests: Measured maximum and minimum responses $s_{exp,max}$ and $s_{exp,min}$, significant amplitudes s_{sig} , maximum significant amplitudes $s_{sig,max}$, and ratio of maximum measured response to maximum significant response $ s_{exp} _{max}/s_{sig,max}$	52
4.2	Bending moments of the FPSO ship due to the modified <i>New Year Wave</i> sequences. The increase or even decrease of the bending moments due to a larger wave height, emphasis clearly the need for knowing the local wave characteristics and for time-domain investigations of Rogue Wave impacts.	57
4.3	Heave and pitch motions of the FPSO due to the modified <i>New Year Wave</i> sequences. Encountering wave sequence (3), responses of the FPSO are amplified more than proportional – indicated with bold font. As an extreme case, the heave motion is increased by 71%, although the exciting wave is only 29% larger, showing the nonlinear system behavior.	57
4.4	Bending moments, heave and pitch motions of the FPSO due to the wave sequence generated by the <i>experimental optimization</i> process, comparing statistical and experimental data: Measured maximum and minimum responses $s_{exp,max}$ and $s_{exp,min}$, significant pitch amplitudes s_{sig} , maximum significant amplitudes $s_{sig,max}$, and ratio of maximum measured response to maximum significant response $ s_{exp} _{max}/s_{sig,max}$	59

- 4.5 Characteristics of the four storm sea states with integrated Rogue Waves generated by the *linear optimization* approach: Peak period T_p , significant wave height H_s , maximum wave height H_{max} and the ratio of maximum to significant wave height H_{max}/H_s 61
- 4.6 Vertical bending moments of the FPSO due to storm seas: Sea state parameters, maximum measured hogging moment $M_{hogg,max}$, maximum measured sagging moment $M_{sagg,max}$, significant bending moment amplitude M_{sig} , maximum significant bending moment $M_{sig,max} = 1.86 \cdot M_{sig}$ and ratio of maximum measured moment to maximum significant bending moment $|M_{exp}|_{max}/M_{sig,max}$ 66
- 4.7 Heave motions of the FPSO due to storm seas: Sea state parameters, maximum and minimum measured heave motion $s_{3,exp,max}$ (up) and $s_{3,exp,min}$ (down), significant heave motion $s_{3,sig}$, maximum significant heave motion $s_{3,sig,max} = 1.86 \cdot s_{3,sig}$ and ratio of maximum measured heave motion to maximum heave motion amplitude $|s_{3,exp}|_{max}/s_{3,sig,max}$ 66
- 4.8 Pitch motions of the FPSO due to storm seas: Sea state parameters, maximum and minimum measured pitch motion $s_{5,exp,max}$ and $s_{5,exp,min}$, significant pitch motion $s_{5,sig}$, maximum significant pitch motion $s_{5,sig,max} = 1.86 \cdot s_{5,sig}$ and ratio of maximum measured pitch to maximum significant pitch $|s_{5,exp}|_{max}/s_{5,sig,max}$ 67
- 4.9 Bending moments, heave and pitch motion of the crane vessel due to the *New Year Wave*, comparing values from statistics and model tests: Measured maximum and minimum responses $s_{exp,max}$ and $s_{exp,min}$, significant amplitudes s_{sig} , maximum significant amplitudes $s_{sig,max}$, and ratio of maximum measured response to maximum significant response $|s_{exp}|_{max}/s_{sig,max}$ 74
- 4.10 Maximum wave heights and corresponding bending moments of the crane vessel for nine different positions of the *New Year Wave* in the wave tank. The *New Year Wave* turns out to be more severe at positions further up- and downstream resulting in larger bending moments. 75

4.11 Bending moments, heave and pitch motions of the crane vessel comparing statistical and measured values: Measured maximum and minimum responses $s_{exp,max}$ and $s_{exp,min}$, significant amplitudes s_{sig} , maximum significant amplitudes $s_{sig,max}$, and ratio of maximum measured response to maximum significant response $|s_{exp}|_{max}/s_{sig,max}$. The observed heave motion is nearly twice as large than predicted by frequency-domain analysis. 78

4.12 Vertical bending moments of the crane vessel due to storm seas: Sea state parameters, maximum measured hogging moment $M_{hogg,max}$ and sagging moment $M_{sagg,max}$, significant bending moment amplitude M_{sig} , maximum significant bending moment $M_{sig,max} = 1.86 \cdot M_{sig}$ and ratio of maximum measured moment to maximum significant bending moment $|M_{exp}|_{max}/M_{sig,max}$ 83

4.13 Heave motions of the crane vessel due to storm seas: Sea state parameters, maximum measured heave motion $s_{3,exp,max}$ (up) and $s_{3,exp,min}$ (down), significant heave motion amplitude $s_{3,sig}$, maximum significant heave motion $s_{3,sig,max} = 1.86 \cdot s_{3,sig}$ and ratio of maximum measured heave to maximum significant heave motion $|s_{3,exp}|_{max}/s_{3,sig,max}$ 83

4.14 Pitch motions of the crane vessel due to storm seas: Sea state parameters, maximum measured pitch motion $s_{5,exp,max}$ and $s_{5,exp,min}$, significant pitch amplitude $s_{5,sig}$, maximum significant pitch $s_{5,sig,max} = 1.86 \cdot s_{5,sig}$ and ratio of maximum measured pitch to maximum significant pitch motion $|s_{5,exp}|_{max}/s_{5,sig,max}$ 84

5.1 Splitting forces, heave motions and airgap of the *GVA 4000* due to the *New Year Wave* comparing results from statistics and model tests: Measured maximum and minimum responses $s_{exp,max}$, $s_{exp,min}$, significant amplitudes s_{sig} , maximum significant amplitudes $s_{sig,max}$, and ratio of maximum measured response to maximum significant response $|s_{exp}|_{max}/s_{sig,max}$. The decrease in airgap and the resultant splitting forces are clearly underestimated by statistics. 100

- 5.2 Splitting forces, heave motions and airgap of the *GVA 4000* in the Rogue Wave sequence from the *experimental optimization* approach, $H_s = 13$ m, $T_p = 13$ s, for survival conditions, 16.2 m draft, comparing statistical and experimental values: Measured maximum and minimum responses $s_{exp,max}$, $s_{exp,min}$, significant amplitudes s_{sig} , maximum significant amplitudes $s_{sig,max}$, and ratio of maximum measured response to maximum significant response $|s_{exp}|_{max}/s_{sig,max}$. With respect to the splitting forces, this Rogue Wave sequence appears to be rather moderate. Note, that this Rogue Wave sequence causes bending moments of the FPSO 83% larger than estimated by statistics. 103
- 5.3 Splitting forces of the *GVA 4000* due to storm seas: Sea state parameters, maximum splitting forces from model tests (compression and tension), significant splitting force amplitude F_{sig} , maximum splitting force amplitude $F_{sig,max} = 1.86 \cdot F_{sig}$, and ratio of maximum measured splitting force to maximum significant splitting force amplitude $|F_{exp}|_{max}/F_{sig,max}$. In comparison to the findings of the analysis of the bending moments of the FPSO, the deviations found between statistical values and experimental data for the splitting forces are rather small, i. e. an underestimation of maximal 28%. 108
- 5.4 Heave motion of the *GVA 4000* due to storm seas: Sea state parameters, maximum measured heave motion (up $s_{3,exp,max}$ and down $s_{3,exp,min}$), significant heave amplitude $s_{3,sig}$, maximum heave amplitude $s_{3,sig,max} = 1.86 \cdot s_{3,sig}$, and ratio of maximum measured heave amplitude to maximum significant heave amplitude $|s_{3,exp}|_{max}/s_{3,sig,max}$. The semisubmersible shows a nonlinear system behavior, thus, heave responses cannot be directly related to the wave height or the ratio of H_{max}/H_s 108

5.5 Variation in airgap of the semisubmersible due to storm seas:
 Sea state parameters, maximum airgap from measurement (up $s_{7,exp,max}$ and down $s_{7,exp,min}$), significant airgap amplitude $s_{7,sig}$, maximum airgap amplitude $s_{7,sig,max} = 1.86 \cdot s_{7,sig}$ and ratio of maximum measured airgap amplitude to maximum significant airgap amplitude $|s_{7,exp}|_{max}/s_{7,sig,max}$. For all four Rogue Wave scenarios, the influence of the extreme wave on the airgap is underestimated. Nevertheless, the *GVA 4000* is not in danger, since the airgap remains large enough in all Rogue Wave sequences. 109

Chapter 1

Introduction

Since time immemorial, seafarers have been heard telling unbelievable stories of gigantic waves or white walls of water, washing men and cargo over board, smashing hulls, capsizing and drowning even the strongest built ships. But the accounts of survivors of such Rogue Wave impacts were often contributed to a vivid fantasy or to an oversized portion of rum.

Times have changed, ships have become bigger, stronger and safer, but still, vessels and offshore structures are lost and damaged in severe weather, many of which after encountering a Rogue Wave. More and more serious reports of Rogue Wave encounters have drawn the interests of scientists to this phenomena. Motivated by these accounts, over the last years research projects have focussed on such extreme waves, their formation and impact on marine structures in order to throw light on this mystery (e. g. the *MAXWAVE* project, funded by the European Union). Fortunately, the chances to encounter a Rogue Wave are rare – unfortunately, observations, photos or measurements are also.

However, even though their probability is very low, they are physically possible and prove to occur more often than predicted by statistical methods as is underlined by these reports. With the improvement of wave measuring techniques, a number of Rogue Waves have been observed all over the oceans. Nevertheless, many questions concerning Rogue Waves and their impacts on marine structures are still waiting for answers.

In this thesis, means to answers some of these questions are proposed and several of the frightening Rogue Waves are brought into the model basin in order to analyze their effects on offshore structures.

1.1 Reports and records of Rogue Waves

In recent years, terms like Freak Wave, Rogue Wave or Monsters of the Deep could often be read in newspapers or heard in radio and television. The public is more sensitized to extreme waves due to reports from passengers of cruise liners encountering a Rogue Wave and publications of ongoing Freak Wave research. The growing trend of adventure travel, like visiting the most southern or northern waters of our planet earth, leads cruise liners into rough sea areas. Thus, in February 2001, the cruise liner *Bremen* encountered a Rogue Wave that was estimated to be 35 m high. The wave smashed a window, flooded the bridge, short-circuited the electronics with the consequence of total power loss. The ship drifted for 30 minutes, disabled in beam seas, with rolling angles up to 40° (Schulz (2001)). In 2005, the cruise vessels *Voyager* (February 14th) and *Norwegian Dawn* (April 16th) were also hit by Rogue Waves with similar consequences. Also the cruise liner *Queen Elizabeth 2* encountered such a Rogue Wave in February 1995 during an Atlantic crossing. Beside these reports of cruise vessels, many other freighters, tankers, container ships and offshore platforms have encountered Rogue Waves – sometimes unharmed, sometimes damaged, sometimes lost.

Reports on individual extreme waves in deep water mention either single high waves or several successive high waves (e. g. Three Sisters) – but when is a wave really a Rogue? Faulkner (2000) presents examples of extreme waves and proposes the definition $H_{max} > 2.4 \cdot H_s$ for waves with abnormal height, where H_s denotes the significant wave height. Wolfram et al. (2000) suggest that only waves exceeding $H_{max} > 2.3 \cdot H_s$ should be termed Rogue Waves. From probability analysis of Rogue Wave data recorded from 1994 to 1998 at North Alwyn, Wolfram et al. (2000) conclude that these waves are generally 50% steeper than the significant steepness of the surrounding sea state. Furthermore, the preceding and succeeding waves have steepness values around half the significant values while their heights are around the significant height, i. e. a Rogue Wave group characteristically comprises a wave sequence with $H_s, 2 \cdot H_s, H_s$.

To illustrate the phenomena of a Rogue Wave, in Figs. 1.1 and 1.2 two typical wave records with ratios of $H_{max}/H_s > 2$ are presented:

- A giant wave ($H_{max} = 25.63$ m) with a crest height of $\zeta_c = 18.5$ m that hit the *Draupner* jacket platform on January 1st, 1995 and will be denoted in the following as *New Year Wave* (Haver and Anderson (2000)). During this time the significant wave height was $H_s = 11.92$ m resulting in a ratio of $H_{max}/H_s = 2.15$.

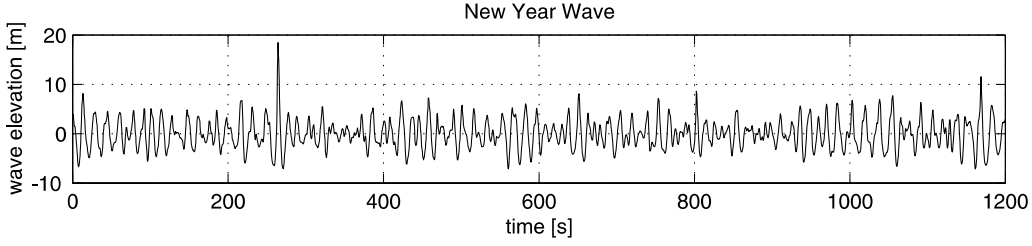


Figure 1.1: Record of a Rogue Wave, the so-called *New Year Wave*, measured in the North Sea at the *Draupner* jacket platform on January 1st, 1995 (Haver and Anderson (2000)), $H_s = 11.92$ m, $H_{max} = 25.63$ m = $2.15 \cdot H_s$, $\zeta_c = 18.5$ m = $0.72 \cdot H_{max}$, water depth $d = 70$ m.

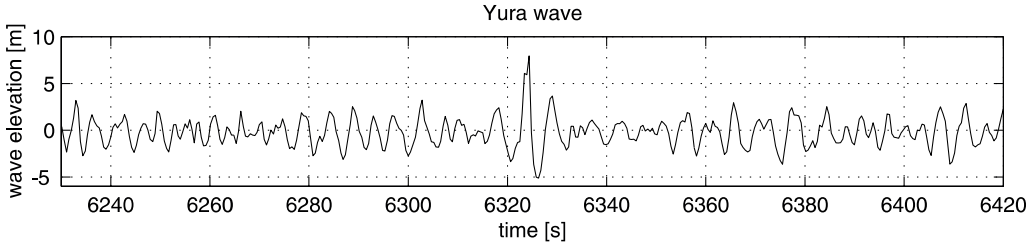


Figure 1.2: Registration of another Rogue Wave recorded in the Japanese Sea off Yura harbor by the Japanese National Maritime Institute (Mori et al. (2000)), $H_s = 5.09$ m, $H_{max} = 13.6$ m = $2.67 \cdot H_s$; $\zeta_c = 8.2$ m = $0.6 \cdot H_{max}$, $d = 43$ m.

- A wave recorded off Yura harbor in the Japanese Sea, with a maximum wave height of 13.6 m and a crest height of $\zeta_c = 8.2$ m. This wave has been recorded in a sea state of $H_s = 5.09$ m resulting in $H_{max}/H_s = 2.67$ (Mori et al. (2000)).

These two extraordinary wave trains will be realized in this thesis in the wave tank by new wave generation techniques presented. Furthermore, the so-called *New Year Wave* is applied for the investigation of wave-structure interactions (see chapter 4 and 5) to reveal the significant of Rogue Wave impacts.

Beside these two Rogue Wave examples, exceptional waves are also reported from the Norwegian Frigg field (Kjeldsen (1990)) with $H_s = 8.49$ m, $H_{max} = 19.98$ m, $\zeta_c = 12.24$ m, water depth $d = 99.4$ m, as well as from the Danish Gorm field (Sand et al. (1990)) with $H_s = 6.9$ m, $H_{max} = 17.8$ m, $\zeta_c \approx 13$ m, $d = 40$ m. Further abnormal waves are identified in the North Cormoran

field in the North Sea (Guedes Soares et al. (2004a)) and in hurricane Camille (Guedes Soares et al. (2004b)).

Using the definition $H_{max}/H_s > 2.0$ for Rogue Waves, Wolfram et al. (2000) analyzed 394537 waves from storms with $H_s > 6.5$ m, recorded from 1994 to 1998 at *North Alwyn* and found 114 Rogue Waves. Thus, 0.029% of all waves recorded were Rogue Waves, i. e. every 3460th wave. From statistical analysis such as highlighted in section 1.2 (see equation 1.1) follows that every 2980th wave can be expected to have a ratio of $H_{max}/H_s > 2.0$, which is in good agreement with this observations.

All these wave data – with $H_{max}/H_s > 2.0$ and $\zeta_c/H_{max} > 0.6$ – prove, that Rogue Waves are serious events which should be considered in the design process and by no means only cock-and-bull stories of seaman. Although their probability of occurrence is very low, they are physically possible. In the future, climate changes due to the greenhouse effect may also lead to extreme storm conditions occurring more frequently. In the pass of Hurricane Ivan in 2004, in the Gulf of Mexico, H_s values of up to 17.9 m have been recorded (Wang et al. (2005)). The category 4 Hurricane passed the wave gauges in a distance of 73 km. For the Hurricane eye’s center, Wang et al. (2005) estimate a maximum H_s of 21 m resulting in a maximum wave height of more than 40 m. As observations of waves in such extreme conditions are seldom, it still remains a challenging question which maximum wave and crest heights can develop in a certain sea state characterized by H_s and T_p .

1.2 Design of offshore structures

For the design of offshore structures, it is important to determine extreme loads and motions. As direct numerical simulations of actions of extreme waves on structures are becoming more popular for the design, determination of low probability values of meteorological and oceanographic data is crucial. The 1000 year or even 10000 year extreme wave, i. e. a wave with a 10^{-3} or 10^{-4} annual probability of exceedance, is considered routinely in design or even required by standards. As an example, the ISO 19900 standard (ISO (2003)) for the offshore and petroleum industry defines that an extreme value has a 10^{-2} annual probability of exceedance and an abnormal value of 10^{-3} to 10^{-4} . If the action of wind and current is neglected, offshore structures have to withstand undamaged, wave conditions of a 100 years return period, which is also called *ultimate limit state*. The NORSOK standard (NORSOK (2004)) of the Norwegian petroleum industry requires that a structure hit by

the 10000 years wave, should not suffer complete loss of integrity (*accidental limit state*).

The determination of the maximum values, describing the worst sea condition to be expected, is extremely difficult as often wave data are nonexistent for the selected location. Also for sea areas where measurements of the wave climate are available for long periods (such a 30 years), the estimation of the 10000 year extreme value is strongly dependent on the extrapolation method and wave model used.

As noted before, it is a common procedure to determine the maximum wave height from a given maximum significant wave height at the location of interest. In most cases, the sea states are considered as a narrow banded process and wave heights are assumed to be Rayleigh distributed. Statistical analysis of many storm seas validates this premise (Jonathan et al. (1994)). Based on this assumptions, the maximum wave height within a given time interval of a sea state, characterized by H_s , can be assessed:

$$H_{max} = H_s \sqrt{\frac{\ln N}{2}}, \quad (1.1)$$

with N the number of waves. To estimate the maximum wave height of a storm with 3 hour persistence and a mean period of 10 s this results in $H_{max} = 1.86 \cdot H_s$. This value of 1.86 is often used to determine the maximum wave heights required for the design process. Encouraged by the Rogue Wave observations presented previously, with H_{max}/H_s ratios larger two, in this thesis the question will be tackled, if this assumption is still valid.

Boosting the doubts that at ratio of 1.86 of maximum to significant wave height may not be sufficient, Faulkner (2003) states, that this value of 1.86 is merely the most probable maximum and by no means the absolute maximum. Consequently, in 2004 the NORSOK standard defines a ratio of $H_{max}/H_s = 1.9$ for the maximum wave height within a 100 year storm of 2 hours duration. For an annual exceedance probability of 10^{-4} (*accidental limit state*), the NORSOK standard suggests the maximum wave height to be $H_{max10000} = 1.25 \cdot H_{max100}$, resulting in a ratio of $H_{max}/H_s = 2.375$. In addition, consideration of waves with extreme steepness is recommended, in particular for floating installations with columns and pontoons.

Since various definitions for Rogue Wave are proposed, in this thesis, waves exceeding the ratio of $H_{max}/H_s > 2$ are called Rogue Waves. The terms Rogue Wave, Freak Wave and Monster Wave are used as synonyms.

1.3 Analysis of storm data recorded at *North Alwyn*

To highlight the relevance of Rogue Waves, a 5 days storm (November 16th till 21st, 1997) recorded at the *North Alwyn* platform is analyzed. *North Alwyn* is located 160 km east of the Shetland Islands in the central North Sea. In Fig. 1.3, a 40-minutes wave record with an exceptional high wave with $H_{max}/H_s = 2.55$ is presented. This wave was measured on November 19th, 1997. During this time the significant wave height of the sea was 8.64 m and the maximum wave height 22.03 m. Applying equation 1.1, this H_{max}/H_s ratio of 2.55 would be expected in a storm containing 444630 waves, corresponding to a persistence of 51 days.

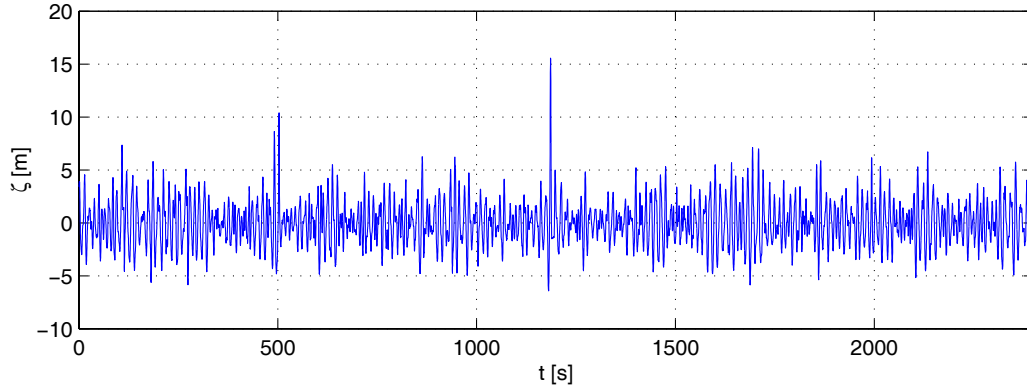


Figure 1.3: Record of Rogue Wave measured at *North Alwyn* on November 19th, 1997, $H_s = 8.64$ m, $H_{max} = 22.03$ m = $2.55 \cdot H_s$, $T_p = 13.11$ s, $d = 126$ m. From statistics, such an extreme wave with $H_{max} = 2.55 \cdot H_s$ would be expected in a storm lasting 51 days.

In addition to this astonishing findings, Fig. 1.4 confirms that waves with ratios of $H_{max}/H_s > 2$ are not really rare events. During the 5 days storm, 21 waves exceeding this limit have been registered (2 on 16th, 1 on 17th, 2 on 18th, 8 on 19th and 9 on 20th), i. e. on the 19th and 20th approximately every three hours a Rogue Wave was recorded!

Concluding, Rogue Waves with a ratio of $H_{max}/H_s > 2$ are by now means seldom, but rather normal. They occur more often than accounted for in many designs. Also the maximum ratio of H_{max}/H_s seems to be under estimated by predictions. All these facts highlight the importance of further detailed investigation of Rogue Wave impacts. The relevance of these findings will be exploited in this thesis.

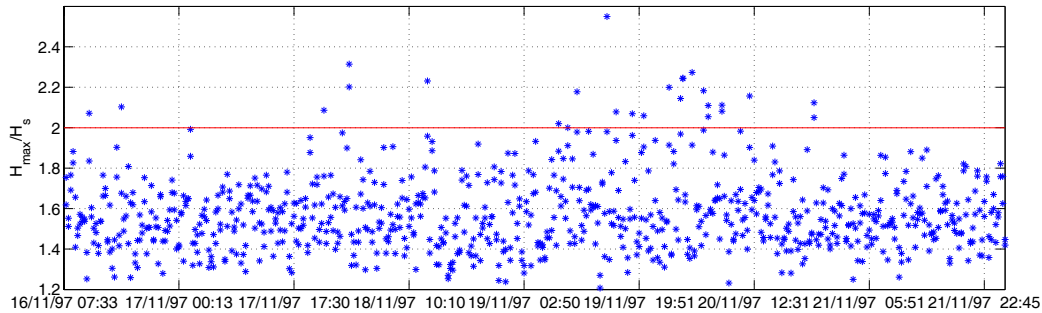


Figure 1.4: Analysis of a storm recorded at *North Alwyn* on November 16th till 21st, 1997, maximum $H_s = 10.67$ m, maximum $H_{max} = 22.03$ m, maximum $H_{max}/H_s = 2.55$ (20-minute records). Within five days, 21 waves with $H_{max}/H_s > 2$ are observed, confirming that Rogue Waves are rather normal events.

1.4 Objectives and Outline of the thesis

The overall aim of this thesis is to investigate the relevance of Rogue Wave impacts on marine structures. Both, experimental and numerical methods are applied to analyze the responses of selected offshore structures.

In this chapter, the importance and probability of occurrence of Rogue Waves is addressed and examples of Rogue Waves are presented. As demonstrated by the analysis of a five day storm recorded at *North Alwyn*, Rogue Waves are normal incidents. Thus, the impact of Rogue Waves will be analyzed both experimentally and numerically.

In chapter 2, new methods for the generation of Rogue Wave sequences in a physical wave tank are developed. A target wave train is synthesized based on the definition of target wave parameters. In a small wave basin, a new experimental optimization approach is applied, optimizing the wave train in order to satisfy all given parameters. The resultant wave sequence is transferred to a larger wave basin for the investigation of wave-structure interactions.

Chapter 3 introduces the offshore structures used to investigate Rogue Wave impacts. The basic principles of the three programm systems applied for the calculation of structure responses and the model test setup are described.

The bending moments and motions of two ships, a Floating production ship and a crane vessel, due to Rogue Wave impacts are analyzed in Chapter 4. Time-domain results are discussed with respect to frequency-domain analysis and rule values from classification societies.

Chapter 5 presents the splitting forces and motions of a semisubmersible in extreme waves. For the investigation of wave-structure interaction, wave sequences generated by the new optimization approaches presented in chapter 2 are applied. Experimental and numerical results are compared to traditional methods for design and discussed with regard to Rogue Wave impacts.

Chapter 6 is dedicated to the numerical simulation of wave propagation. Different approaches, based on potential theory and on the Reynolds-averaged Navier-Stokes equations, are introduced, to model a numerical wave tank. A new coupling approach for the fast and accurate simulation of nonlinear wave evolution is proposed, combining the advantages of both numerical strategies. This coupling provides the basis for the time efficient and accurate investigation of wave-structure interaction and wave breaking.

Chapter 7 summarizes the findings of the work. Perspectives for future developments and applications close the thesis.

1.5 General remarks

Throughout this thesis, three physical wave tanks are referred to:

- Small wave tank at the Technische Universität Berlin (TUB) – tank dimensions: length 15 m, width 0.3 m, water depth 0.4 m, flap type wave generator
- Large wave tank at the Technische Universität Berlin – tank dimensions: length 80 m, width 4 m, water depth 1.5 m, piston type wave generator
- Towing tank at the Hamburg Ship Model Basin (HSVA) – tank dimensions: length 300 m, width 18 m, water depth 5.6 m, double flap wave generator.

The Rogue Wave measured at the *Draupner* Platform located in the North Sea on January 1st, 1995, as given in Fig.1.1, will be referred to as *New Year Wave* in the thesis.

Chapter 2

Optimization of Rogue Wave Sequences

Ocean waves vary in shape and size determined by height, length, propagation velocity and direction. These irregularity of ocean waves can be described with a random wave model, where the sea state is supposed to consist of a superposition of component waves, each with its own amplitude, frequency and direction of propagation. However, to investigate the impact of extreme (annual probability of exceedance 10^{-2}) or abnormal (annual probability of exceedance 10^{-3} to 10^{-4}) waves, a deterministic approach to model these conditions within an irregular sea state is required, as with statistical methods extreme wave events may not be covered.

Is the highest wave really the worst, or is the wave steepness or the grouping of waves more relevant? Current research focuses on answering these and related questions. Thus, Buchner and Voogts (2004) investigate impacts of steep waves on an FPSO bow and conclude that the wave steepness is a critical parameter for loads. Also Clauss et al. (2004a) analysis capsizing phenomena in Rogue Wave groups. For these model tests, techniques for the generation of wave scenarios with predefined wave pattern and predefined local wave characteristics are required. Therefore, the scope of this chapter is to provide methods for the generation of deterministic wave sequences to answer such questions by model tests in the wave tank.

Since conventional numerical methods are still not accurate, or if accurate not fast enough to generate special wave environments, as new alternative an *experimental optimization* approach for synthesizing deterministic wave sequences is presented. The advantage of an *experimental optimization* process is the inherent inclusion of all nonlinear wave effects by using a physical wave

tank. The basic idea is to optimize wave sequences in a small wave basin and transfer the final signal to a large wave basin where tests with appropriate scaled models are conducted.

- First, target parameters such as wave height, wave length, period and crest elevation at a particular time are defined for a wave group. Starting with a random phase distribution in frequency domain the phases are optimized in order to satisfy the target parameter in time domain resulting in a target wave sequence.
- From this optimized target wave sequence a first control signal for the wave generator is calculated through linear wave theory (*linear optimization* approach), and the wave sequence is registered in a physical wave tank. Since nonlinear effects like wave-wave interaction and wave breaking are insufficiently considered by the generation model, the measured wave train may differ from the target parameters defined. Nevertheless, this control signal can be used for the realization of harsh wave environments in the wave tank.
- To improve the accuracy of the measured wave sequence at the target location, the control signal is iteratively improved by a fully automated *experimental optimization* process, controlling the wave generator, measuring and analyzing the created waves and modifying the control signal. As a result of this optimization process, a control signal for the generation of a wave train satisfying all target parameters is obtained.
- Knowing the transfer functions of the wave generators, both of the small and of the large wave tank, the wave sequence is transferred to the large wave basin, thus enabling the analysis of wave-structure interaction in well defined wave sequences at a larger scale.

Since the *experimental optimization* process requires the conduction of many iteration cycles, the entire experimental process is automated. Therefore, the wave train is optimized using a small wave basin equipped with a fully automated wave maker, that can be operated unmanned 24 hours a day. The transfer of the control signal from the small tank to a large basin is made feasible, since the geometric similarity of the waves in both tanks is ensured – in particular, the wave steepness as a key parameter for wave propagation is chosen identical. The small wave tank of the TUB is equipped with an electrically driven flap type wave generator and the large wave basin has a

hydraulically driven piston type wave maker. From the water depth of both tanks follows a geometric scale of 1:3.75 and a time scale of $1 : \sqrt{3.75}$.

As the transfer of a wave train from the small tank to the large wave basin is intended, the frequency range for the spectrum in the tanks has to be chosen accordingly. Thus, the selected frequency range is 4 ... 15 rad/s for the small and 2.05 ... 7.75 rad/s for the large wave basin.

2.1 Linear optimization approach for the synthesis of Rogue Wave sequences

The first step in generating deterministic wave sequences is the description of the target wave sequence by definition of target parameters. As an example, a single high wave is synthesized in a random JONSWAP sea state with significant wave height $H_s = 13$ m, peak enhancement factor $\gamma = 1$ and peak period $T_p = 13$ s. The target parameters of the i^{th} waves are defined as:

$$\begin{aligned} f_1 &= \left(\frac{H_i - H_{target}}{H_{target}} \right)^2 \\ f_2 &= \left(\frac{T_i - T_{target}}{T_{target}} \right)^2 \\ f_3 &= \left(\frac{\zeta_{ci} - \zeta_{c target}}{\zeta_{c target}} \right)^2 \\ f_4 &= \left(\frac{t_i - t_{target}}{t_{target}} \right)^2 \end{aligned}$$

f_1, f_2, f_3 and f_4 are the function values. $H_{target} = 2 \cdot H_s$ denotes the target wave height and $T_{target} = T_p$ is the related period (zero-downcrossing). $\zeta_{c target} = 0.6 \cdot H_{target}$ is the target crest height (horizontal asymmetry of the wave as defined by Kjeldsen (1983)) and t_{target} denotes the time of occurrence (see Fig. 2.1). Since wave height and period are defined, also the wave steepness, given by the ratio of wave height H to wave length L , H_{target}/L_{target} , is included in the optimization process.

The measure of merit f_m , to be minimized, is stated as:

$$\text{minimize } f_m(c) = \sum_{j=1}^n f_j$$

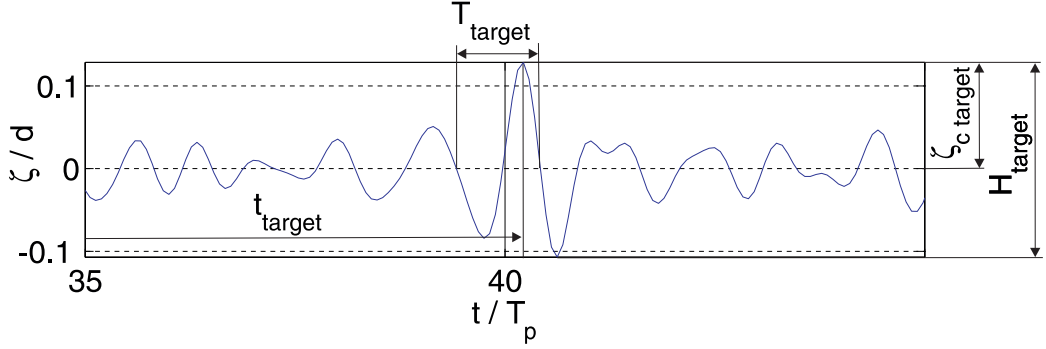


Figure 2.1: Target parameters of a Rogue Wave group integrated in irregular seas.

with n , the number of target parameters defined. c denotes the phase angles of the Fourier representation of the wave train which are modified during the optimization process. The amplitudes of the component waves are kept unchanged, thus ensuring that the JONSWAP spectrum is conserved.

In addition to the above target parameters, the maximum acceleration a_{max} , velocity u_{max} and stroke x_{max} of the wave board are defined as inequality constraints and are therefore not allowed to be exceeded. $x_B(t)$ denotes the motion of the wave board.

$$\begin{aligned} \max |x_B(t)| - x_{max} &\leq 0 \\ \max |\dot{x}_B(t)| - u_{max} &\leq 0 \\ \max |\ddot{x}_B(t)| - a_{max} &\leq 0 \end{aligned}$$

Starting with a random phase spectrum in frequency domain an initial time series of the target wave train is determined by inverse Fourier transformation based on linear wave theory. The wave train is analyzed by zero-downcrossing analysis and the objective function is calculated.

Applying the Subplex optimization method introduced by Rowan (1990), which is a generalization of the Nelder-Mead Simplex method for unconstrained minimization of multivariate functions, the phases of the wave spectrum are modified. The number of function evaluations required for convergence typically increases only linearly with the problem size, so for most applications the Subplex method is much more efficient than the Simplex method. For the Subplex method only function evaluations and no gradient

or curvature information of the measure of merit are required. The optimization terminates when a value of the measure of merit of less than 0.01 is achieved, ensuring that the target parameters are satisfied precisely. The optimization of the wave sequence follows the procedure as proposed in Clauss and Steinhagen (2000).

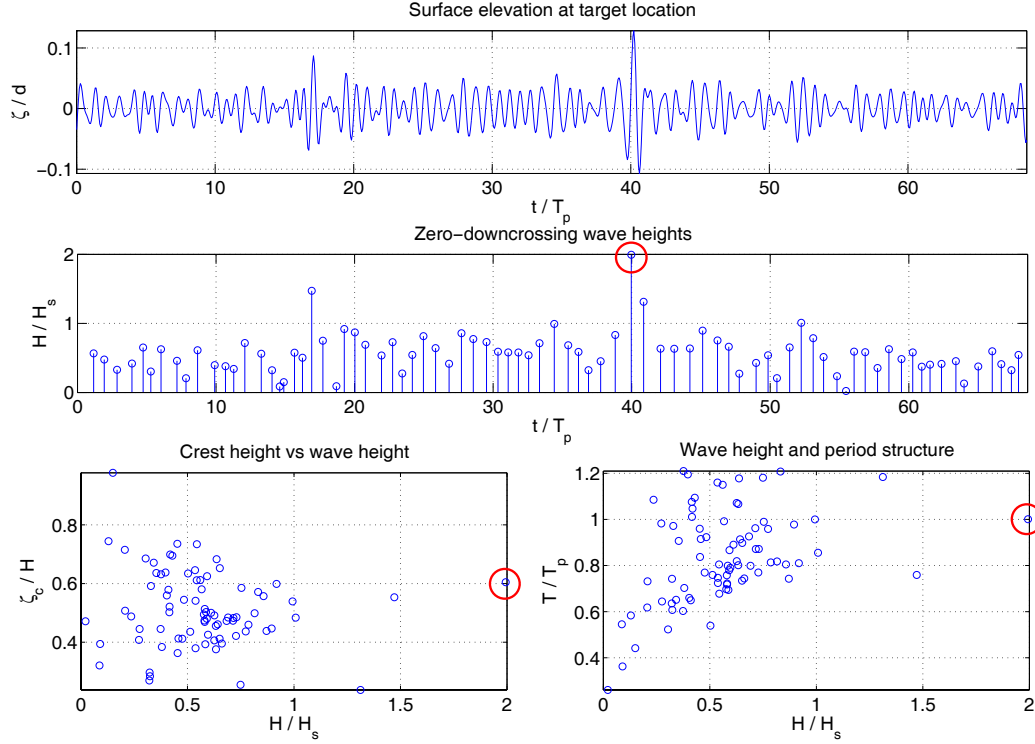


Figure 2.2: Result of the *linear optimization* for the generation of an initial control signal ($H_s = 13$ m, $T_p = 13$ s).

Fig. 2.2 presents the resultant optimized target wave train satisfying all target parameters. The nondimensional diagrams are related to a significant wave height of $H_s = 13$ m and a peak period of $T_p = 13$ s which corresponds to a geometric scale of 1:303 in the small wave tank and 1:81 in the large basin. In the diagram, the Rogue Wave with a wave height of $H_{max}/H_s = 2$ at the predefined time can be clearly detect. Bottom left hand diagram illustrates the crest asymmetry resulting in $\zeta_c/H = 0.6$ for the embedded Rogue Wave.

The control signal of the wave generator is calculated from the target wave train by linear transformation of the target wave train upstream to the position of the wave maker by phase shift in frequency domain, and multiplication by the corresponding hydrodynamic and electric transfer functions. The

electric transfer function of the wave maker is obtained by wave packet technology (Clauss and Kühnlein (1995)). As this initial control signal is based on linear wave theory, the measured wave train differs from the target wave train as nonlinear wave effects are expected in such severe seas ($H_s = 13$ m). In particular, the embedded Rogue Wave will deviate from the predefined parameters.

If these discrepancies are acceptable, the control signal generated with this optimization approach can be used directly for experiments in the wave tank. Since the generation process is based on linear wave theory, this method will be in the following denoted as *linear optimization* approach.

For a moderate sea state, Fig. 2.3 presents a Rogue Wave registered by the Japanese National Maritime Institute in the Sea of Japan off *Yura harbor* at a water depth of 43 m, at a sea state of $H_s = 5.09$ m with $H_{max} = 13.6$ m and a wave crest height of $\zeta_c = 8.2$ m (Mori et al. (2000)). This wave is realized in the small wave tank applying the *linear optimization* approach. The registrations in Fig. 2.4 show, how the Rogue Wave develops on its way to the target position at $x = 7$ m. Comparison with full scale data is satisfactory. Furthermore, this *linear optimization* approach will be used in chapters 4 and 5 for the synthesization of control signals to investigate motions and structural loads of offshore structures.

For the deterministic investigation of wave-structure interactions, waves complying exactly with the predefined parameters may be required. Therefore, in the following section an *experimental optimization* process is introduced to fit the measured wave train, based on the *linear optimization*, to the selected parameters.

In comparison to the optimization of waves in a numerical wave tank (Steinhagen (2001)), one can be sure, that all nonlinearities are included in this hybrid process, as real waves are generated.

2.2 Experimental optimization of a single high wave embedded in irregular seas

For the *experimental optimization* the small wave tank at TUB with a water depth of 0.4 m is used and a new electrically driven wave generator capable of continuous and fully automated operation has been developed and built. Settle down time of the wave tank is short, thus enabling many iteration cycles per day.

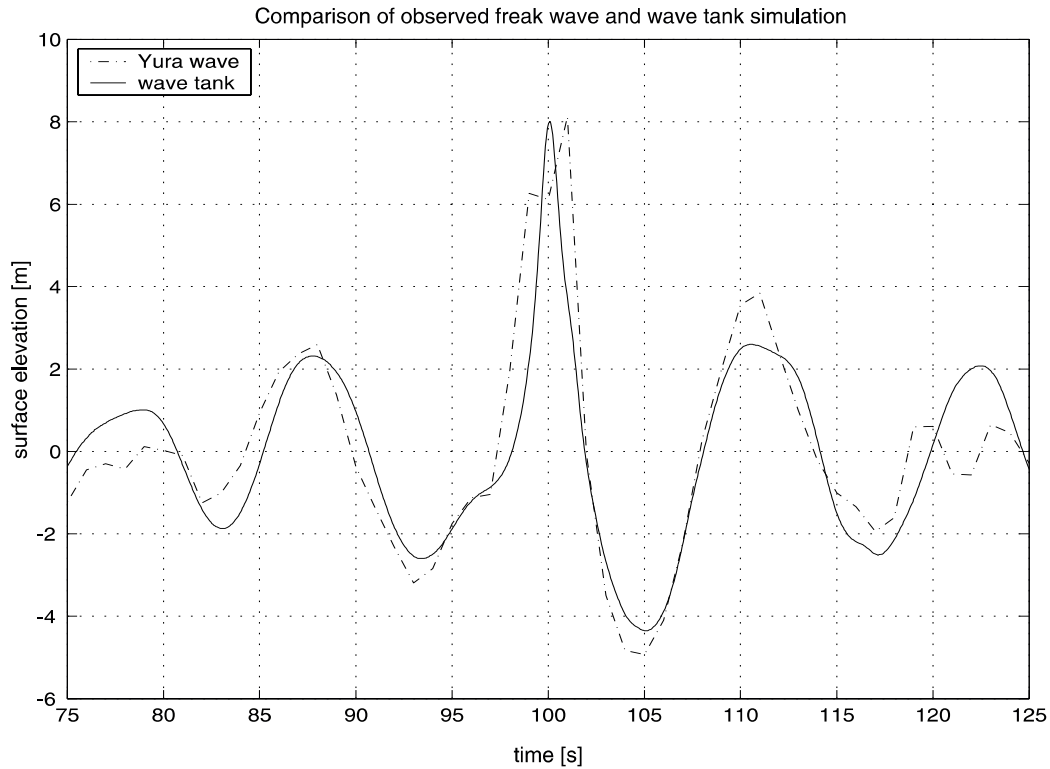


Figure 2.3: Comparison of the recorded *Yura wave* presented in chapter 1 to the wave tank realization. The control signal for the experiment is generated by the *linear optimization* approach.

Within the *experimental optimization* process only the wave environment close to the embedded Rogue Wave is modified. Therefore, the discrete wavelet transformation (González Sánchez et al. (1996)) is introduced into the optimization process which allows local (temporal limited) changes to the control signal. The discrete wavelet transform samples the signal into several decomposition levels and each resulting coefficient describes the wave in a specific time range and frequency bandwidth.

Fig. 2.5 presents the initial control signal of the optimization process and the associated 3-scale discrete wavelet transform. As wavelet, a so-called symlet with 16 coefficients, as introduced by Daubechies (1988), is selected. The third decomposition level of the wavelet transform is composed of the approximation coefficients c^3 and the detail coefficients d^1 , d^2 and d^3 from the previous decomposition levels. Due to the use of the wavelet transform the number of free variables can be significantly reduced if only approximation and detailed coefficients of the third decomposition level c^3 and d^3 are

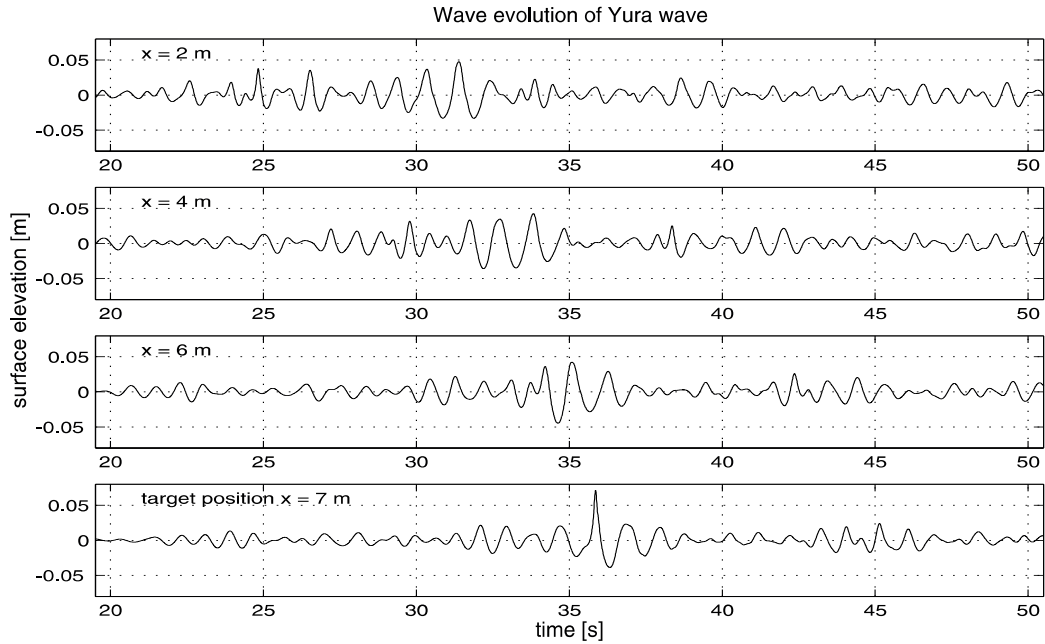


Figure 2.4: Evolution of the *Yura wave* in the wave tank at selected positions. The wave train is synthesized based on target parameters using the *linear optimization* approach at scale 1:112. Full-scale wave data have been collected by National Maritime Research Institute, Japan, Mori et al. (2000). The Rogue Wave develops from a rather unsuspecting looking wave group.

modified. These coefficients contain most of the wave energy, i. e. values of these coefficients are largest.

In the example given, the original time-trace consists of 2548 time steps. The corresponding 3-scale discrete wavelet transform has the same number of coefficients, where half of the coefficients belong to the detail coefficients d^1 , a quarter to the detail coefficients d^2 , and an eighth to detail coefficients d^3 and to the approximation coefficients c^3 respectively. From the coefficients c^3 and d^3 only those are considered, that are valid for the time frame when the Rogue Wave is generated (coefficients 85–129 and 404–448). Thus, the number of free variables to be considered in the optimization process is reduced to 90.

The objective function of the *experimental optimization* is adapted from the generation of the target signal. The fitting of the wave train is achieved by applying the Subplex optimization method. Nonlinear free surface effects are included in the fitting process since the values of the objective function are determined from the wave tank experiment. Fig. 2.6 shows the fully automated optimization scheme of steering the wave maker, analyzing waves

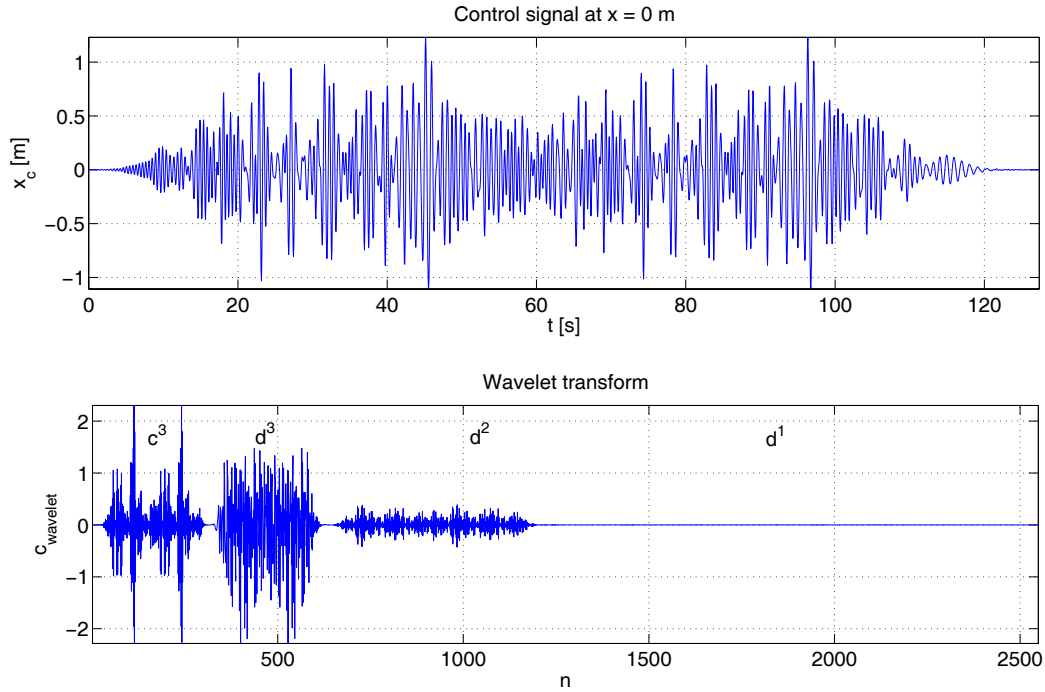


Figure 2.5: Initial control signal ($x_c(t)$) of the optimization process and associated 3-scale discrete wavelet transform. For the *experimental optimization* of the embedded Rogue Waves 90 wavelet coefficients are considered (coefficients 85–129 and 404–448).

and modifying the control signal until convergence is achieved.

The optimization terminates when a value of the measure of merit of less than 0.003 is achieved. Depending on the number of target parameters and the quality of the starting control signal, a minimum of 500 iteration steps is required, corresponding to approximately 20 hours time. As a result of the optimization, Fig. 2.7 presents the improved wave train and the corresponding zero-downcrossing wave heights. The final wave sequence satisfies all given parameters within the defined degree of accuracy.

Fig. 2.8 presents the synthesis of the wave sequence during the *experimental optimization* process. At the bottom of the Figure (blue line) the initial wave sequence (control signal from *linear optimization*) is displayed which develops to the experimentally optimized wave sequence with the embedded Rogue Wave (top, red line). Now, this procedure enables the generation of arbitrary but deterministic wave sequences in the small wave basin.

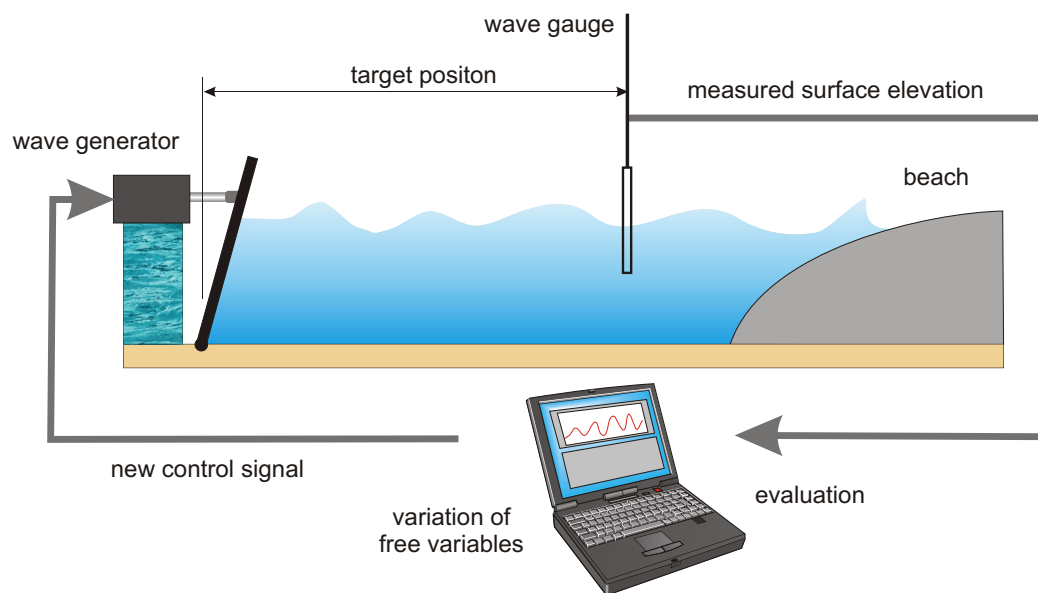


Figure 2.6: Computer controlled optimization of waves: The wave sequence is automatically created, measured, evaluated and modified until convergence is achieved, i. e. the target wave train is generated.

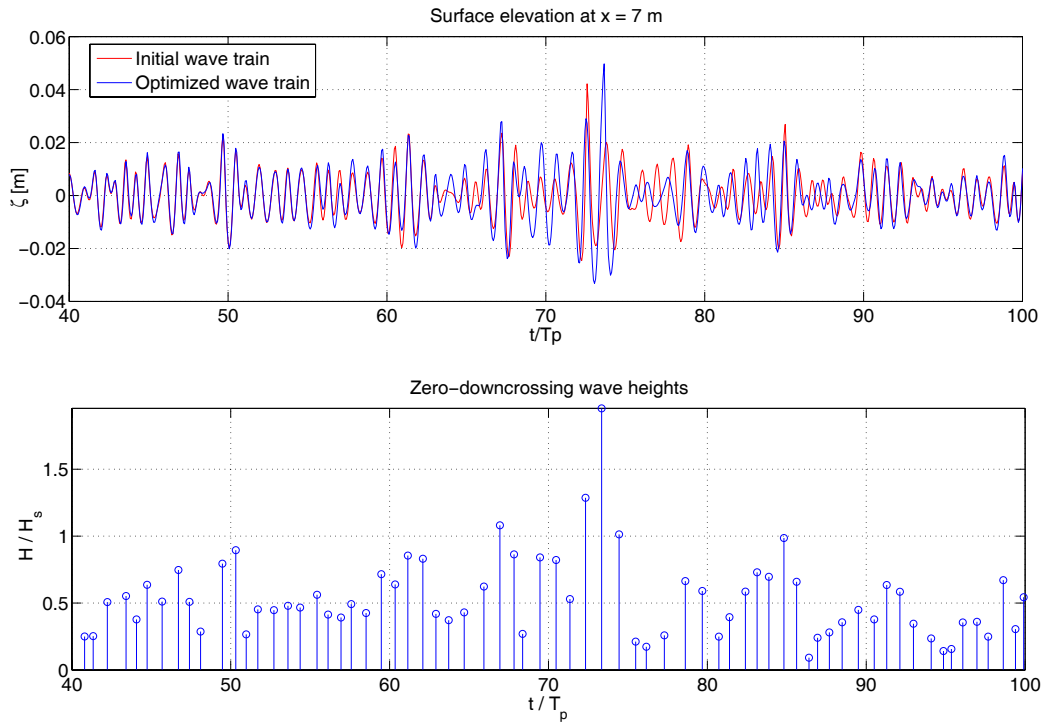


Figure 2.7: Improved wave train and corresponding zero-downcrossing wave characteristics: Final step 1690 of the *experimental optimization* in the small wave tank at scale 1:303. The optimized wave train (blue) satisfies all pre-defined target characteristics: $H_s = 13$ m, $T_p = 13$ s, $H_{target} = 2 \cdot H_s$, $T_{target} = T_p$, $\zeta_{c,target} = 0.6 \cdot H_{target}$ and $t_{target} = 55$ s.

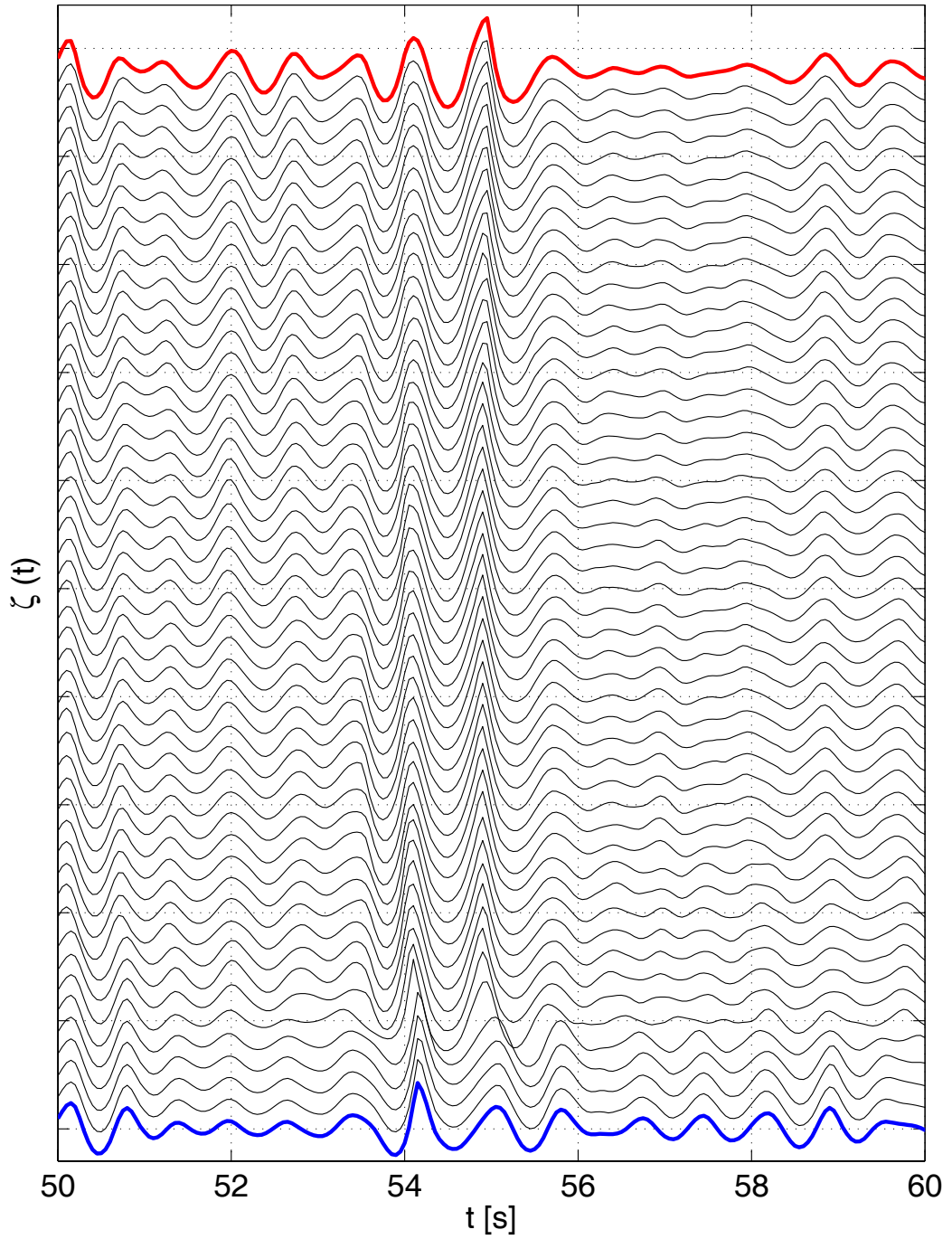


Figure 2.8: Synthesis of the wave sequence showing 50 iteration steps. Blue: Starting signal for the *experimental optimization* – Red: Final wave sequence satisfying the predefined parameters: $H_s = 13$ m, $T_p = 13$ s, $H_{target} = 2 \cdot H_s$, $T_{target} = T_p$, $\zeta_{c target} = 0.6 \cdot H_{target}$ and $t_{target} = 55$ s.

2.3 Transfer of the wave signal from the small to the large wave basin

The optimization of deterministic wave sequences described in the previous section is carried out in the small wave basin, since this basin is fully automated, and decay time after each run is quite short, thus enabling many iteration cycles per day. In addition, a large wave basin is quite expensive to run and the danger of damaging the wave generator still remains. However, this small wave basin is not suitable for the investigation of wave-structure interaction as viscous effects become more dominant at small model scales (such as 1:303). Wave propagation itself is relatively insensitive to viscous effects as inertia forces are dominant. Therefore, the idea is to optimize wave sequences in the small wave basin and transfer the final signal to the large wave basin where model tests are conducted at an adequate model scale (here 1:81).

This implies that the waves have to propagate in the large wave tank identically as in the small wave basin but in a scaled manner. This is indeed the case, as the wave steepness $k\zeta_a$ (wave number $k = \frac{2\pi}{L}$, wave amplitude ζ_a) which characterizes wave propagation, is equal at both scales. The scaling is performed according to Froude's law, i. e. the geometric properties wave length, wave height and water depth are scaled linearly and time according to the square root of scale.

To transfer the control signal from one wave tank to the other, the electrical, hydraulic and hydrodynamic transfer functions of the wave generators have to be known precisely. The determination of these transfer function is crucial for the accuracy of the conversion. The electrical transfer function of the small flap type wave generator and the transfer function of the large hydraulic driven piston type wave generator are obtained by wave packet technology (Clauss and Kühnlein (1995)) and smoothed by regression. The hydrodynamic transfer functions are modelled using the Biésel function (Biésel and Suquet (1951)), relating the wave board stroke to the wave amplitude at the position of the wave maker (see also the appendix).

Dividing the Fourier transform of the control signal of the small wave tank by the associated electrical and hydrodynamic transfer function, the Fourier transform of the wave sequence at the position of the wave maker is obtained. Inverse Fourier transformation gives the wave elevation and by multiplication by scale and modifying the time step size according to the square root of scale the wave sequence at the large wave board is calculated. Multiplication of the Fourier transform of the wave train by the hydraulic and

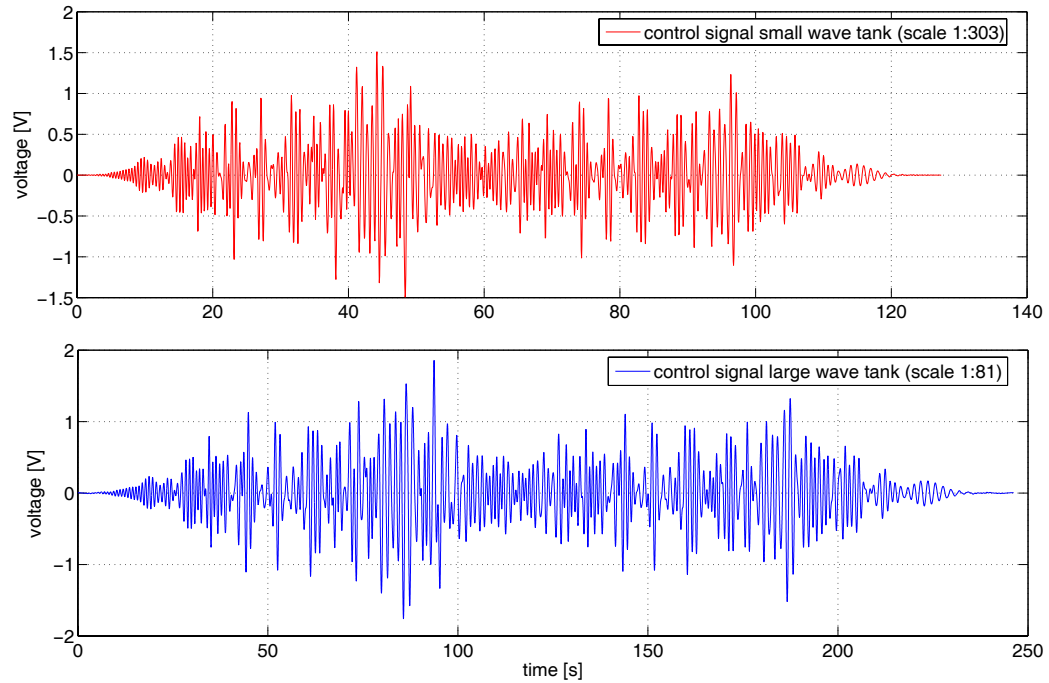


Figure 2.9: Comparison of the control signals of the small and the large wave tank. Although the signals look different an identical wave sequence is generated in both tanks.

hydrodynamic transfer function of the piston type wave maker and subsequent inverse Fourier transformation yields the control signal for the large wave basin. With this control signal, the wave sequence is generated in the large wave basin and registered at the scaled target position $x = 26.25$ m. In Fig. 2.9, the control signals for both wave basins are presented. The control signals differ in length and shape, nevertheless identical wave scenarios are generated in the small and the large wave tank.

Fig. 2.10 presents the simulation of the same wave sequence measured in the small wave basin (flap type wave generator, $d = 0.4$ m) and in the large wave basin (piston type wave generator, $d = 1.5$ m). Good agreement between both simulations is observed. In a next step, this optimized and transformed wave sequence is used to investigate wave-structure interactions (see chapters 4 and 5).

Fig. 2.11 shows the optimized and transferred wave train, measured in the large wave tank nondimensioned by significant wave height and period. In the diagram one can clearly detect the Rogue Wave with a wave height of $H_{max}/H_s = 1.94$ at the predefined time. Bottom left hand diagram illustrates

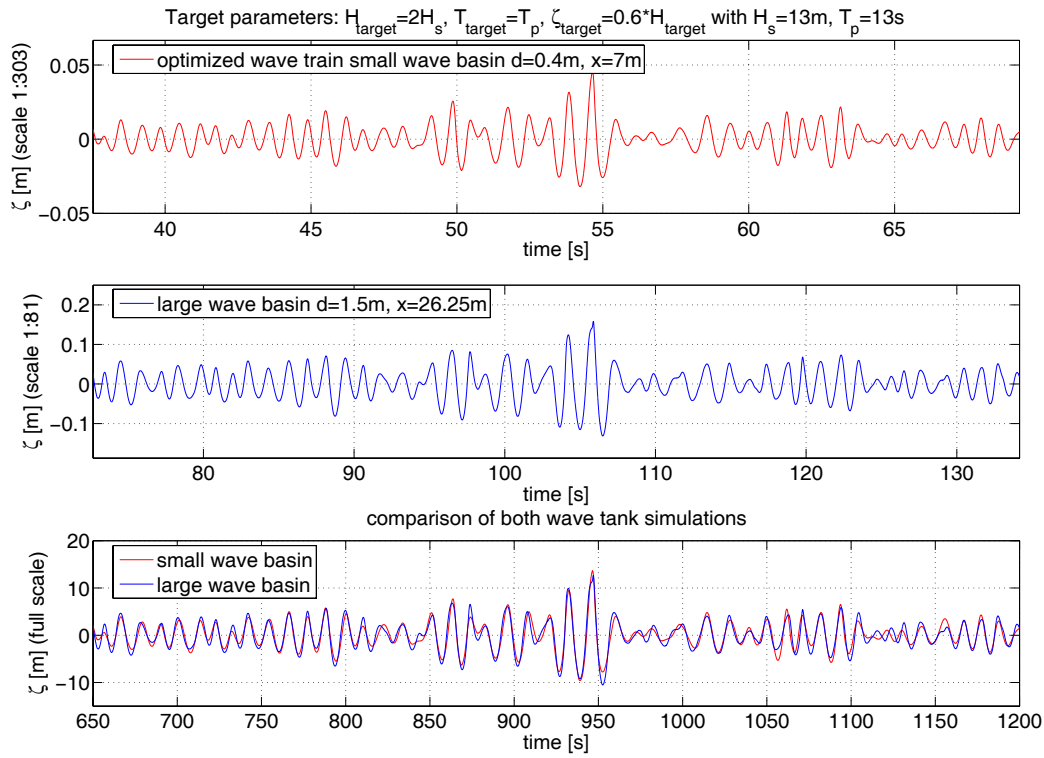


Figure 2.10: Comparison of realized wave in the small wave basin (flap type wave generator, $d = 0.4$ m) to the same (scaled) wave in the large wave basin (piston type wave generator, $d = 1.5$ m) after transformation of the control signals. Good agreement between both wave sequences is observed.

the crest asymmetry resulting in $\zeta_c/H = 0.58$ for the embedded Rogue Wave. Now, with this new method all kind of waves within a realistic environment can be realized in a larger wave basin.

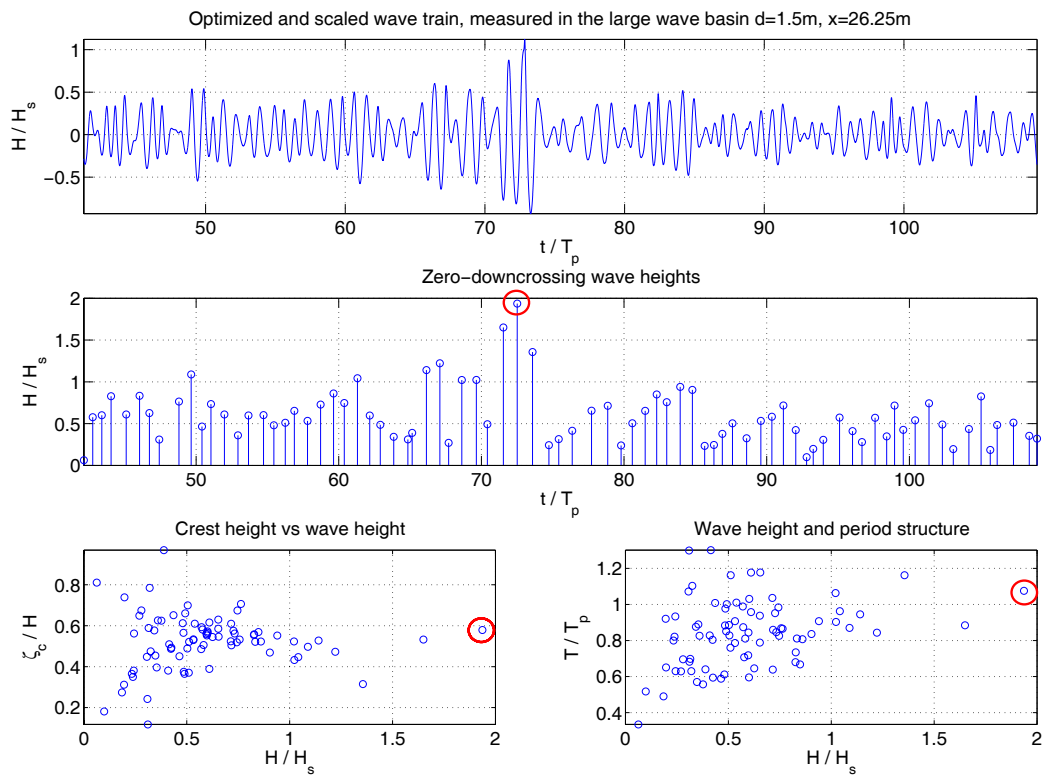


Figure 2.11: Optimized and scaled wave train, measured in the large wave tank (scale 1:81). The embedded Rogue Wave satisfies the predefined target parameters (red circles).

2.4 Phase-amplitude iteration scheme for the generation of deterministic wave scenarios

Alternatively, to the optimization approaches proposed in the previous section, in this section another experimental iteration scheme is presented. This scheme modifies the phase angles and amplitudes of the control signal in frequency domain dependent on the differences between target and measured wave train.

This handy experimental wave generation scheme is based on the method proposed by Chaplin (1996) who improved the accuracy of a focused wave train: Starting with a given target wave train (a wave packet at the concentration point) and the corresponding control signal for the wave generator, the wave train is recorded in the wave basin. From the comparison of the recorded phase angles ($\varphi_{recorded}$) with the target phase angles (φ_{target}) in frequency-domain, new phase angles of the control signal are calculated:

$$\varphi_{new} = \varphi_{old} - 2 \cdot (\varphi_{target} - \varphi_{recorded}) \quad (2.1)$$

The phase shift applied is the opposite phase shift determined by comparison of target phase angles and recorded phase angles. This iteration scheme was successfully applied by Chaplin to the generation of a wave packets (in-phase superposition of component waves).

In this thesis, the iteration scheme is extended, in order to generate irregular wave sequences. The target wave sequences can either be synthesized from parameters applying the optimization approach presented in section 2.1, or can be records from full scale measurements. The target phases are calculated from the target signal by Fourier transform and phases are modified according to equation 2.1. In addition to the original scheme, also the amplitudes of the component waves are scaled with the ratio of target amplitude to recorded amplitude:

$$a_{new} = a_{old} \cdot \left(\frac{a_{target}}{a_{recorded}} \right) \quad (2.2)$$

As an application, the *New Year Wave* (see also Fig. 1.1) is generated at different model scales 1:81, 1:175 and 1:250. From the target wave train a

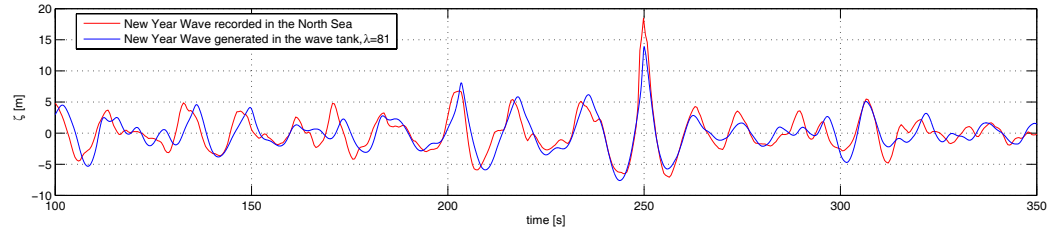


Figure 2.12: Optimized wave train at target position ($x = 30$ m, water depth $d = 1.5$ m) after two iteration steps of the phase-amplitude iteration scheme in comparison to recorded *New Year Wave* sequence (wave tank simulation at scale 1:81, presented as full scale data).

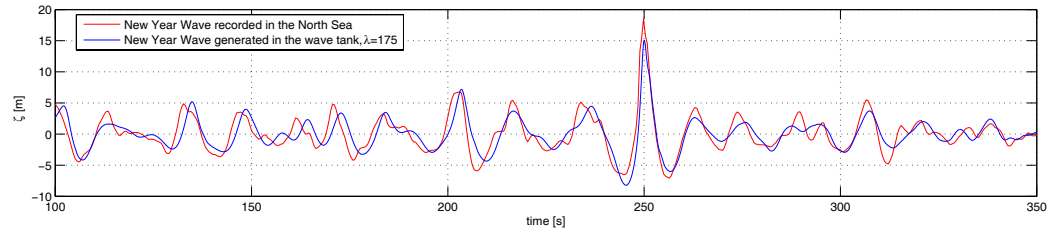


Figure 2.13: Optimized wave train at target position ($x = 6$ m, water depth $d = 0.4$ m) after 23 iteration steps in comparison to recorded *New Year Wave* sequence (wave tank simulation at scale 1:175, presented as full scale data).

first control signal is calculated by linear wave theory. The wave is generated in the wave tank and the phase-amplitude iteration scheme is applied.

Fig. 2.12 presents the wave train optimized in the large wave tank at TUB with the phase-amplitude experimental iteration scheme. Model scale 1:81 is selected in order to match with the model scale selected for the investigation of the offshore structures in Rogue Waves.

Fig. 2.13 and Fig. 2.14 present the results of the iteration process in the small wave tank at a water depth of 0.4 m. For model scale 1:175 the water depth of 0.4 m corresponds to 70 m at full scale and at 1:250 to 100 m.

The simulations at all three model scales show that with the phase-amplitude iteration scheme complex wave sequences can be realized at different wave tanks and model scales. The number of iterations required to obtain good results depends on the quality of the starting control signal. For scale 1:81, a control signal is calculated based on linear theory and after only two iteration steps the wave train is in good agreement with the target wave train. For the optimization at scales 1:175, 1:250 respectively, a control signal for a wave

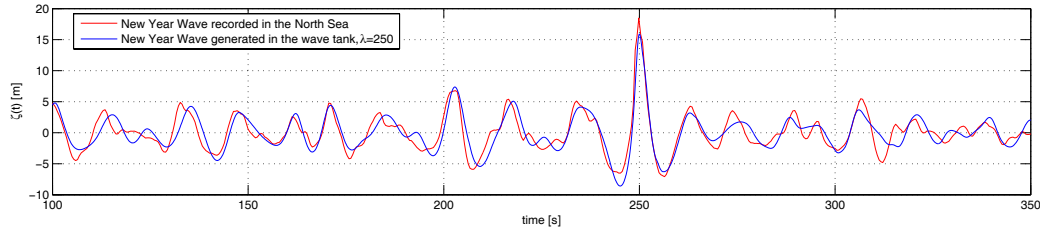


Figure 2.14: Optimized wave train at target position ($x = 6$ m, water depth $d = 0.4$ m) after ten iteration steps in comparison to recorded *New Year Wave* sequence (wave tank simulation at scale 1:250, presented as full scale data).

packet is used as a starting point, but after ten, 23 respectively, iteration steps good agreement with the target wave sequence is observed. The differences in the maximum wave height of the experimentally simulated and the recorded *New Year Wave* can be attributed to the limited bandwidth of the wave generators and to the fact that the *New Year Wave* is close to breaking due to high frequency contents.

This iteration process can be used for the fast (only a few iteration steps) and precise generation of wave trains. Due to the limited number of iterations needed this method can also be applied to large wave tanks. If a better accuracy is required for local wave characteristics the wave train can further be improved by the *experimental optimization* process described in section 2.2. Both methods can be used independently or in combination.

2.5 Conclusive comparison of optimization approaches

New methods for the generation of deterministic wave sequences in a wave basin for the investigation of wave-structure interaction have been introduced.

Starting with the definition of target parameters, an initial control signal is created applying the *linear optimization* approach. Using the Subplex optimization, the wave sequence is improved experimentally in a small wave tank, satisfying all target parameters. The final control signal is transferred to a large wave basin resulting in an identical, but scaled, wave sequence.

The transfer of control signals from one tank to another is possible as the following conditions are satisfied:

- Geometrical dimensions like water depth and target position are scaled by model scale
- Time is scaled according to Froude's law by the square root of model scale
- Wave steepness is identical at both scales
- Corresponding frequency ranges of wave makers are selected
- Transfer functions of wave makers are precisely known or determined

Note, that the transfer from the small to the large wave tank is possible, although different types of wave generators are used. Thus, the costly large wave basin is used for specific seakeeping tests with defined wave sequences, whereas the small wave tank optimizes signals for the next test campaign.

Alternatively, to the *linear* and *experimental optimization* procedure the handy phase-amplitude iteration scheme is developed. This method allows the fast and precise generation of predefined wave sequences. The procedure is applicable in large wave tanks as only a few iteration cycles are required. Depending on the scope of the planned investigation and therefore depending on the accuracy requirements the proposed wave generation methods can be applied independently or in combination.

Chapter 3

Experimental and Numerical Investigation of Offshore Structures

Although modern numerical methods are useful for the determination of design loads, hydrodynamic model tests are still indispensable for:

- Validation of new developed numerical simulation tools predicting system responses in general
- Verification of calculation results relying on established codes
- New types of structures, to confirm that no important hydrodynamic action has been overlooked
- Investigation of nonlinear or extreme events not sufficiently covered by numerical approaches such as slamming, green water effects, ringing, run-up effects, Rogue Wave impacts, combined effects of wind, waves and current.

In the following chapters, different offshore structures are experimentally investigated with respect to their responses due to Rogue Wave impacts. The experimental data are to be compared with results from numerical simulations based on different program systems. Thus, in this chapter, the ships used in the investigations are introduced and the model test setup is illustrated. Then, a short introduction into the codes applied for the numerical investigations is given.

3.1 Investigated structures

3.1.1 FPSO

Within the last 15 years, a growing trend to use ship type structures for offshore oil production can be observed. While in 1991 only 24 FPSOs (Floating Production Storage and Offloading ships) were in service, ten years later in 2001, 72 FPSOs were on location. An FPSO is an offshore production facility that stores crude oil in tanks located in the hull of the vessel. Periodically, the crude oil is offloaded to shuttle tankers and transported to shore. Actually, more than 100 units are installed in water depths up to 1400 m and many are under construction or ordered (Nutter and Albaugh (2004)). The advantages of FPSOs leading to this increase in numbers are the large deck area, the possibility to store huge amounts of crude (in combination with shuttle tankers saving the installation of pipelines), a huge payload and the ship type structure itself with low construction costs, fast delivery times and favorable seakeeping behavior. FPSOs are often based on old tankers which are overhauled and converted, thus reducing capital investments in combination with a short construction period in comparison to a newly build design.

Nowadays, FPSOs are widely used, in particular for deep water and for harsh offshore environments. Within the next years, a growing demand is expected for FPSOs for water depths of more than 1500 m, where a pipeline export infrastructure does not exist (Gorf (2004)). The investigation in this thesis focusses on a DP-FPSO (Dynamically Positioned FPSO) being a merger between a harsh weather FPSO and a dynamically positioned ultra deep water drilling ship (Dijk (2003)). A feasibility study proves that dynamic positioning systems can deal with extreme conditions (Dijk (2004)). The advantage of using a DP-FPSO is the elimination of mooring systems and the easier relocation.

For the design and dimensioning of the hull, existing shipbuilding rules and standards are applied. These rules are empirically based and are intended to be applicable for a variety of ship types. Classification rules typically consider the North Atlantic wave environment as a design premise and are based on a 20 years return period corresponding to a significant wave height in the range of 16.5 m to 18.3 m (Terpstra et al. (2001)). The design of ships based on empirical terms is in contrast to common practice in the offshore industry where direct calculation methods are applied (MacMillan (2001)). During storms, FPSOs stay on station and weathervane, whereas ships try to avoid severe storm conditions by choosing a more favorable route. In consequence,

FPSOs are exposed more often to extreme wave conditions than ships. This exposure to extreme weather conditions in combination with high topside loads and a more box shaped form of new built FPSOs may lead to structural loads that are not covered by standard design rules. Terpstra et al. (2001) found that for a new built FPSO, the rule values for the maximum still water bending moment and shear forces are exceeded by up to 95%. Therefore, Det Norske Veritas (2004) has published a new standard for the structural design of offshore ships where for the wave induced loads, calculations based on strip theory or the usage of a three dimensional diffraction program is recommended.

The main dimensions of the DP-FPSO investigated throughout the thesis are:

- Length over all $L_{oa} = 280.78$ m
- Length between perpendiculars $L_{pp} = 259.89$ m
- Breadth $B = 46$ m
- Draft $T = 16.67$ m
- Displacement $\nabla = 174000$ t
- Block coefficient $c_B = 0.87$

3.1.2 Crane vessel

Throughout the seventies, crane vessels were designed and built for the installation of jackets and topsides where heavy-lift operations are required. Most of these vessels are still operating and new ships are also put to service (e. g. *Saipem 3000* in 2003). Beside the traditional installation tasks, crane vessels are nowadays applied for the removal and disposal of decommissioned platforms and for the installation of underwater installations and offshore wind fields. Due to a large open deck area some crane vessels carry their loads to or off the location, avoiding lifting operations between two floating vessels (Terdre (2005)). In addition, crane vessels are applied for laying pipelines and as support vessel for underwater robots. Most crane vessels are dynamically positioned but can also be moored. The biggest crane ship, the *Derrick Barge 50*, lifts up to 2400 t. The shape of the crane ship used for this investigation is similar to the *Derrick Lay Barge 1601*, that was commissioned in 1974.

The main dimensions of the crane vessel are:

- Length over all $L_{oa} = 202.50$ m
- Length between perpendiculars $L_{pp} = 194.4$ m
- Breadth $B = 37.8$ m
- Draft $T = 10.10$ m
- Displacement $\nabla = 65314$ t
- Block coefficient $c_B = 0.88$

3.1.3 Semisubmersible

Semisubmersibles are characterized by a favorable seakeeping behavior and are used world wide for the exploration of oil fields and production. The semisubmersible *GVA 4000* is designed for effective drilling operations all over the year in the environmental conditions of the North Sea and North Atlantic. The maximum design wave height for the *GVA 4000* is a 33 m high wave (accidental limit state) demonstrating that the semisubmersible is designed for harsh sea conditions. The *GVA 4000* main structure comprises twin pontoons and four columns supporting the deck structure.

Semisubmersibles with more hulls are sensitive to horizontal forces and the structural loadings can become considerable. This is due to hydrodynamic forces, called splitting forces, acting in opposite directions on the hulls. Therefore, the lower hulls of the *GVA 4000* are connected by two horizontal bracings. The *GVA 4000* is a very successful design that was built four times. The displacement and draft of the *GVA 4000* is variable due to large ballast tanks. During transit, both submerged hulls are at the water surface and draft is only 7.2 m, ensuring accessibility to ports or docks and a high transit speed due to reduced resistance. For drilling operation, ballast tanks are flooded improving the seakeeping behavior. In case of extreme weather conditions, operation is abandoned and the draft is lessened by about 4.1 m, giving a larger airgap, i. e. a larger distance between wave crest and underside main deck. The airgap is critical for a semisubmersible as waves smashing into the deck structure can cause severe damages.

The main dimensions of the semisubmersible *GVA 4000* are:

- Pontoon length 80.56 m

- Pontoon beam 16 m
- Column spacing (longitudinal and transverse) 54.72 m
- Column diameter 12.9 m
- Height to main deck 41 m
- Draft (operation) 20.5 m
- Draft (survival) 16.2 m
- Displacement (operation) $\nabla = 25790$ t
- Displacement (survival) $\nabla = 22820$ t

3.2 Experimental setup

The model tests are performed in the large wave tank at TUB. Data acquisition and control of the wave maker is performed by a single computer system, ensuring time synchronization of steering, measuring and the repeatability of the experiment. For measuring the wave elevations, resistant type wave gauges are used. The motions of the models are registered by a dedicated video system introduced in the appendix, that is synchronized by the computer system. Structural loads, i. e. forces and moments are recorded by strain gauges as described in the appendix.

In the following, all these data, both calculated and measured, will be presented as full scale data.

3.2.1 Setup for the FPSO and for the crane vessel

Wooden models of both, the FPSO and the crane vessel, are built at scale $\lambda = 81$. The model tests are performed according to Froude's law, i. e. the geometric properties (length, width, height and water depth) are scaled linearly and time is scaled according to the square root of scale.

During the tests, the wave elevations, bending moments, heave and pitch motions of the vessels are recorded. For measuring the bending moments, the model of the FPSO is cut into three segments with intersections at $L_{pp}/4$ and $L_{pp}/2$ measured from bow (Fig. 3.1). The model of the crane vessel is intersected at midship as presented in Fig. 3.2.



Figure 3.1: Segmented model of the FPSO during tests in the wave tank, scale 1:81. Bending moments are registered at midship and at quarter length from bow.

At the intersections, the connecting steel elements on both sides are equipped with strain gauges for the registration of vertical bending moments. These moments consist of the contributions caused by vertical forces and by surge loads. Due to the fact that the entire system acts as a dynamic, oscillating system, the vertical position of the connecting elements is essential for the registration. To investigate this effect, the measuring devices of the FPSO ship can be attached to the model at different heights (Fig. 3.3). Measurements have been carried out both with connecting elements at deck level and at water line level.

The seakeeping tests are performed in head seas. Several severe wave conditions, such as the *New Year Wave* and variations of the *New Year Wave*, are realized to investigate the corresponding impact. The transfer functions of motions and loads are obtained by applying the deterministic wave packet technology (Clauss and Kühnlein (1995)).

3.2.2 Setup for the semisubmersible

A model of the *GVA 4000* is built from Plexiglas at scale 1:81. Heave, pitch and roll motions as well as airgap and splitting forces are key characteristics of semisubmersibles and are registered during the experiments. Model tests are carried out in head seas ($\beta = 180^\circ$) for the evaluation of motion behavior, and in beam seas ($\beta = 90^\circ$) for structural investigations (splitting forces).



Figure 3.2: Model of the crane vessel with the halves of the hull connected by strain gauges for the registration of the bending moments.

With exchangeable ballast weights in the columns (see Fig. 3.4), the draft of the semisubmersible can be adjusted to survival and operation conditions. Also the righting arm can be varied by modifying the vertical position of the weights.

The airgap is measured by wave gauges at different locations of the platform deck. For measuring the splitting forces, the cross bracing of the semisubmersible is equipped with strain gauges (see Fig. 3.4). Model motions are registered with the video system as given in the appendix. The advantage of this setup is, that no additional forces from the measuring equipment, such as forces caused by cable actuated position sensors, are affecting model motions.



Figure 3.3: Side view of the FPSO at midship: The vertical position of the connecting steel elements, which are equipped with strain gauges for the registration of the bending moments, can be changed (photo: measuring device for bending moments at water line level).

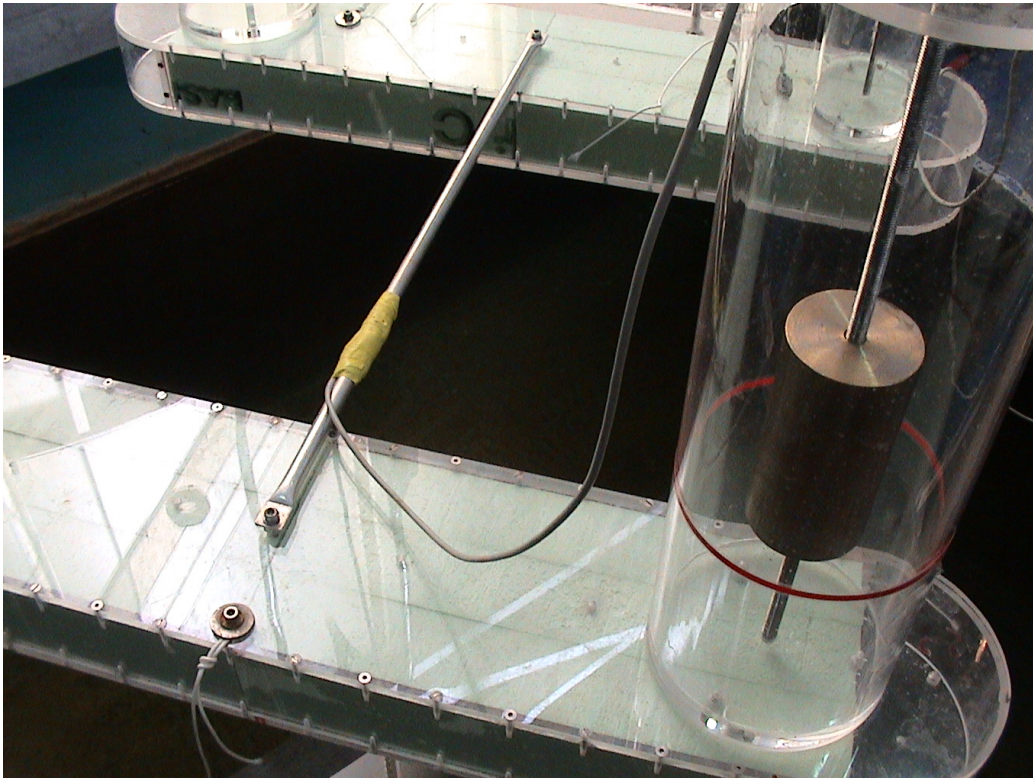


Figure 3.4: The main hulls of the semisubmersible *GVA 4000* are connected by a cross bracing equipped with strain gauges to register the splitting forces in waves. The ballast weights can be changed for different displacements and positioned at different heights.

3.3 Numerical methods for the simulation of motions and loads

For the numerical investigation of the vertical bending moments of the FPSO and the crane vessel as well as for the analysis of the splitting forces of the semisubmersible, three different programs are applied:

1. WAMIT
2. SEAWAY
3. IST-CODE (calculations carried out by Instituto Superior Tecnico, Lisbon, Portugal)

In the following, a short description of the three program systems with regard to the calculation of vertical bending moments and splitting forces is given.

3.3.1 WAMIT

For the evaluation of motions, forces and bending moments, the program system WAMIT (Wave Analysis, developed at Massachusetts Institute of Technology) for wave-structure interaction at zero-speed is applied (Newman (1985), WAMIT (1994)). In the program, a three-dimensional panel method using potential theory is implemented. Figs. 3.5 and 3.6 present the discretization of the FPSO and the crane vessel for the calculations. WAMIT solves the equation of motion in frequency-domain, and is applicable only for zero-speed problems. Results of motions and forces are given uniquely as response amplitude operators (RAO) by amplitude and phase. The program WAMIT allows for the analysis of generalized modes of flexural motions, in addition to the usual six degrees of rigid-body motions. To analyze bending moments of a vessel the ship is assumed to be a slender beam, with vertical displacement along the length. The deformation of the ship is modelled using mathematical mode shapes. Legendre polynomials $P_i(x)$, $i = 2, 3, \dots$, are found to approximate well the bending modes (Newman (1994)). The deflection line for each bending mode is given by the product of the calculated amplitude and the corresponding Legendre polynomial:

$$w_i(x) = s_{ia} \cdot P_{i-5}(x), \quad i = 7, 8, \dots \quad . \quad (3.1)$$

The indexing takes into account, that the first 6 indices are reserved for the conventional rigid body motions. For multiple bending modes, the total deflection results from complex superposition of the individual deflection lines. Twice differentiation of the deflection line, multiplied with the flexural stiffness, results in the bending moment of the ship:

$$M_b(x) = -w''(x) \cdot EI_y(x). \quad (3.2)$$

As will be shown in the following, the above WAMIT procedure is successfully applied to the analysis of vertical bending moments of stationary ships with high block coefficient (Clauss et al. (2004c)).

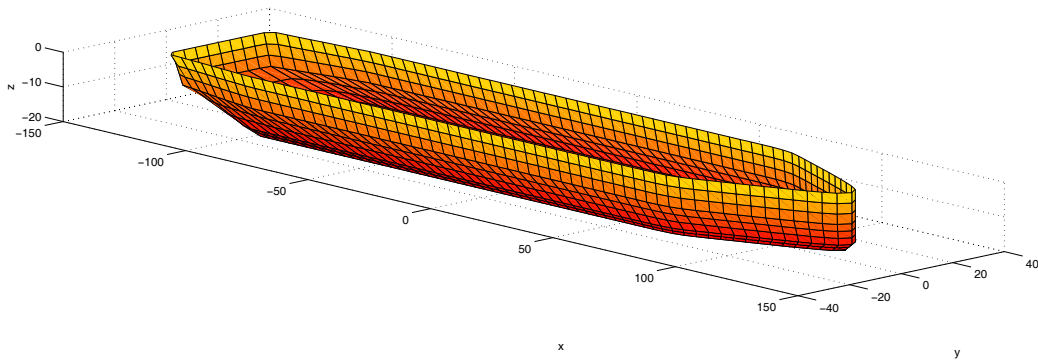


Figure 3.5: Discretization of the FPSO for the numerical analysis of motions and bending moments.

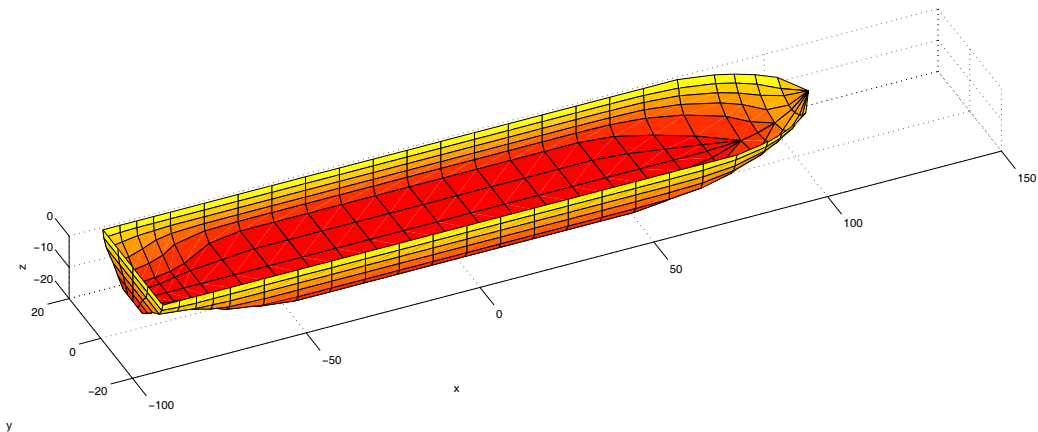


Figure 3.6: Crane vessel discretization for the analysis using WAMIT.

For the investigation of motions and splitting forces of the *GVA 4000* the wetted surface of the body is discretized into 760 panels (operation draft)

and 712 panels for survival draft. Dimensions and discretization of the semi-submersible *GVA 4000* at operation draft are presented in Fig. 3.7. The transfer function for the heave and pitch motion are calculated directly by WAMIT. The transfer function of the splitting forces is obtained from the difference of the forces acting on each hull:

$$RAO_{splitting\ forces} = (RAO_{forces\ side\ 1} - RAO_{forces\ side\ 2})/2, \quad (3.3)$$

where $RAO_{forces\ side\ 2}$ is calculated from the difference of the total horizontal exciting forces of the semisubmersible $RAO_{forces\ horizontal}$, and the forces acting on one side $RAO_{forces\ side\ 1}$ by:

$$RAO_{forces\ side\ 2} = RAO_{forces\ horizontal} - RAO_{forces\ side\ 1}. \quad (3.4)$$

The transfer function of the forces on one side $RAO_{forces\ side\ 1}$ is obtained by a separate WAMIT analysis, where only one side (hull and two columns) of the semisubmersible is considered.

The variation of the airgap can be calculated in time-domain as the difference of the heave motion $s_3(t)$ and the wave height $\zeta(t)$,

$$airgap(t) = s_3(t) - \zeta(t). \quad (3.5)$$

In frequency-domain a similar relation can be applied:

$$RAO_{airgap} = RAO_{s_3} - RAO_{\zeta}. \quad (3.6)$$

The transfer function of the wave RAO_{ζ} is:

$$RAO_{\zeta} = \frac{\text{FFT}(\zeta(t))}{\text{FFT}(\zeta(t))} = 1. \quad (3.7)$$

Thus, the transfer function of the airgap is easily obtained from the transfer function of the heave motion:

$$RAO_{airgap} = RAO_{s_3} - 1. \quad (3.8)$$

Note, that the transfer function of the heave motion is an array of complex numbers, i. e. it contains amplitude and phase information. Therefore, the subtraction of 1 (complex $1, 0i$) introduces a phase shift and amplitude modification to the complex heave transfer function.

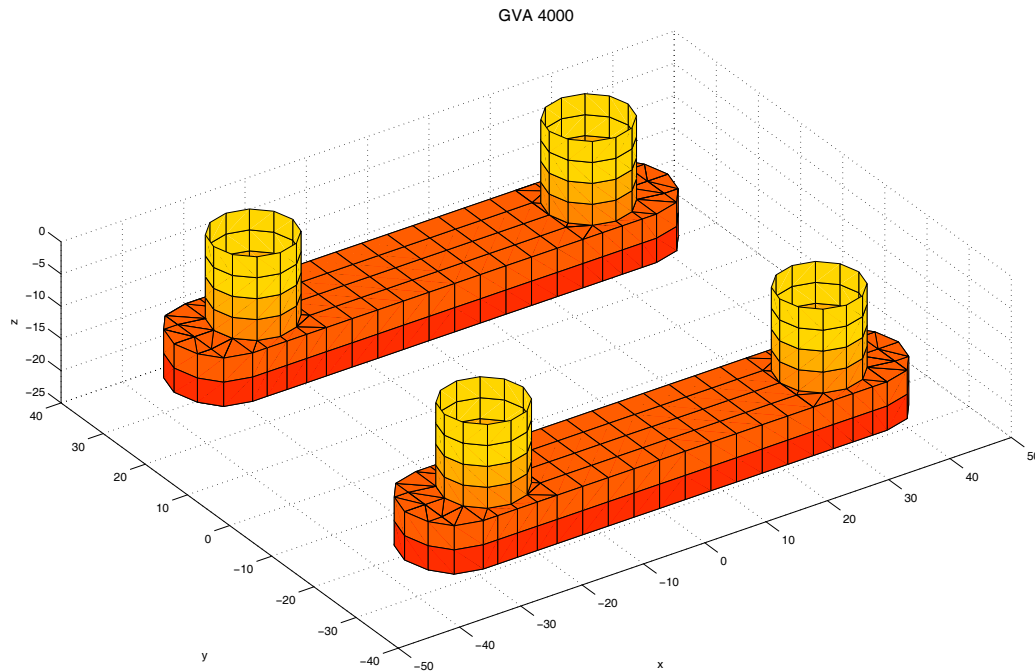


Figure 3.7: Discretization of semisubmersible *GVA 4000* at drilling draft for the analysis of seakeeping behavior and splitting forces using WAMIT.

3.3.2 SEAWAY

The program SEAWAY is a frequency-domain ship motion code, based on linear strip theory, to calculate the wave induced loads, motions, added resistance and internal loads for six degrees of freedom of displacement ships in regular and irregular waves (Journée (2000)). For calculating the vertical bending moments, the solid mass distribution is given to model the actual load case of the model. SEAWAY calculates the vertical bending moments from contributions of vertical forces as well as horizontal forces. SEAWAY is able to calculate the vertical bending moments with respect to an arbitrary vertical reference frame.

In analogy to WAMIT, results are given as transfer functions by amplitude and phase. Conventionally, the step from frequency-domain to time-domain is based on random distributed phases applied to the energy density spectrum as well as on the response spectrum, thus resulting in a random wave sequence and associated structure motions. To investigate the response characteristics in a deterministic wave sequence containing a Freak Wave, the phase information of the exciting wave train has to be conserved.

Therefore, responses in time-domain are calculated using the following procedure: First, the exciting wave scenario is transformed by Fourier transform into frequency-domain, giving the corresponding phases and amplitudes. Complex multiplication with the transfer function of the analyzed degree of freedom and backward transformation into time-domain by inverse Fourier transformation gives the questioned response. Thus, the responses of a structure due to deterministic wave sequences can be analyzed in time-domain, although the applied ship motion code gives results solemnly as transfer functions. This method is applied to investigate motions and structural responses in time-domain based both on WAMIT and SEAWAY.

3.3.3 IST TIME-DOMAIN CODE

In contrast to the two codes described so far, the IST-CODE (Instituto Superior Tecnico Lisbon) calculations are performed using a time-domain, nonlinear strip theory code (Fonseca and Guedes Soares (1998b)). The method assumes that the nonlinear contribution for the vertical bending moment is dominated by hydrostatic and Froude-Krilov forces, thus these components depend on the instantaneous wetted surface of the hull. Radiation and diffraction forces are considered to be linear. A detailed presentation of the method is given by Fonseca and Guedes Soares (1998a).

The hydrostatic forces and moments are calculated at each time step by integration of the hydrostatic pressure over the wetted surface of the hull under the undisturbed wave profile. The radiation forces, which are calculated using a strip theory method, are represented in the time-domain by infinite frequency added masses, radiation restoring coefficients (which are zero for the zero speed case), and convolution integrals of memory functions. The convolution integrals represent the effects of the entire history of the motion accounting for memory effects due to the radiated waves. This code has been validated against measurements with good results for the case of a container ship (Fonseca and Guedes Soares (2002)) and of an FPSO (Guedes Soares et al. (2001)).

Chapter 4

Bending Moments and Motions of Ship Type Offshore Structures due to Rogue Waves

Regarding structural loads, bending moments are probably the most critical ones apart from long term effects such as fatigue. In this chapter, the impact of Rogue Waves on the vertical bending moment of an FPSO and of a crane vessel, such as given in the previous chapter, are investigated. Results of both, numerical and experimental simulations are presented and compared. In addition, the motion behavior – in particular the heave and pitch motions – are analyzed with respect to Rogue Waves.

The investigations are performed in head waves, as most FPSO have a central mooring arrangement located within a turret. That allows them to weathervane, i. e. to rotate freely around the point of mooring in response to shifting weather directions. In extreme conditions also a crane vessel will weathervane. Therefore, the bow always points into the prevailing wind and current.

4.1 Results for the FPSO

In the following analysis, the question is raised, if standard frequency-domain evaluation methods for structural loads and motions cover also Rogue Wave impacts. The investigation also asks, if design rules – in particular for the vertical bending moments – are basically applicable for the design of FPSOs that are more and more asked for.

Results of both model tests and numerical simulations are presented. By comparison of time-domain results to results of frequency-domain investigations as well as to requirements of classification rules, the significance of Rogue Wave impacts is explored.

For the time-domain analysis of the responses of the FPSO, the following Rogue Wave scenarios are modelled:

- The *New Year Wave* as it was observed in the North Sea
- The *New Year Wave* at different positions further up- and downstream
- Variations of the *New Year Wave* with elongated period and increased maximum wave height
- Rogue Waves generated by the *experimental optimization* method as given in chapter 2
- Rogue Waves synthesized by the *linear optimization* approach.

4.1.1 Transfer functions of bending moments and motions of the FPSO

As a first step in the investigation of responses due to Rogue Waves, the RAOs for motions and bending moments are obtained from model tests and from calculations. An introduction to the three numerical programs applied can be found in section 3.3. Fig. 4.1 presents the transfer functions of the vertical bending moment at midship comparing numerical and experimental results. In WAMIT, the transfer function is calculated using the first five mode shapes which predicts accurately the frequency and amplitude of maximum response. SEAWAY and the IST-CODE slightly overestimate the peak values in comparison to model test data. Note, that for the calculations all three codes neglect viscous effects. The first peak ($\omega \approx 0.47$ rad/s) results from the wave length being equal to L_{pp} , i. e. the hogging and sagging cases. The cancellation frequency corresponds to a wave length of $L_{pp}/2$, and the second peak to $L_{pp}/3$. Therefore, the shape of the transfer function for the bending moment can be directly related to the geometry of the hull.

The IST-CODE as well as WAMIT assume the connecting elements for the registration of the bending moments to be at water line level. As SEAWAY is able to account for the vertical position of the measuring elements in the

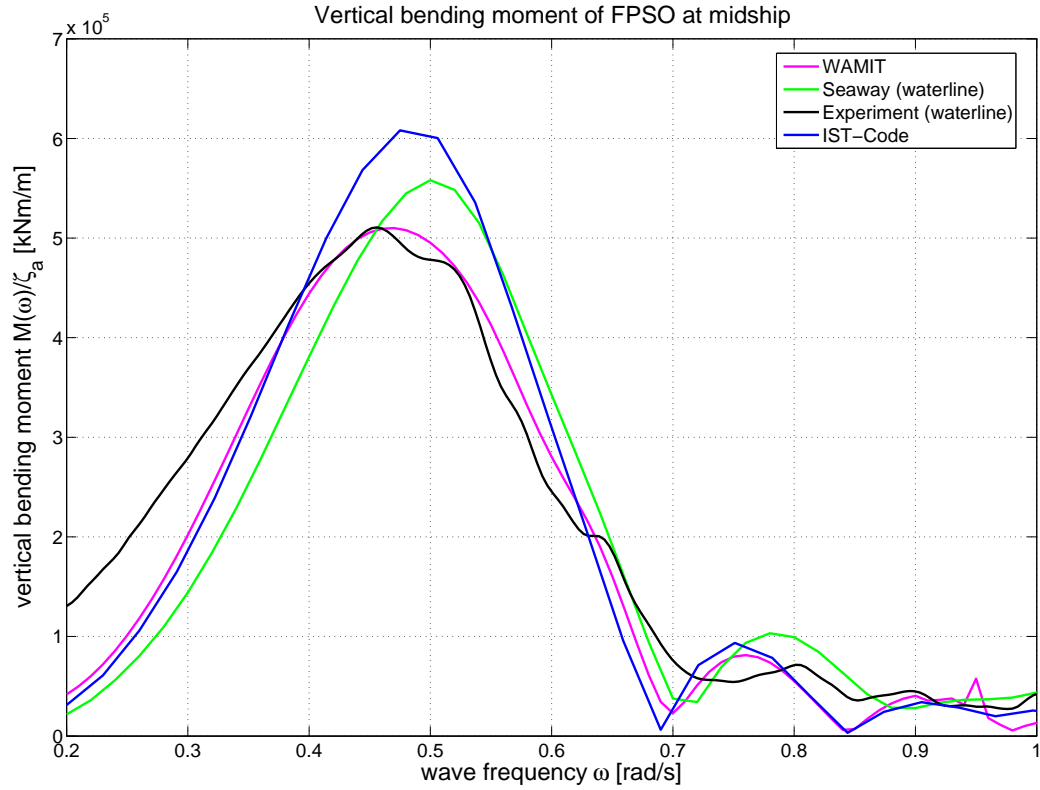


Figure 4.1: Transfer function of the vertical bending moments of the FPSO at midship position, measured and calculated at water line level. Maximum responses are observed if the wave length equals L_{pp} corresponding to hogging and sagging cases.

model, the sensitivity to this parameter is also analyzed. Fig. 4.2 gives a comparison of numerical and experimental data of the transfer functions of the vertical bending moments related to a reference frame at deck level. In comparison to the transfer functions of the bending moment calculated at water line level, the maximum values are significantly lower and the second peak at $\omega \approx 0.8$ rad/s becomes more dominant.

The transfer functions for the heave and pitch motion are presented in the next section, in Fig. 4.4 and Fig. 4.5, in the framework of the statistical estimation of extreme motions.

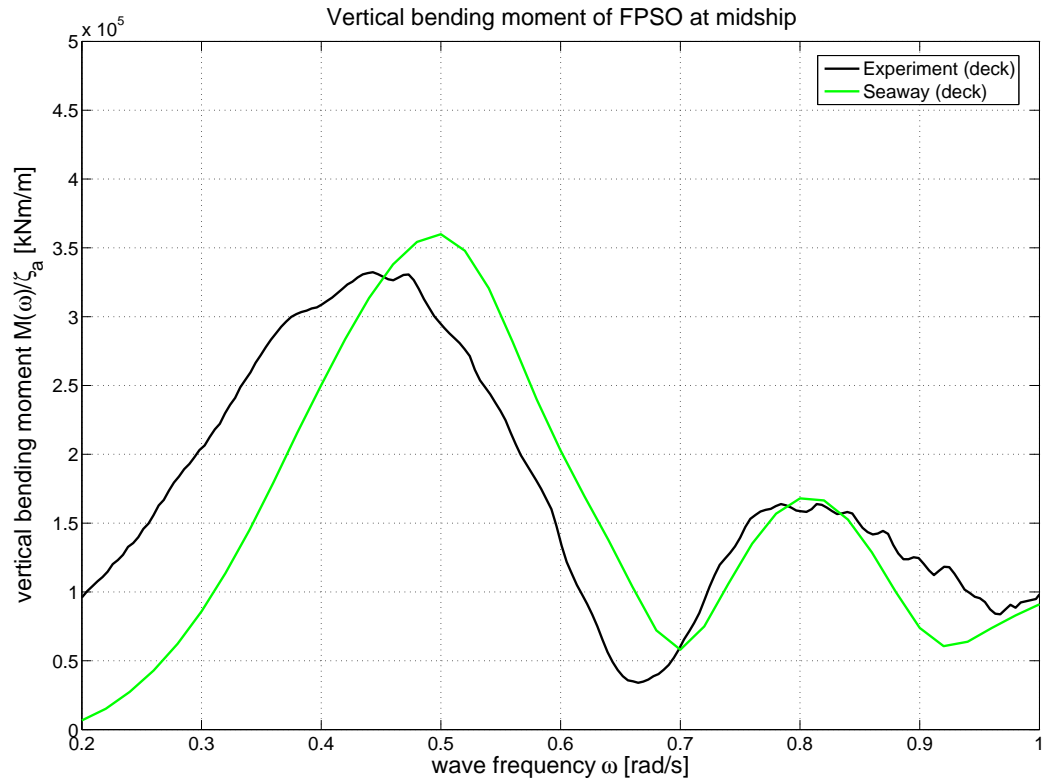


Figure 4.2: Transfer function of the vertical bending moment of the FPSO at midship position, measured and calculated at deck level. The amplitude of maximum response is clearly lower than in the case with connecting elements at water line level.

4.1.2 Frequency-domain approach and statistical analysis of loads and motions of the FPSO

For the design of offshore structures, the determination of significant responses depending on sea states is a commonly applied procedure. Fig. 4.3 illustrates this standard process, here for the investigation of the bending moments of the FPSO: Starting from an energy density spectrum (top diagram, Pierson-Moskowitz spectrum normalized for $H_s = 1$ m), the response spectra S_M are obtained by multiplication with the squared transfer function of the bending moment. For this example, the transfer function measured in model tests with wave packets is used. The associated significant bending moment (double amplitude) $2M_{sig}/H_s$ – as function of the zero-upcrossing period – is presented in the lowest diagram in Fig. 4.3. These data follow from the respective area of the response spectra for each zero-upcrossing period.

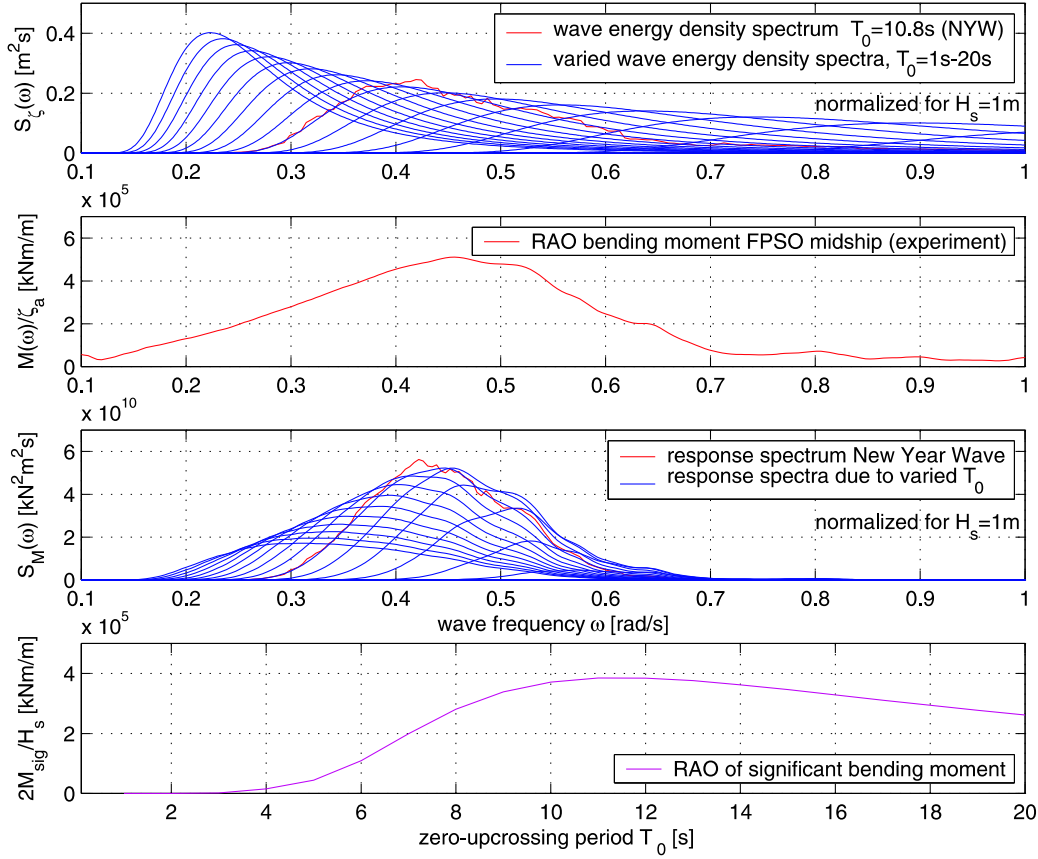


Figure 4.3: Frequency-domain analysis of the bending moments at midship section of the FPSO ship: Sea spectra – response amplitude operator – response spectra – significant bending moment double amplitude. Maximum bending moments are expected in sea states with $T_0 = 11$ s.

$$2M_{sig} = 4\sqrt{S_M}. \quad (4.1)$$

Highest values of the significant bending moment (double amplitude) are expected in the range of $T_0 = 11$ s. The significant bending moment to be expected in a given sea state is derived by multiplication of the (normalized) significant bending moment by the significant wave height. Maximum moments are estimated using the relation $M_{max} = 1.86 \cdot M_{sig}$ as explained in section 1.2 equation 1.1.

In analogy to the calculation of the significant bending moments, the heave motion and pitch motion of the FPSO are analyzed. Fig. 4.4 presents the investigation of the heave motion. For long waves, the FPSO follows the

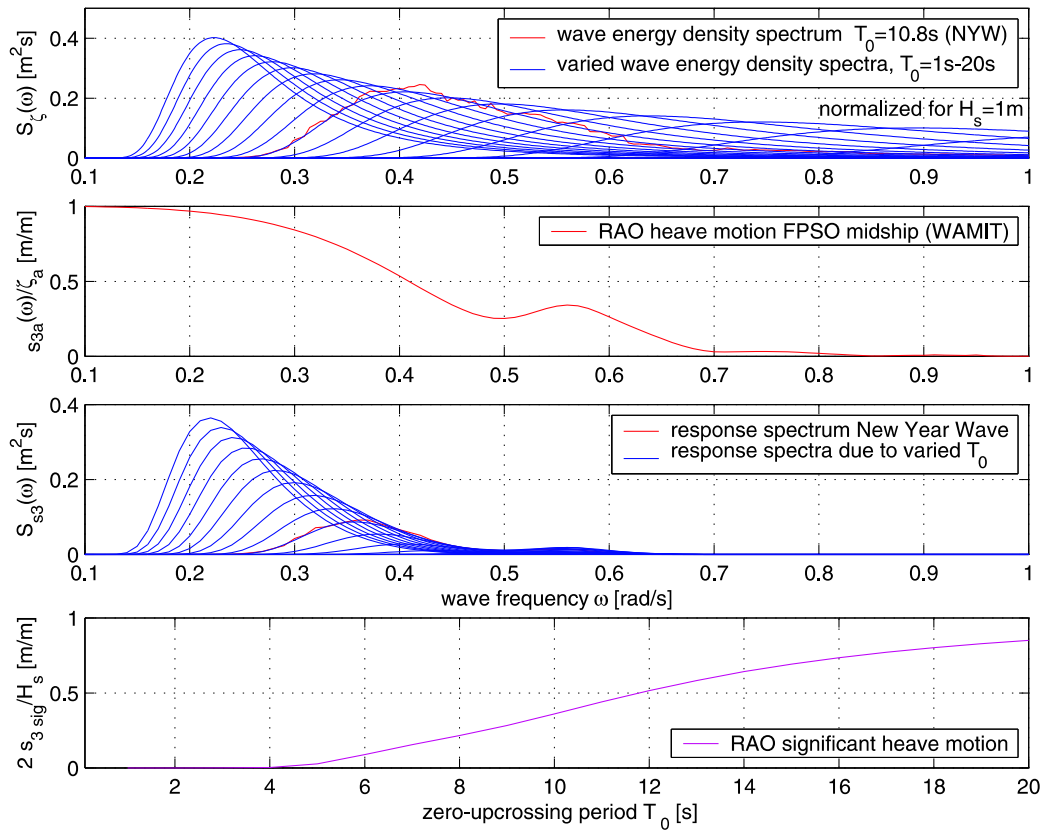


Figure 4.4: Frequency-domain analysis of the heave motion of the FPSO: Sea spectra – response amplitude operator – response spectra – significant heave motion double amplitude. Due to the large dimensions of the FPSO the heave motions are kept low for sea states with short periods.

wave motion and the transfer function equals one (Fig. 4.4 second diagram). Consequently, also the significant heave motion converges towards one for large wave lengths. Since the area under the sea spectra is normalized for $H_s = 1$ m and multiplied with the squared RAO of the heave motion, also the area of the response spectrum and consequently the significant heave motion equals 1 in long waves. With decreasing wave length the heave transfer functions becomes smaller, i. e. the FPSO will not follow the wave motions.

In Fig. 4.5 the statistical analysis of the pitch motion is presented. Maximum significant responses for the pitch motion (bottom diagram) are expected in identical sea states as for the bending moments. With these data from the statistical analysis maximum values of motions and bending moments are estimated and will be compared to time-domain observations.

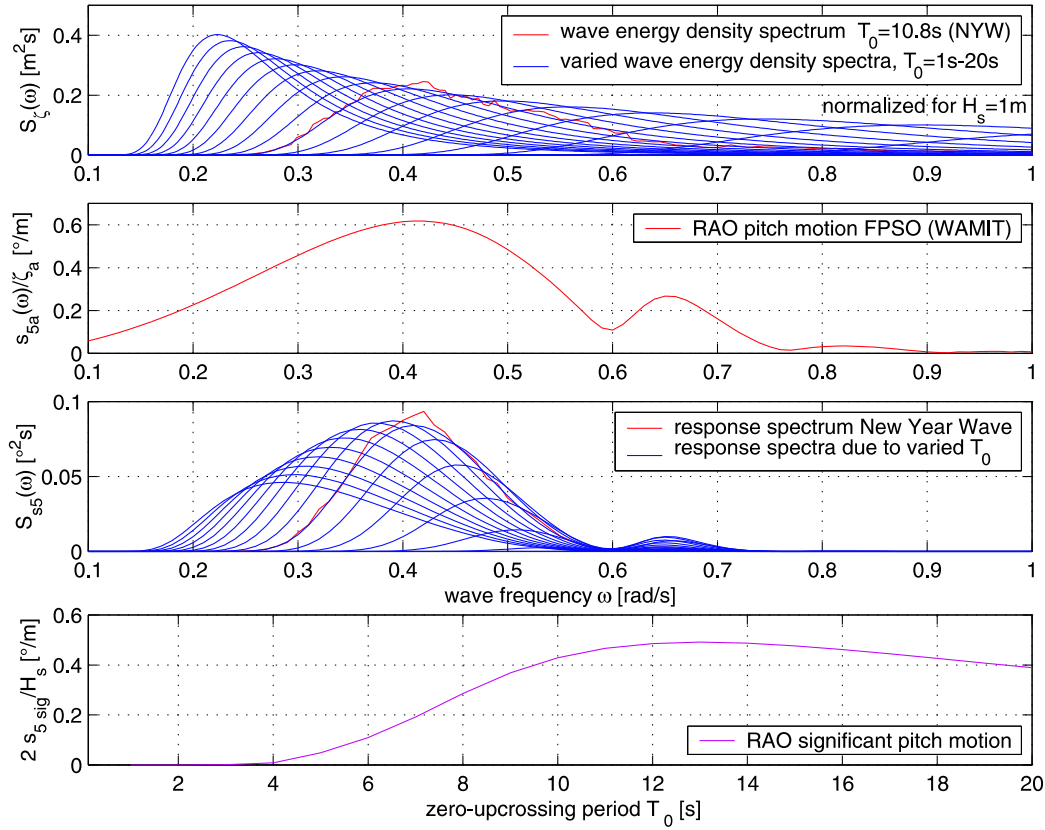


Figure 4.5: Frequency-domain analysis of the pitch motion of the FPSO: Sea spectra – response amplitude operator – response spectra – significant pitch double amplitude. The pitch transfer function shows a similar characteristic as the transfer functions of the bending moments. Thus the sagging and hogging case – wave length equals L_{pp} – gives also the largest pitch motions.

4.1.3 Comparison to classification rules

To ensure the safety of ships and lives at sea, rules from classification societies provide guidance to the designers and constructors concerning i. a. environmental conditions and subsequent loads. For a ship type structure, classification rules require the ship to withstand a minimum vertical bending moment that shall consider North Atlantic wave conditions. Since the rules are often based on experience, they are constantly adopted and improved. Nevertheless, one has to bear in mind, that rule values do not consider Rogue Waves explicitly, as ships can normally avoid severe weather by sailing on another route. Since the main classification societies are cooperating via the IACS (International Association of Classification Societies) requirements for

the wave bending moment are identical, regardless of the society.

For the FPSO selected for the investigation the maximum wave induced vertical bending moments as required by classification rules (Det Norske Veritas (2000)) is given for the sagging case by:

$$M_{sagging} = -0.11 \cdot c_W L_{pp}^2 B (c_B + 0.7), \quad (4.2)$$

and for the hogging case by:

$$M_{hogging} = 0.19 \cdot c_W L_{pp}^2 B c_B, \quad (4.3)$$

with c_W the wave coefficient that is determined by:

$$c_W = 10.75 - [(300 - L_{pp})/100]^{3/2} \quad (4.4)$$

for ship length L_{pp} between 100 m and 300 m, with the breath B and the block coefficient c_B .

This leads to values for the vertical bending moments of:

- $-5.64 \cdot 10^6$ kNm for sagging
- $5.41 \cdot 10^6$ kNm for hogging.

All new ships have to withstand at least these sagging and hogging moments and are built according to this requirements, if fatigue criteria do not call for a stronger structure.

4.1.4 Time-domain investigation of the FPSO encountering the *New Year Wave*

To investigate an example of a Rogue Wave impact in time-domain, the *New Year Wave* is realized in the wave tank and the associated responses of the FPSO are registered. In addition, calculations of time traces by all three numerical ship motion codes show the potential of numerical investigation tools. The results based on WAMIT and SEAWAY are calculated using the transfer functions obtained in the previous section, whereas the IST-CODE uses a time stepping method. In Fig. 4.6, the measured vertical bending moments and the associated heave and pitch motions resulting from the *New Year Wave* excitation are presented in comparison to the calculations.

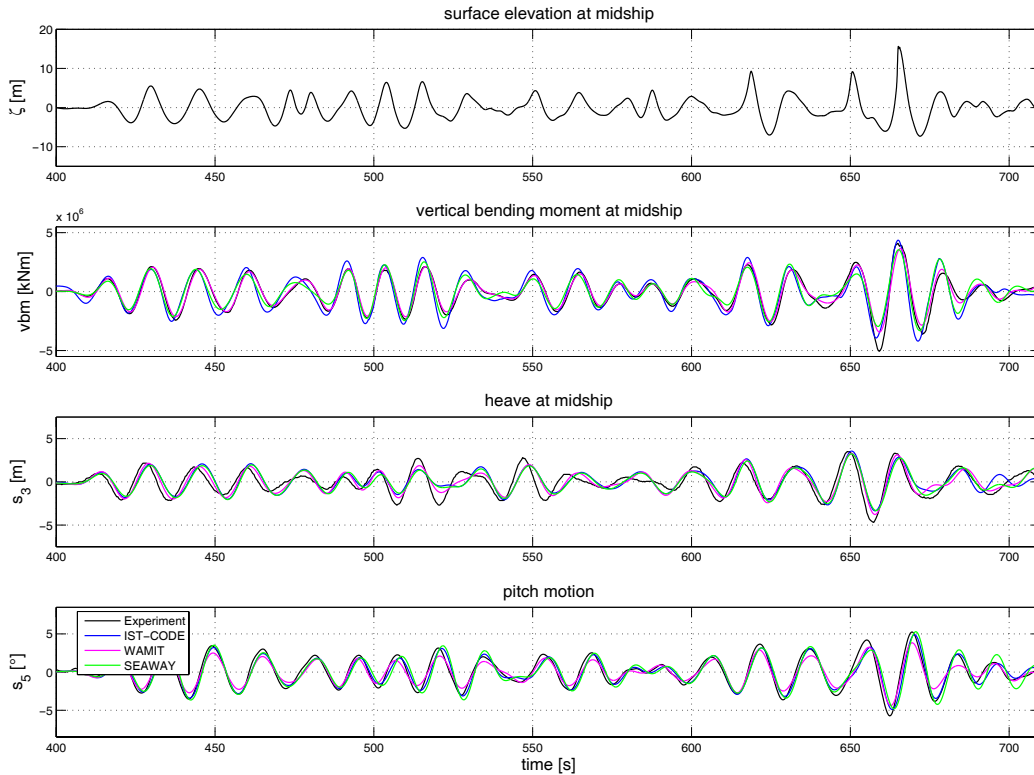


Figure 4.6: Comparison of experimental and numerical simulation of the FPSO facing the *New Year Wave*: Wave elevation – vertical bending moment at midship (at waterline level) – heave motion – pitch motion. The Rogue Wave impact results in responses larger than predicted by statistical means and classification rules.

The observed agreement between the results of numerical simulations and model tests is good. Even the responses due to the Rogue Wave event are modelled satisfactory by WAMIT and SEAWAY, although these are linear codes and therefore only valid for small wave elevations. Nevertheless, the maximum sagging moment is underestimated by all three codes by up to 30%. The same phenomenon can be observed for the heave and pitch motions, although differences are smaller (10% – 20%).

The observed asymmetric behavior of the structural responses confirms the nonlinearity of the vertical bending moments. These observations confirm results by Fonseca et al. (2001) who investigated the dynamic loads of a container ship in heavy weather at $F_n = 0$ and $F_n = 0.25$.

A comparison of the maximum sagging and hogging moments of the FPSO in this Rogue Wave ($-5.06 \cdot 10^6$ kNm and $4.08 \cdot 10^6$ kNm) to the wave bending

Responses of the FPSO due to the <i>New Year Wave</i>					
	$s_{exp,max}$	$s_{exp,min}$	s_{sig}	$s_{sig,max}$	$ s_{exp} _{max}/s_{sig,max}$
moment [10^6 kNm]	4.08	-5.06	2.29	4.26	1.19
heave [m]	3.51	-4.70	2.62	4.88	0.96
pitch [$^\circ$]	5.60	-5.87	2.78	5.18	1.13

Table 4.1: Bending moments, heave and pitch motion of the FPSO due to the *New Year Wave* comparing statistical values and results from model tests: Measured maximum and minimum responses $s_{exp,max}$ and $s_{exp,min}$, significant amplitudes s_{sig} , maximum significant amplitudes $s_{sig,max}$, and ratio of maximum measured response to maximum significant response $|s_{exp}|_{max}/s_{sig,max}$.

moment limitations according to classification rules for ships ($-5.64 \cdot 10^6$ kNm and $5.41 \cdot 10^6$ kNm) reveals that the existing rules are covering this extreme wave impact of the *New Year Wave*.

Table. 4.1 presents the results of the frequency-domain estimation of the maximum responses in comparison to results from model tests. The experiment gives 19% larger responses for the bending moment and 13% larger pitch motions. Thus, the *New Year Wave* is a critical wave sequence, although the *Draupner* sea state ($H_s = 11.92$ m, $T_0 = 10.8$ s) itself is not that extreme.

Since the *New Year Wave* appears to be an extraordinary wave, the responses of the FPSO due to this wave sequence are analyzed in more detail. The encountering position of the FPSO is varied systematically and the geometry of the Rogue Wave itself is modified with respect to period and wave height.

4.1.5 Variation of the location of encounter between the *New Year Wave* and the FPSO

Based on the investigation of the responses of the FPSO due to the *New Year Wave* as it was recorded in the field (Fig. 4.6), the position of the FPSO is adjusted in the wave tank in order to answer the question, if the *New Year Wave* sequence is most critical at the position it was measured, or would be more severe – with respect to structural responses and motions – further up- or downstream. Nine different positions of the FPSO ($-3/2L_{pp}$, $-1L_{pp}$, $-1/2L_{pp}$, $-1/4L_{pp}$, initial position, $+1/4L_{pp}$, $+1/2L_{pp}$, $+1L_{pp}$, $+3/2L_{pp}$) are selected and the *New Year Wave* is generated. The associated wave elevation registered at midship and the corresponding vertical bending moments measured at midship are presented in Fig. 4.7.

Surprisingly, the reference Freak Wave measured at the *Draupner* platform seems to be less severe compared to upstream locations. One quarter of the ship length upstream ($-1/4L_{pp}$), the wave turns out to be higher due to a deep trough (Clauss et al. (2004c)). As a consequence, the maximum vertical sagging moment is clearly increased (+10% = $5.61 \cdot 10^6$ kNm). This is just within the limiting maximum sagging moment from classification rules for ships ($5.64 \cdot 10^6$ kNm) confirming that the selected *New Year Wave* is really an extreme event. Maximum hogging moments are observed a quarter of a ship length downstream ($+1/4L_{pp}$ in wave direction) and are well within limitations of classification rules.

The maximum responses within $-3/2L_{pp}$ to $+3/2L_{pp}$ vary in the range of 34% for sagging, 24% for hogging, and 32% in wave height, although the wave train is generated by the same control signal. This variation of the location of encounter reveals clearly the importance of phase information and the knowledge of the local wave characteristics, since responses due to the same wave sequence can dramatically change within a few ship length.

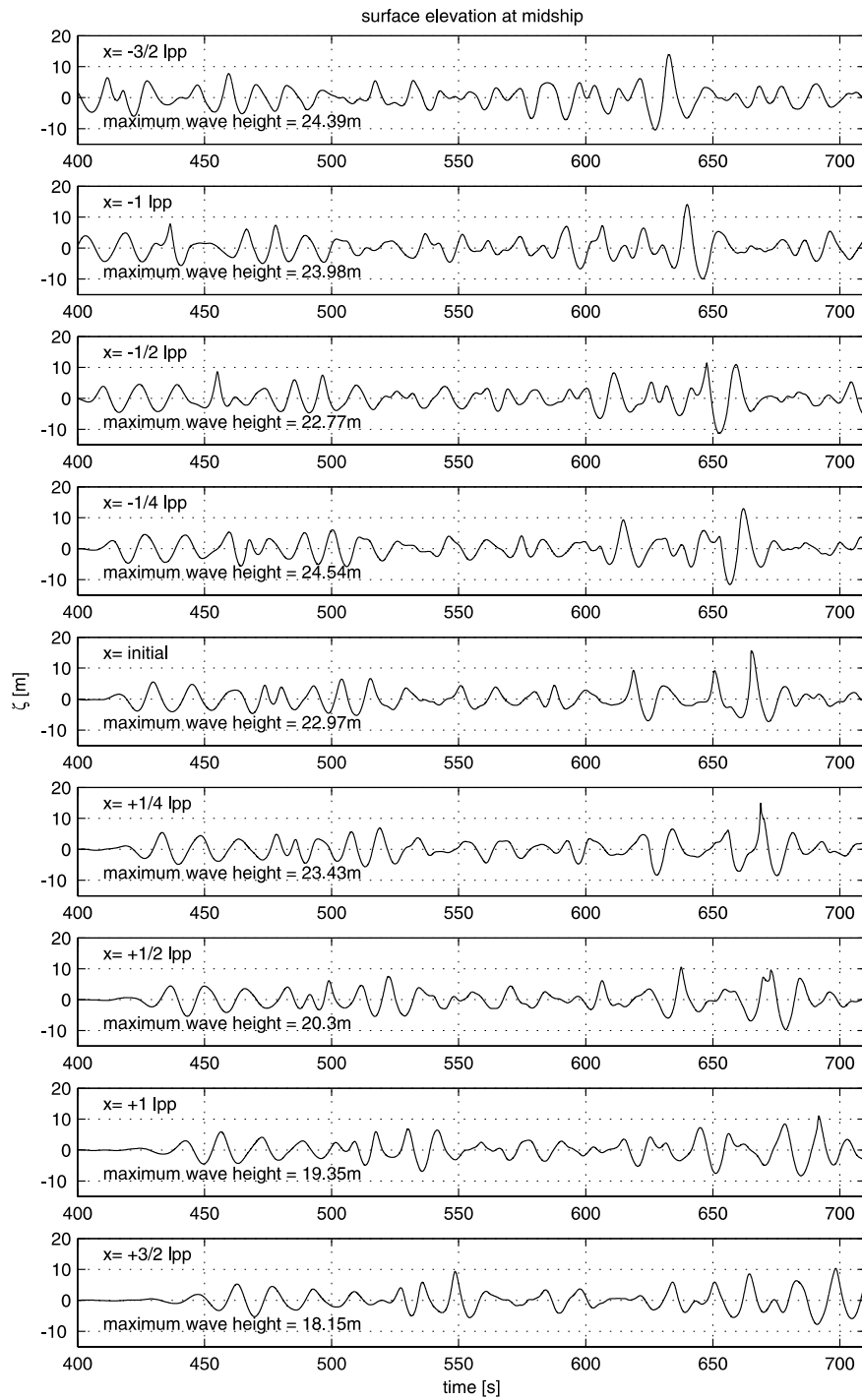
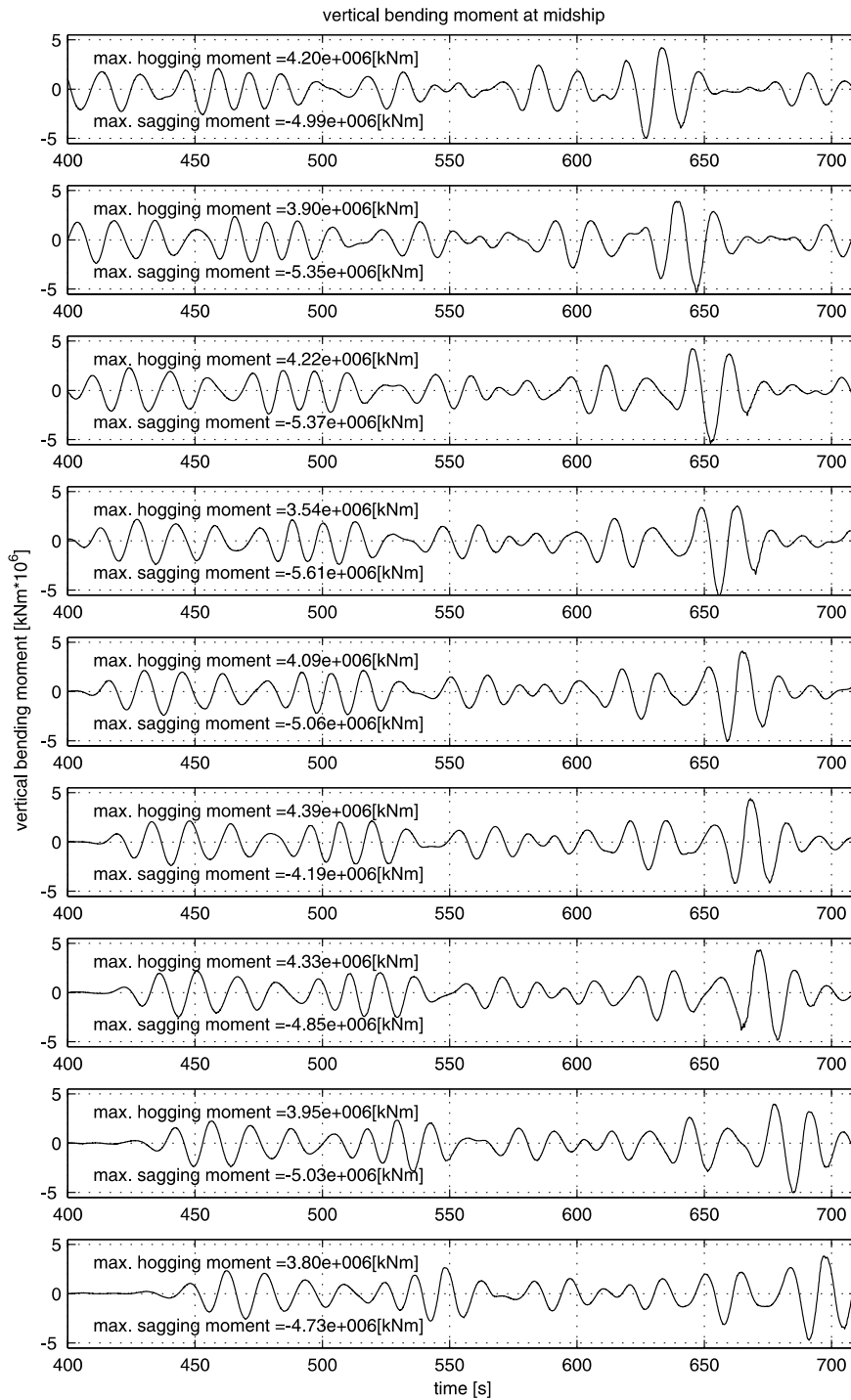


Figure 4.7: *New Year Wave* measured at different positions in the wave tank (left) and associated vertical bending moments of the FPSO due to the Rogue Wave impact (right). Maximum bending moments are observed $-1/4L_{pp}$



upstream for sagging and $+1/4L_{pp}$ downstream for hogging, revealing that the *New Year Wave* is more severe at these positions than at the original one.

4.1.6 Variation of period and height of the *New Year Wave* sequence

Variation of the position of encounter, between the FPSO and the incoming wave sequence, revealed that structural responses are extremely sensitive to the local shape of the Rogue Wave. Therefore, using the new nonlinear wave generation approach proposed by Hennig (2005), modifications are introduced into the *New Year Wave* sequence and two different scenarios are realized:

- *New Year Wave* with elongated local period
- *New Year Wave* with increased wave height and elongated period.

Fig. 4.8 (top) gives an impression of the original *New Year Wave* modelled in the wave basin (black line) and the two variations. The wave history is kept unchanged up to the instance when the *New Year Wave* occurs, thus ensuring comparability of the responses as memory effects caused by excitations of the preceding waves are identical for all three conditions. In the case with elongated local period (blue lines) of the *New Year Wave*, in addition an increase in wave height can be observed, although this was not explicitly modelled. This is due to the fact that wave breaking is reduced in comparison to the original *New Year Wave*, as the wave steepness is reduced with longer period and consequently the wave becomes taller.

From Fig. 4.8 it can be seen, that the largest wave (red line) gives also the largest structural responses and motions. Table 4.2 summarizes the registered maximum wave heights, bending moments at midship and at quarter length, and differences compared to the original wave train in percent. Table 4.3 gives the maximum heave and pitch motions of the FPSO due to the three *New Year Wave* sequences.

As could have been expected, the largest responses follow from the highest wave. Nevertheless, the results show, that the increase in response is not proportional to the increase in wave height, i. e. a nonlinear system behavior is observed. Surprisingly, in case (2) the maximum sagging moment remains unchanged, whereas the wave height is increased by 19%. In contrast, wave sequence (3) results in an increase of the heave motion by 71%, although the maximum wave height is only 29% larger. These results clearly point out, that the local wave pattern is extremely important for the maximum responses and therefore deterministic methods for the evaluation of seakeeping behavior are required.

Bending moments of the FPSO ship					
	midship		quarter length		
	hogging [10 ⁶ kNm]	sagging [10 ⁶ kNm]	hogging [10 ⁶ kNm]	sagging [10 ⁶ kNm]	H_{max} [m]
(1)	3.98	-4.41	2.52	-2.62	20.66
(2)	4.65 +17%	-4.37 -1%	2.64 +5%	-2.47 -6%	24.63 +19%
(3)	5.51 +38%	-5.68 +29%	3.30 +31%	-3.41 +30%	26.67 +29%

(1) = *New Year Wave*

(2) = *New Year Wave* with elongated period

(3) = *New Year Wave* with increased wave height and elongated period

Table 4.2: Bending moments of the FPSO ship due to the modified *New Year Wave* sequences. The increase or even decrease of the bending moments due to a larger wave height, emphasis clearly the need for knowing the local wave characteristics and for time-domain investigations of Rogue Wave impacts.

Heave and pitch motion of the FPSO ship					
	heave		pitch		H_{max}
	[m]	[m]	[°]	[°]	[m]
(1)	3.95	-3.95	4.88	-5.09	20.66
(2)	5.68 +44%	-4.71 +19%	6.20 +27%	-5.90 +16%	24.63 +19%
(3)	6.76 +71%	-5.89 +49%	7.00 +43%	-7.04 +38%	26.67 +29%

(1) = *New Year Wave*

(2) = *New Year Wave* with elongated period

(3) = *New Year Wave* with increased wave height and elongated period

Table 4.3: Heave and pitch motions of the FPSO due to the modified *New Year Wave* sequences. Encountering wave sequence (3), responses of the FPSO are amplified more than proportional – indicated with bold font. As an extreme case, the heave motion is increased by 71%, although the exciting wave is only 29% larger, showing the nonlinear system behavior.

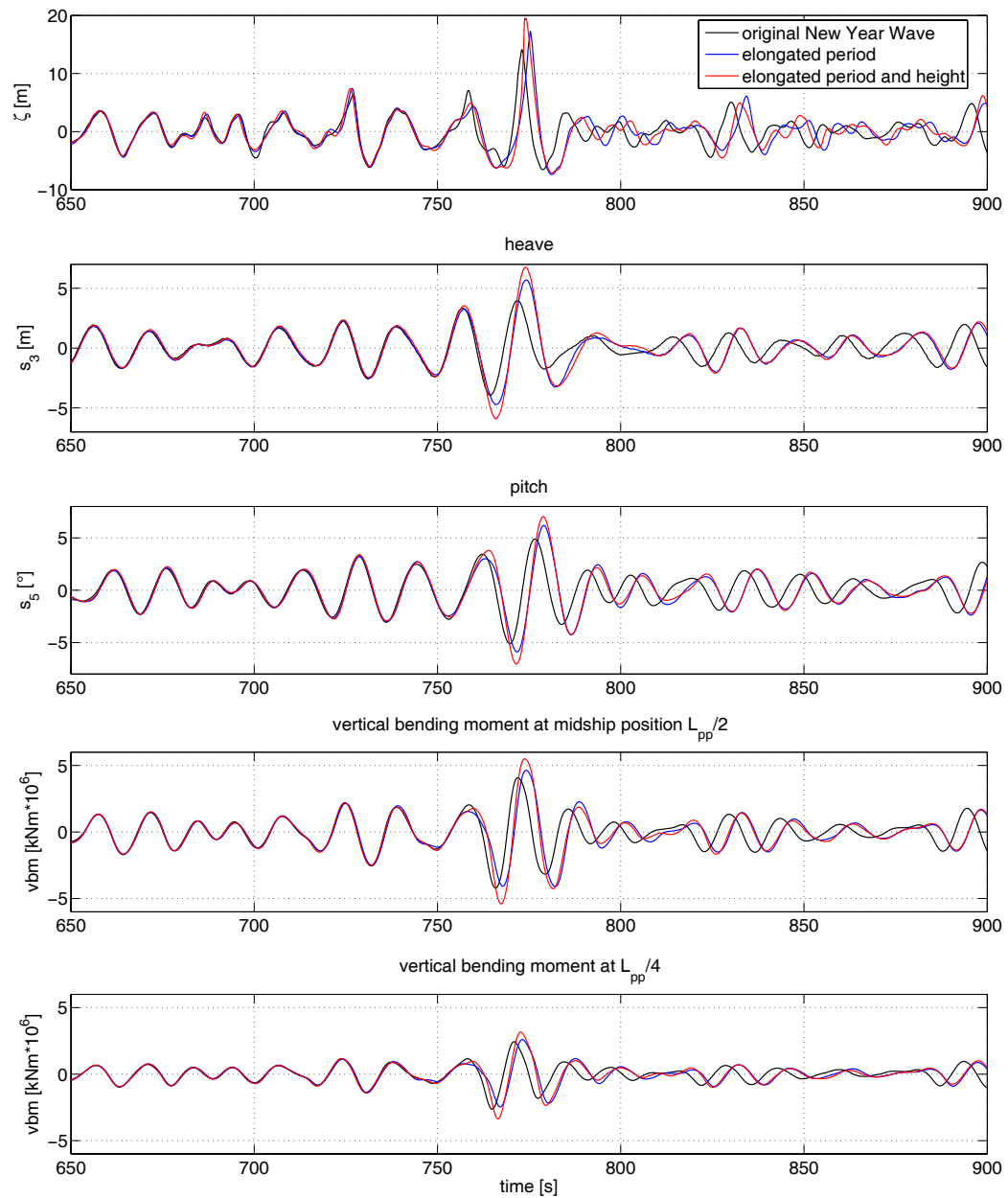


Figure 4.8: *New Year Wave* (black), *New Year Wave* with elongated period (blue), and *New Year Wave* with elongated period and increased wave height (red) as well as resultant heave and pitch motion and vertical bending moments at midship and at quarter length from bow. The wave history is kept unchanged, thus enabling the relation of changes in response to the modifications introduced into the *New Year Wave*.

4.1.7 FPSO in Rogue Waves integrated in storm seas

As the *New Year Wave* and their variations may by chance be exotic Rogue Waves, in this section different storm seas with embedded Rogue Waves are generated using either the *experimental optimization* or the *linear optimization* approach presented in chapter 2. Again, the resultant motions and loads due to these Rogue Wave impacts are investigated.

In the first case study, the *experimental optimization* approach is applied to integrate a single high wave with $H_{max}/H_s = 2$ in a random JONSWAP sea state with a significant wave height of $H_s = 13$ m, peak enhancement factor $\gamma = 1$ and peak period $T_p = 13$ s. This wave originates from the *experimental optimization* in the small wave tank and is then transferred to the large wave tank in order to enable model tests at a scale of 1:81 (see chapter 2 and compare Figs. 2.10 and 2.11).

Responses of the FPSO due to the experimentally optimized Rogue Wave					
	$s_{exp,max}$	$s_{exp,min}$	s_{sig}	$s_{sig,max}$	$ s_{exp} _{max}/s_{sig,max}$
moment [10^6 kNm]	5.89	-7.50	2.20	4.09	1.83
heave [m]	4.47	-4.62	1.85	3.43	1.35
pitch [$^\circ$]	6.35	-5.66	2.40	4.46	1.42

Table 4.4: Bending moments, heave and pitch motions of the FPSO due to the wave sequence generated by the *experimental optimization* process, comparing statistical and experimental data: Measured maximum and minimum responses $s_{exp,max}$ and $s_{exp,min}$, significant pitch amplitudes s_{sig} , maximum significant amplitudes $s_{sig,max}$, and ratio of maximum measured response to maximum significant response $|s_{exp}|_{max}/s_{sig,max}$.

In Fig. 4.9, the measured wave train (top) and the subsequent bending moments, heave and pitch motions are shown. For comparison, calculations using the seakeeping codes WAMIT and SEAWAY are also given. The maximum responses observed in model tests are summarized in Table 4.4 and compared to the maximum significant amplitudes originating from the statistical analysis. In addition, the last column in Table 4.4 gives the ratio of maximum measured response to maximum significant response. Appallingly, all registered maximum responses clearly outreach the estimated maximum values from the statistics (+35% to +83%), although a significant wave height of $H_s = 13$ m and a maximum wave height of 26 m is not the worst that can be expected during the lifespan of an FPSO. The observed maximum bending moments clearly outreaches the limitations from classification rules for ships

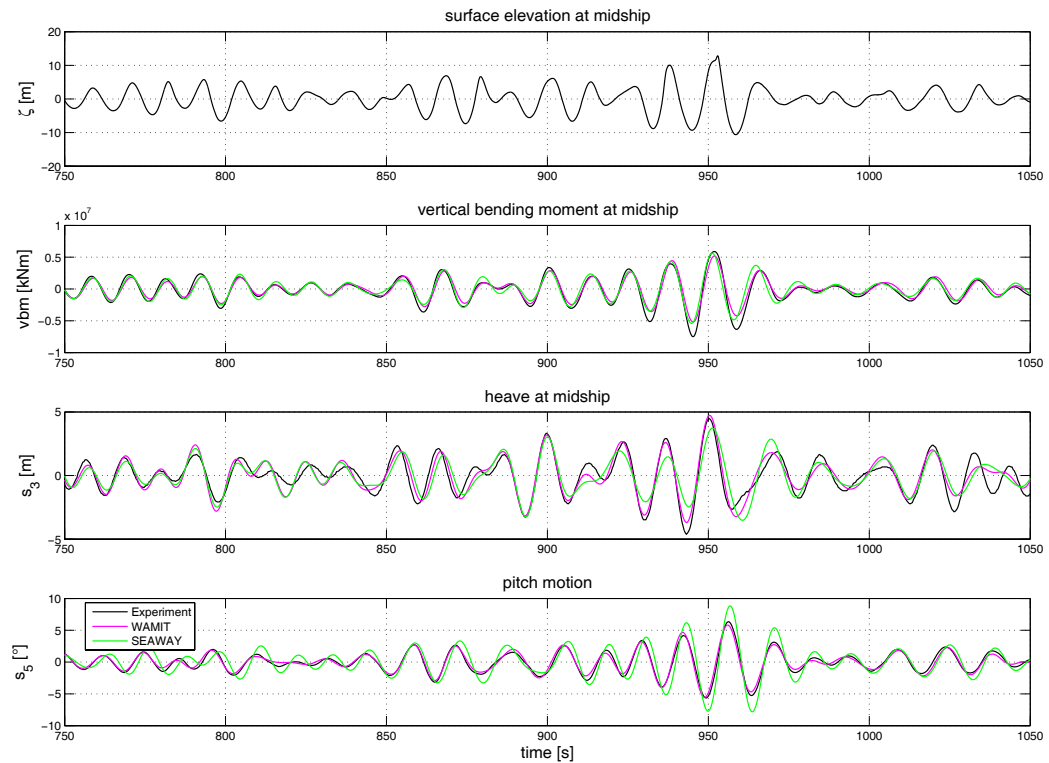


Figure 4.9: FPSO in storm sea with embedded Rogue Wave generated by the *experimental optimization* process presented in chapter 2, $H_{max}/H_s = 2$, $H_s = 13$ m, $T_p = 13$ s, $\gamma = 1$. Although the ratio of $H_{max}/H_s = 2$ is frequently observed during a storm, responses are significantly larger than estimated by statistics.

($-5.64 \cdot 10^6$ kNm and $5.41 \cdot 10^6$ kNm). These results emphasize the potential of the new *experimental optimization* process, since deterministic wave scenarios can be designed and synthesized based on predefined parameters and realized precisely in the model basin.

To back up the findings from the investigation of the *New Year Wave* sequence and the wave sequence generated by the *experimental optimization* approach, four additional Rogue Wave scenarios are synthesized by the *linear optimization* process introduced in chapter 2. The advantage of this method is, that control signals can be generated fast, without time consuming *experimental optimization*. As the procedure is based on linear wave theory, nonlinear wave effect are not considered for, and deviations between target wave train and measured wave train may occur. In particular, the target location and the local parameters of the embedded Rogue Wave may deviate.

Therefore, during the experiments, the target location, i. e. the position of the FPSO model in the wave tank, is adjusted accordingly.

Significant wave heights of 12 m and 13 m are selected with peak periods of 14 s and 15 s. These are harsh sea conditions, but by no means the most extreme conditions an FPSO will encounter during the lifetime, as was already discussed in chapter 1. In consequence, an FPSO ship must be able to bear such conditions. Into the four sea states, Rogue Waves with H_{max}/H_s ratios of around 2.5 are integrated and Table 4.5 gives the associated main parameters of the synthesized storm scenarios. For simplicity, the four storm wave sequences are labelled with letters A to D. The maximum wave height generated is 32.56 m in wave scenario B, and the maximum ratio of H_{max}/H_s is 2.68 in wave scenario D.

Synthesized harsh wave conditions				
	T_p [s]	H_s [m]	H_{max} [m]	H_{max}/H_s -
(A)	15	13	31.85	2.45
(B)	15	13	32.56	2.50
(C)	14	12	28.83	2.40
(D)	14	12	32.15	2.68

Table 4.5: Characteristics of the four storm sea states with integrated Rogue Waves generated by the *linear optimization* approach: Peak period T_p , significant wave height H_s , maximum wave height H_{max} and the ratio of maximum to significant wave height H_{max}/H_s .

As result from the model tests, Figs. 4.10 to 4.13 show the Rogue Wave sequences, the corresponding vertical bending moments at midship and the heave and pitch motions for each of the four wave scenarios. For comparison, calculations results by SEAWAY and by WAMIT are also given. In general, the calculated bending moments agree well with experimental data. Nevertheless, the maximum bending moments are underestimated in all four sea states by the numerical codes. In contrast to this observation, the heave motions are generally well predicted, also at the instance of encountering the Rogue Wave. The pitch motion is predicted accurately by WAMIT, whereas SEAWAY overestimates the pitch angles. The consequences of overestimating loads and motions are structures designed for more extreme conditions, thus structures are safer and probably more expensive to build. In contrast, a underestimation of responses may lead to designs not sufficiently armed to cope with extreme conditions.

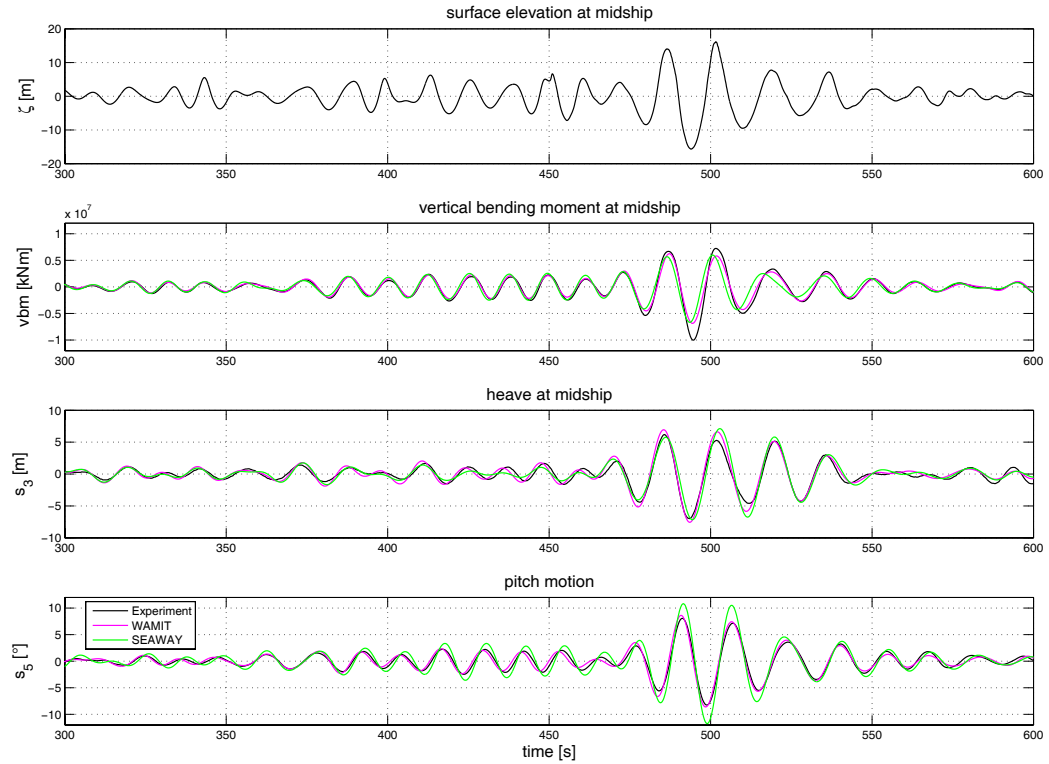


Figure 4.10: Responses of the FPSO due to storm scenario A: $T_p = 15$ s, $H_s = 13$ m, $H_{max} = 31.85$ m and $H_{max}/H_s = 2.45$. Although this wave sequence has the second smallest ratio of H_{max}/H_s of the four wave sequences synthesized by the *linear optimization* process, the bending moments as well as the pitch motions are the largest observed in the model tests.

In Table 4.6 the maximum hogging and sagging moments in comparison to significant (maximum) values of the frequency-domain approach are summarized. Note, that the last column of Table 4.6 gives the ratio of maximum observed sagging moment to the maximum significant bending moment. The observed maximum sagging moments are for all four wave scenarios larger than the maximum hogging moment, i. e. wave troughs impose larger bending moments on the FPSO. From the data it is obvious that the frequency-domain approach, applying the relation $M_{sig,max} = 1.86 \cdot M_{sig}$ to estimate the maximum responses, does not cover these extreme wave impacts. In wave scenarios A and C, measured values are more than twice as large than estimated by statistics. Surprisingly, out of the four wave scenarios investigated, these both cases have the lowest H_{max}/H_s ratios and seem nonetheless to be the worst for the structural responses.

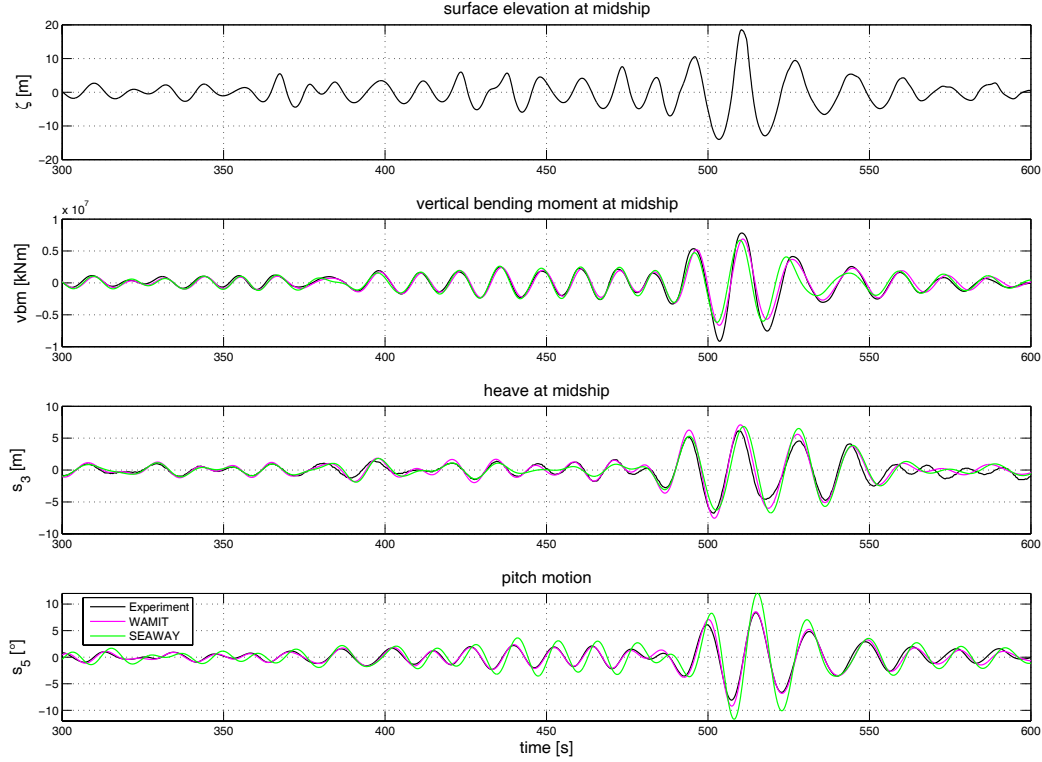


Figure 4.11: Responses of the FPSO due to storm scenario B: $T_p = 15$ s, $H_s = 13$ m, $H_{max} = 32.56$ m and $H_{max}/H_s = 2.50$. Both numerical methods have difficulties to model the consequences of the Rogue Wave impact, i. e. to model the maximum responses precisely.

In comparison to the requirements of classification rules for ships with regard to the minimum bending moments a ship has to withstand undamaged, $-5.64 \cdot 10^6$ kNm for sagging and $5.41 \cdot 10^6$ kNm for hogging, the experimental values are significantly larger, although classification rules estimate already larger maximum moments than the statistical approach.

In Table 4.7 the maximum heave responses are listed and compared to statistical values. Differences observed are less than found for the bending moments. Nevertheless, also the observed heave motions are up to 48% larger in wave scenario C. Therefore, wave sequence C seems to be a really critical one, although the embedded Freak Wave and its H_{max}/H_s ratio are smallest.

Table 4.8 summarizes the maximum pitch motions in analogy to the previous tables of the bending moments and heave motions. In general, also the pitch motions are significantly underestimated by the statistical approach. In consequence, if the statistical approach is applied to estimate maximum

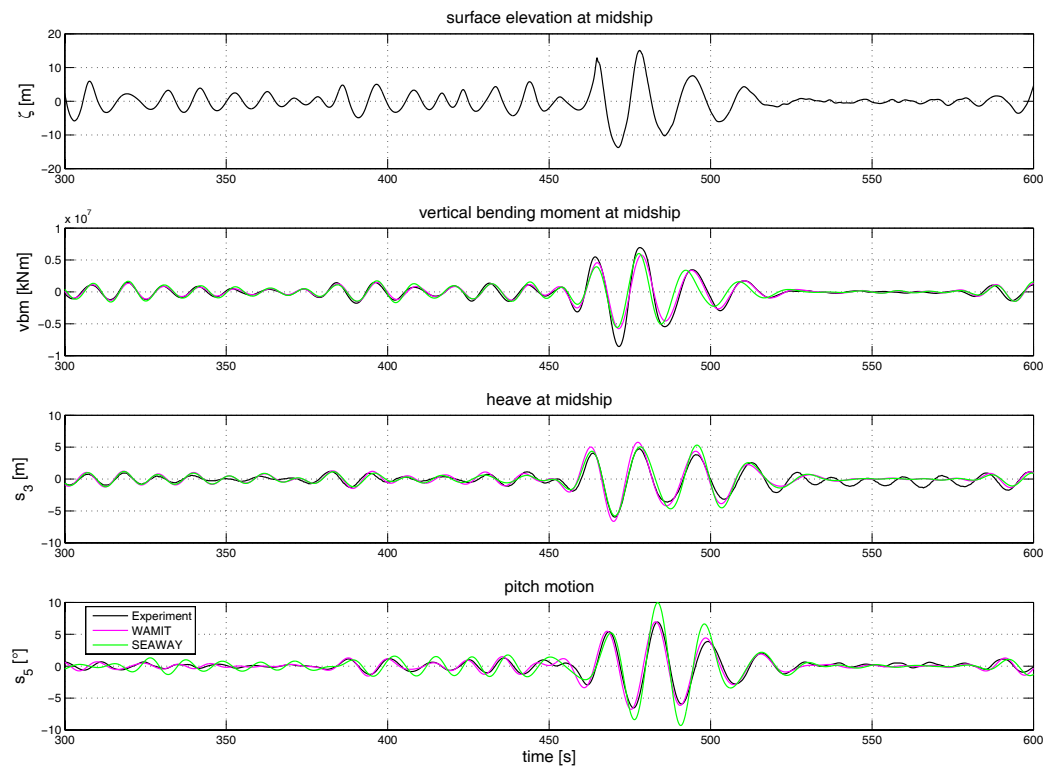


Figure 4.12: Responses of the FPSO due to storm scenario C: $T_p = 14$ s, $H_s = 12$ m, $H_{max} = 28.83$ m and $H_{max}/H_s = 2.40$. Surprisingly, the wave sequence with the smallest ratio of H_{max}/H_s gives heave motions 48% larger than estimated by frequency-domain analysis.

response using a ratio of 1.86 between significant and maximum response, one cannot be sure to be on the safe side if Rogue Wave impacts should be considered.

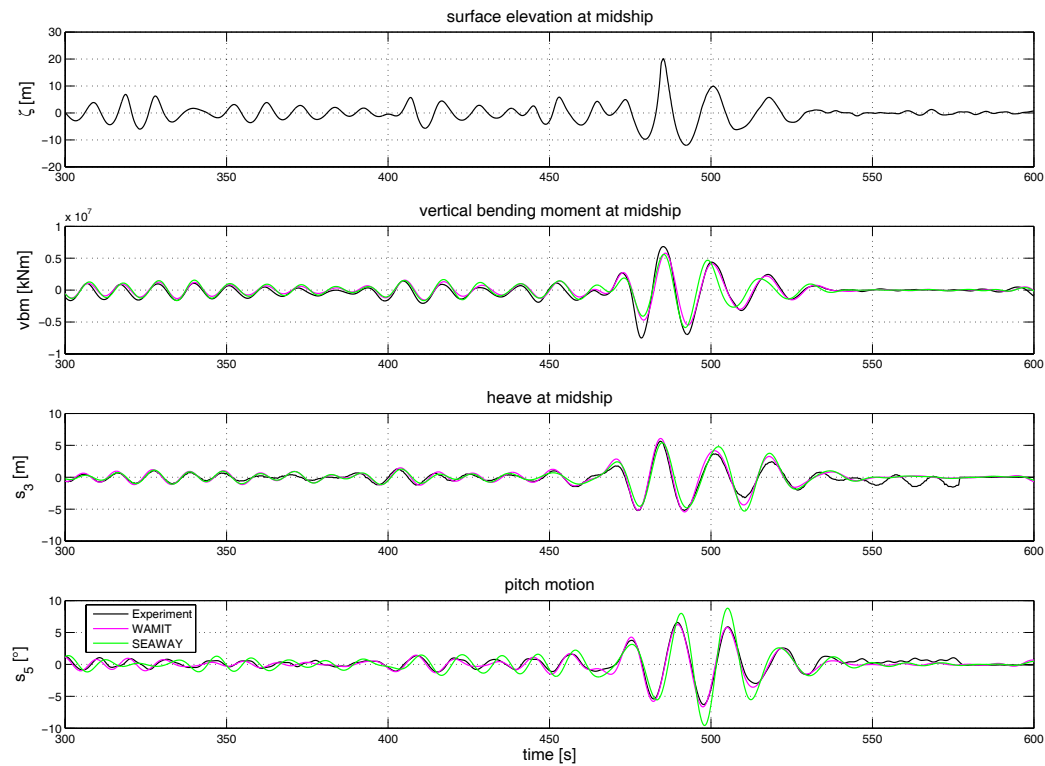


Figure 4.13: Responses of the FPSO due to storm scenario D: $T_p = 14$ s, $H_s = 12$ m, $H_{max} = 32.15$ m and $H_{max}/H_s = 2.68$. Unexpectedly, the worst wave scenario with a ratio of $H_{max}/H_s = 2.68$ gives not the worst responses.

Bending moments of the FPSO						
Sea state		Experiment		Statistics		
	H_{max}/H_s	$M_{hogg,max}$	$M_{sagg,max}$	M_{sig}	$M_{sig,max}$	$ M_{exp} _{max}/M_{sig,max}$
	[-]	[10 ⁶ kNm]	[10 ⁶ kNm]	[10 ⁶ kNm]	[10 ⁶ kNm]	[-]
(A)	2.45	7.23	-10.03	2.50	4.64	2.16
(B)	2.50	7.82	-9.16	2.50	4.64	1.97
(C)	2.40	6.94	-8.57	2.23	4.14	2.07
(D)	2.68	6.83	-7.51	2.23	4.14	1.81

Table 4.6: Vertical bending moments of the FPSO due to storm seas: Sea state parameters, maximum measured hogging moment $M_{hogg,max}$, maximum measured sagging moment $M_{sagg,max}$, significant bending moment amplitude M_{sig} , maximum significant bending moment $M_{sig,max} = 1.86 \cdot M_{sig}$ and ratio of maximum measured moment to maximum significant bending moment $|M_{exp}|_{max}/M_{sig,max}$.

Heave motions of the FPSO							
Sea state		Experiment		Statistics			
	H_{max}/H_s	H_{max}	$s_{3,exp,max}$	$s_{3,exp,min}$	$s_{3,sig}$	$s_{3,sig,max}$	$ s_{3,exp} _{max}/s_{3,sig,max}$
	[-]	[m]	[m]	[m]	[m]	[m]	[-]
(A)	2.45	31.85	6.21	-6.99	2.86	5.32	1.31
(B)	2.50	32.65	6.16	-6.77	2.86	5.32	1.27
(C)	2.40	28.83	4.76	-5.95	2.17	4.03	1.48
(D)	2.68	32.15	5.66	-5.22	2.17	4.03	1.30

Table 4.7: Heave motions of the FPSO due to storm seas: Sea state parameters, maximum and minimum measured heave motion $s_{3,exp,max}$ (up) and $s_{3,exp,min}$ (down), significant heave motion $s_{3,sig}$, maximum significant heave motion $s_{3,sig,max} = 1.86 \cdot s_{3,sig}$ and ratio of maximum measured heave motion to maximum heave motion amplitude $|s_{3,exp}|_{max}/s_{3,sig,max}$.

Pitch motions of the FPSO							
Sea state			Experiment		Statistics		
	H_{max}/H_s	H_{max}	$s_{5,exp,max}$	$s_{5,exp,min}$	$s_{5,sig}$	$s_{5,sig,max}$	$ s_{5,exp} _{max}/s_{5,sig,max}$
	[-]	[m]	[°]	[°]	[°]	[°]	[-]
(A)	2.45	31.85	8.05	-8.24	3.04	5.65	1.46
(B)	2.50	32.65	6.29	-6.57	3.04	5.65	1.16
(C)	2.40	28.83	6.93	-6.54	2.57	4.79	1.37
(D)	2.68	32.15	6.57	-6.29	2.57	4.79	1.31

Table 4.8: Pitch motions of the FPSO due to storm seas: Sea state parameters, maximum and minimum measured pitch motion $s_{5,exp,max}$ and $s_{5,exp,min}$, significant pitch motion $s_{5,sig}$, maximum significant pitch motion $s_{5,sig,max} = 1.86 \cdot s_{5,sig}$ and ratio of maximum measured pitch to maximum significant pitch $|s_{5,exp}|_{max}/s_{5,sig,max}$.

4.2 Results for the crane vessel

The crane vessel considered for the investigations of the bending moments is a ship with a large block coefficient of $c_B = 0.88$ and a crane mounted at the stern. Crane operations are performed only during periods of good weather in order to minimize motions. Nevertheless, also crane vessels can encounter severe weather conditions, e. g. during transit. Compared to a stationary FPSO, crane vessels can avoid the most extreme conditions by sailing into calmer waters like a normal ship. Nonetheless, severe conditions cannot be avoided at all times and thus, crane ships have to endure extreme loads due to high steep waves. The investigation of the crane vessel will be performed in analogy to the investigation of the FPSO, starting with frequency-domain and rule examination followed by the time-domain analysis of the crane vessel facing the *New Year Wave* and *Rogue Wave* sequences synthesized by both, the *experimental optimization* and *linear optimization* approach.

4.2.1 Transfer functions of bending moments and motions of the crane vessel

The transfer function of the bending moment of the crane vessel, determined by model tests and calculated by SEAWAY and WAMIT, is given in Fig. 4.14. Generally, the transfer function of the bending moments of the crane vessel has the same characteristic as for the FPSO ship. The maximum amplitude is observed at a wave frequency of 0.55 rad/s corresponding to the ship length of $L_{pp} = 194.4$ m. The cancellation frequency and the second maximum corresponds to a wave lengths of $L_{pp}/2$ and $L_{pp}/3$ respectively. The maximum amplitudes and peak periods of the bending moment transfer function are predicted reasonably well by WAMIT and SEAWAY. The slight overestimation of the maximum amplitudes can be attributed to viscous effects at the experiments which are not considered for in the calculations.

For the heave and pitch motion of the crane vessel the transfer functions are shown in the next section in Fig. 4.16 and Fig. 4.17 and used to estimate maximum responses by statistical means.

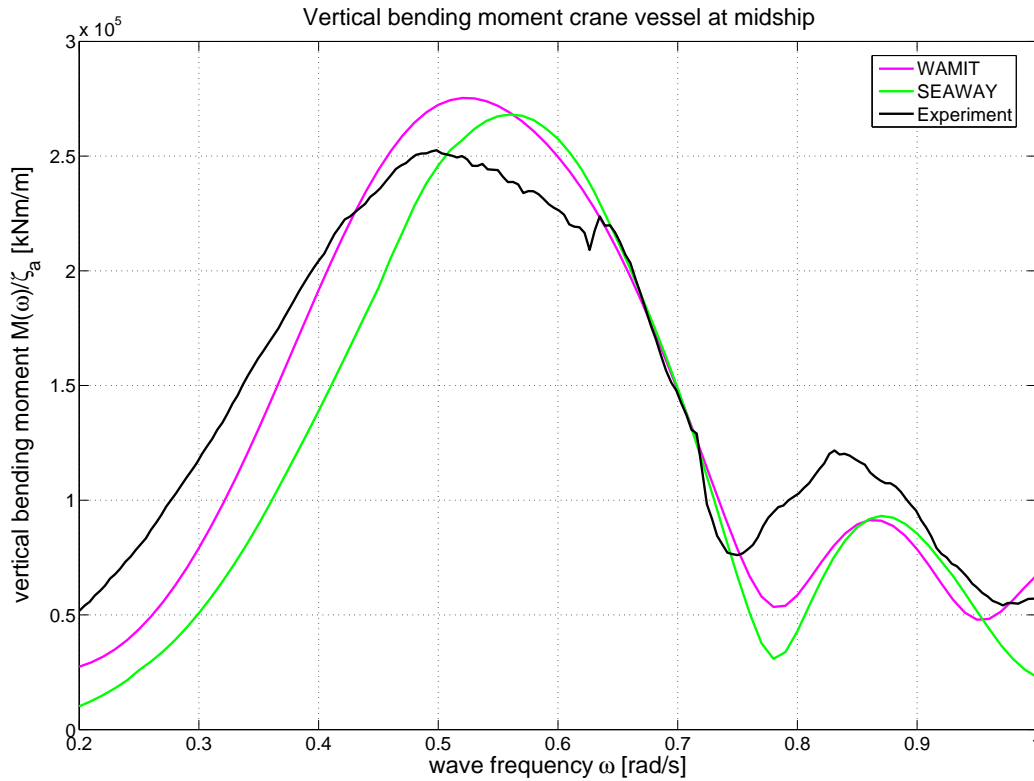


Figure 4.14: Transfer function of the bending moment of the crane vessel, comparing experimental and numerical results. The maximum responses are lower than for the FPSO due to the smaller dimensions of the crane vessel.

4.2.2 Frequency-domain approach and statistical analysis of loads and motions of the crane vessel

The standard procedure to evaluate maximum responses based on transfer functions and sea spectra, as introduced in section 4.1.2, is illustrated for the bending moments of the crane vessel in Fig. 4.15. For the evaluation, the transfer function of the bending moment obtained by model tests is used.

In comparison to the analysis of the bending moments of the FPSO ship (presented in Fig. 4.3), highest significant bending moments are observed in the range of $T_0 = 10$ s with maximum values of $1.04 \cdot 10^5$ kNm/m (amplitude). The smaller period and peak values are due to the fact, that the crane vessel is 65 m shorter than the FPSO and has a displacement of only $\nabla = 65314$ t.

Fig. 4.16 presents the analysis of the heave motion by statistical means. The heave transfer function for the crane vessel is typical for a ship shaped

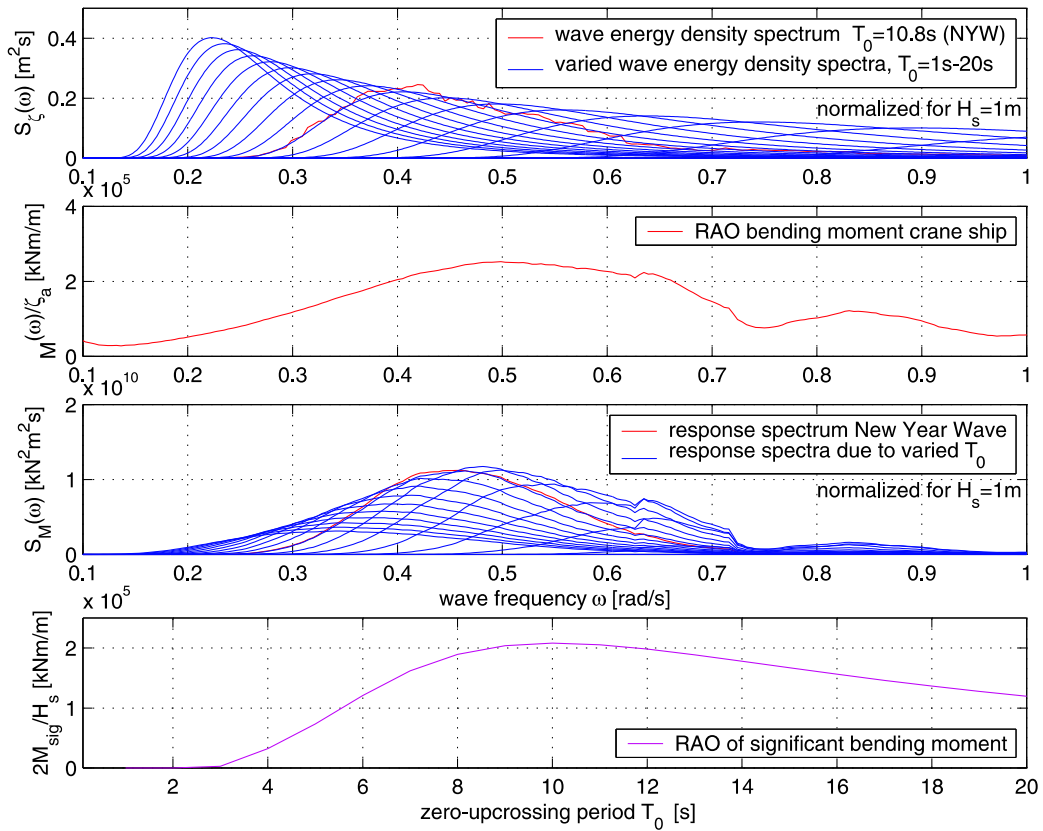


Figure 4.15: Frequency-domain analysis of the bending moments at midship section of the crane vessel: Sea spectra – response amplitude operator – response spectra – significant bending moment double amplitude. Maximum significant amplitudes are observed in the range of $T_0 = 10$ s.

structure with high block coefficient: No resonance peaks are observed due to large damping. In comparison to the FPSO, larger significant heave motions are estimated at the same periods due to the smaller size of the crane vessel. Thus, in identical sea states larger heave motions are expected for the crane vessel, whereas the bending moments are smaller.

The analysis of the pitch transfer function illustrated in Fig. 4.17, shows that for the crane vessel, the maximum value of the significant pitch motion is larger than for the FPSO and shifted towards shorter periods, i. e. the crane vessel pitches more, in particular in sea states with shorter periods. Summarizing, from the statistical analysis follows, that the seakeeping behavior of the FPSO ship is better than for the crane vessel, purely due to its geometrical dimensions, with the drawback of larger bending moments.

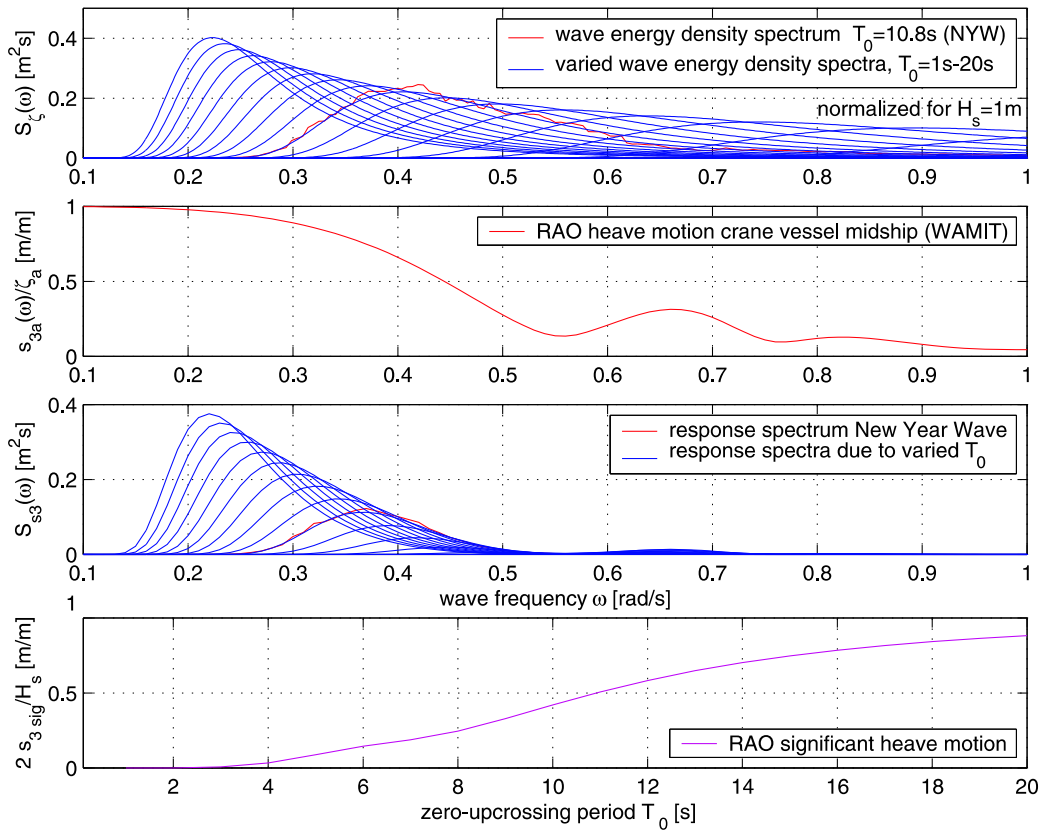


Figure 4.16: Frequency-domain analysis of the heave motion of the crane vessel: Sea spectra – response amplitude operator – response spectra – significant heave motion double amplitude. The significant heave motion converges towards 1 for large periods. Thus, the ship follows the wave motion in long waves.

4.2.3 Comparison to classification rules

As the hull of the crane vessel is typical for a ship, the design of the longitudinal strength must comply with classification rules for ships. For the crane vessel, the maximum wave induced vertical bending moments are (Det Norske Veritas (2000)):

- $-2.38 \cdot 10^6$ kNm for sagging
- $2.28 \cdot 10^6$ kNm for hogging.

The bending moments induced by waves are dominant in comparison to the still water bending moments, caused by unbalanced mass distribution of

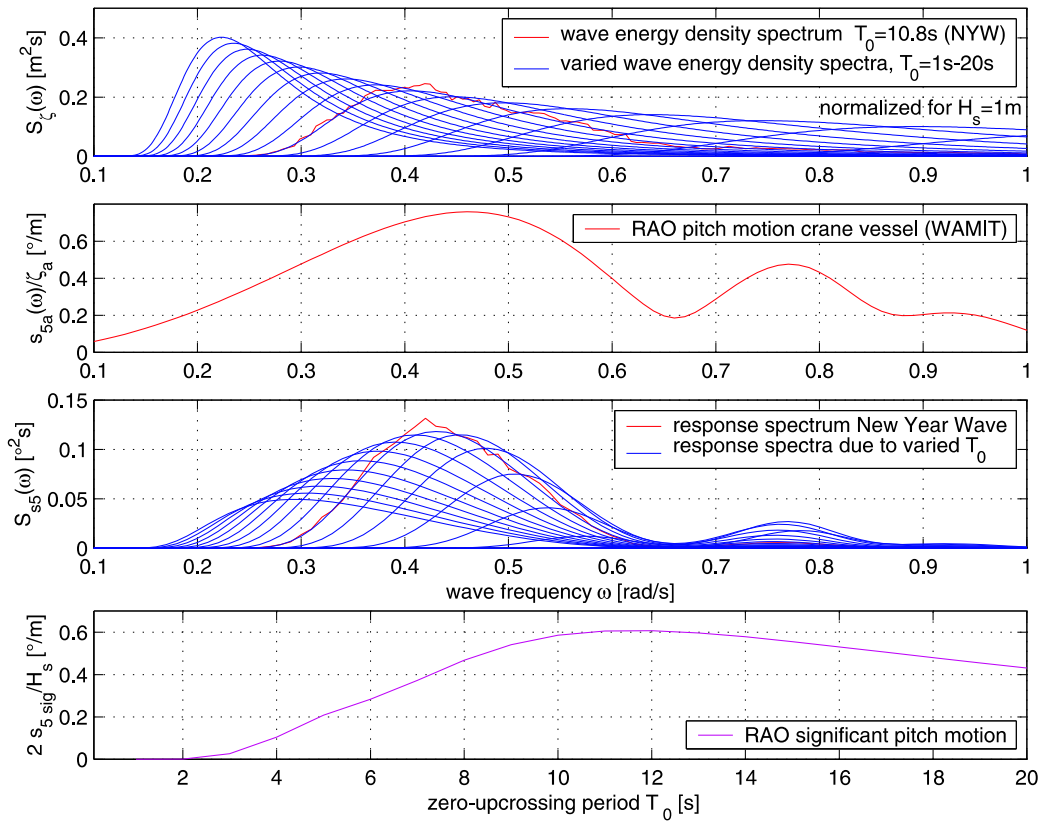


Figure 4.17: Frequency-domain analysis of the pitch motion of the crane vessel: Sea spectra – response amplitude operator – response spectra – significant pitch double amplitude. The pitch transfer function looks similar to the transfer function of the bending moments, resulting in an similar transfer function of the significant pitch motion.

different load cases. According, to the classification rules still water bending moments are $-1.41 \cdot 10^6$ kNm for sagging and $1.51 \cdot 10^6$ kNm for hogging, documenting that wave action is the crucial parameter for the longitudinal strength design of ships.

4.2.4 Time-domain investigation of the crane vessel encountering the *New Year Wave*

As a first example, the crane vessel is exposed to the *New Year Wave* and Fig. 4.18 presents the wave sequence realized in the wave tank and the associated heave and pitch motions as well as the bending moments. In addition, simulation results, calculated based on the transfer functions obtained by WAMIT and SEAWAY, are given. In general, the responses are predicted reasonably well, although both numerical codes tend to underestimate maximum values for the heave and pitch motion.

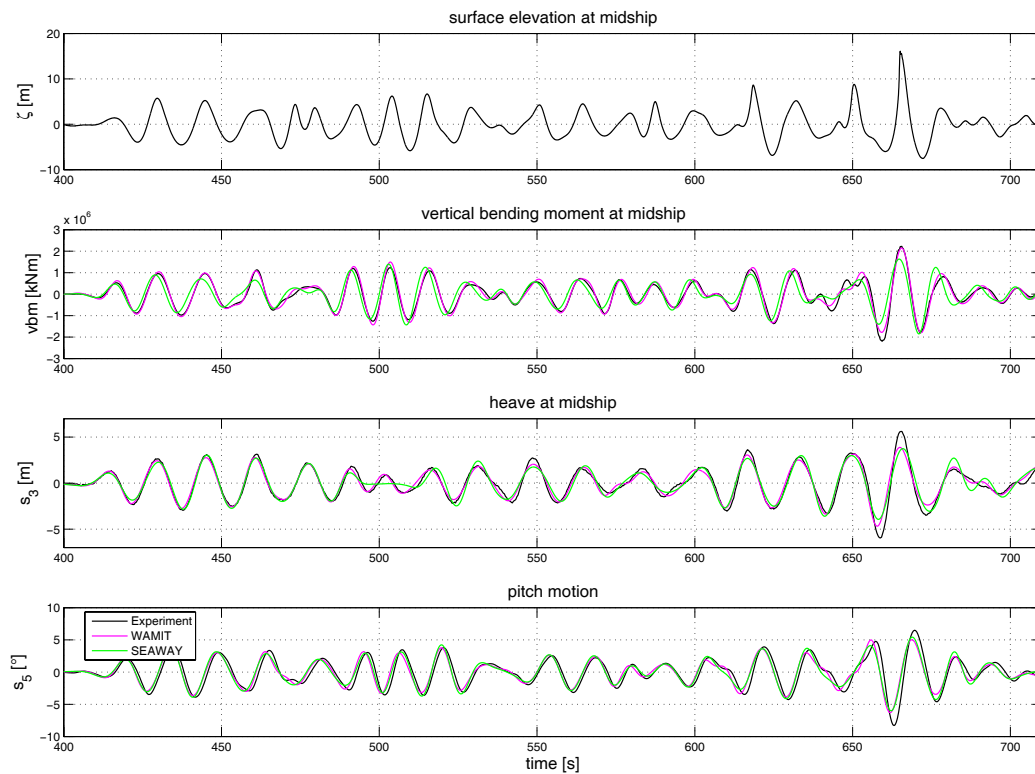


Figure 4.18: Crane vessel encountering the *New Year Wave*: Comparison of experimental and numerical results: *New Year Wave* – vertical bending moment at midship – heave motion – pitch motion. The *New Year Wave* causes bending moments just within limitation of classification rules.

Table 4.9 compares the experimentally obtained responses to the significant values from the statistical approach based on Pierson-Moskowitz spectra with a significant wave height of 11.92 m and zero-upcrossing period of 10.8 s. Maximum bending moments and heave motions are well predicted by statis-

tics, whereas the pitch motion from time-domain analysis is 24% larger. The maximum sagging moment of $-2.19 \cdot 10^6$ kNm and the maximum hogging moment of $2.23 \cdot 10^6$ kNm of the crane vessel are just within the limits of classification rules.

Responses of the crane vessel due to the <i>New Year Wave</i> impact					
	$s_{exp,max}$	$s_{exp,min}$	s_{sig}	$s_{sig,max}$	$ s_{exp} _{max}/s_{sig,max}$
moment [10^6 kNm]	2.23	-2.29	1.22	2.27	1.01
heave [m]	5.61	-5.97	3.02	5.62	1.06
pitch [$^\circ$]	6.49	-8.31	3.62	6.72	1.24

Table 4.9: Bending moments, heave and pitch motion of the crane vessel due to the *New Year Wave*, comparing values from statistics and model tests: Measured maximum and minimum responses $s_{exp,max}$ and $s_{exp,min}$, significant amplitudes s_{sig} , maximum significant amplitudes $s_{sig,max}$, and ratio of maximum measured response to maximum significant response $|s_{exp}|_{max}/s_{sig,max}$.

4.2.5 Variation of the location of encounter between the crane vessel and the *New Year Wave*

To achieve detailed information on the Freak Wave impact, the sensitivity of the bending moments depending on the position of the crane vessel in the wave tank is investigated. Therefore, nine different locations are selected: $-3/2L_{pp}$, $-1L_{pp}$, $-1/2L_{pp}$, $-1/4L_{pp}$, initial position, $+1/4L_{pp}$, $+1/2L_{pp}$, $+1L_{pp}$, $+3/2L_{pp}$. Fig. 4.19 gives an impression of the *New Year Wave* passing under the bow of the crane vessel. Beside extreme bending moments such a Rogue Wave will also cause high pressure loads at the bow and green water on deck. In Table 4.10, the measured wave elevations and corresponding bending moments are summarized for the nine different locations of encounter.

Crane vessel encountering the <i>New Year Wave</i>					
	wave height			bending moment	
	maximum [m]	trough [m]	crest [m]	hogging [10^6 kNm]	sagging [10^6 kNm]
$x_0 - \frac{3}{2}L_{pp}$	23.92	8.86	15.06	2.37	2.17
$x_0 - L_{pp}$	25.03	11.38	13.65	2.10	2.54
$x_0 - \frac{1}{2}L_{pp}$	23.75	12.05	11.69	2.25	2.54
$x_0 - \frac{1}{4}L_{pp}$	24.52	11.16	13.36	2.28	2.32
$x_0 = x_{orig}$	23.65	7.54	16.11	2.23	2.19
$x_0 + \frac{1}{4}L_{pp}$	21.45	8.42	13.03	2.36	2.10
$x_0 + \frac{1}{2}L_{pp}$	20.27	8.88	11.39	2.45	2.49
$x_0 + L_{pp}$	19.78	10.22	9.56	2.00	2.26
$x_0 + \frac{3}{2}L_{pp}$	20.06	9.35	10.71	2.11	2.27

Table 4.10: Maximum wave heights and corresponding bending moments of the crane vessel for nine different positions of the *New Year Wave* in the wave tank. The *New Year Wave* turns out to be more severe at positions further up- and downstream resulting in larger bending moments.

Highest responses are observed $-1/2L_{pp}$ and $-1L_{pp}$ upstream for the sagging moment and $+1/2L_{pp}$ downstream for the hogging moment causing +16%, +10% respectively higher loads than observed at the initial position. The reference Freak Wave sequence (initial position) is not the highest wave. Just one ship length further upstream (at $x_0 - L_{pp}$) the maximum wave height is 25 m, due to a very deep trough of -12.05 m that causes the maximum sagging moment. The maximum hogging moments are not observed when the largest crest is encountered, as one would possibly expect, but $+1/2L_{pp}$

further downstream. This is quite surprising, underlining the importance of the knowledge of the local wave characteristics. The maximum loads observed are slightly higher than values predicted by the frequency-domain approach and by classification rules.

These findings are in accordance with the results of the FPSO. Also for the FPSO, larger sagging moments are observed upstream and larger hogging moments downstream, i. e. both vessels show similar responses due to identical wave sequences. This could have been expected, since both ships are box shaped due to high block coefficients.



Figure 4.19: Impression of the crane vessel model facing the *New Year Wave* in the wave tank. Beside extreme bending moments, encountering the *New Year Wave* causes also high impact loads on the bow and green water on deck.

4.2.6 Crane vessel in Rogue Waves integrated in storm seas

In Fig. 4.20 the measured wave train generated by the *experimental optimization* process as well as the corresponding bending moments, heave and pitch motions are presented. For comparison, calculation results by WAMIT and SEAWAY are also given. As mentioned previously, ships that are designed according to classification rules should endure a storm with maximum significant wave heights in the range of 16.5 m to 18.3 m. Thus, this storm sea with a significant wave height of 13 m is quite moderate and very likely to be encountered during the lifetime of the vessel.

Nevertheless, the integrated Rogue Wave causes extreme responses not covered by the standard statistical methods and design rules. From Table 4.11 follows, that the experimentally obtained heave motion is nearly twice as large than estimated by statistical means, also the maximum pitch angle is 48% larger than expected. Compared to the maximum significant bending moment of $2.47 \cdot 10^6$ kNm for a sea state with $H_s = 13$ m and $T_p = 13$ s, the measured hogging moment is 27% larger. Rule requirements for the hogging

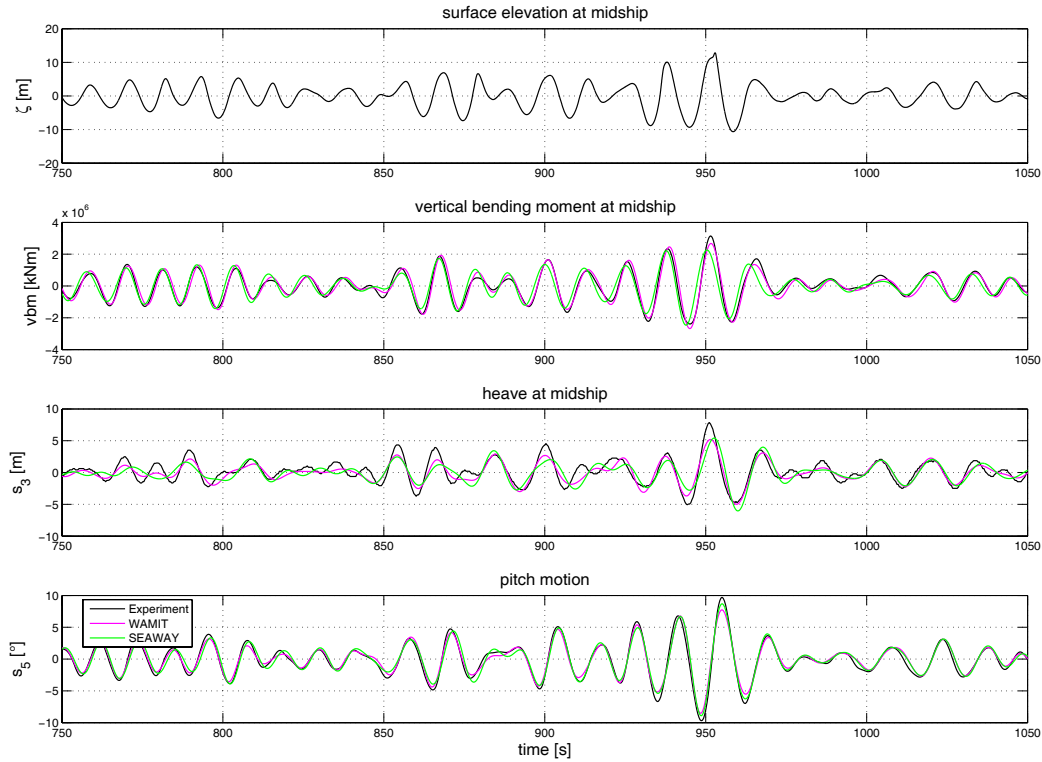


Figure 4.20: Storm sea with embedded Rogue Wave generated by the *experimental optimization* approach and associated responses of the crane vessel, $H_{max}/H_s = 2$, $H_s = 13$ m, $T_p = 13$ s, $\gamma = 1$. The observed responses are significantly larger than estimated by statistics. Thus, the *experimental optimization* approach proves its potential for the synthesization and investigation of extreme wave scenarios.

moment are exceeded by 39%. Note, that for the crane vessel the hogging moments are larger than the maximum sagging moments in this wave sequence, whereas the FPSO shows a contrary behavior pointing out the importance of detailed investigations.

The underestimation of the extreme responses in this wave sequence is remarkable, as the ratio of H_{max}/H_s is only 2, and waves with such a ratio of H_{max}/H_s or larger are found to occur quite frequently as documented in the analysis of a storm presented in chapter 1. As Rogue Waves with ratios of H_{max}/H_s of up to 2.55 have been recorded during this storm, consequently, the crane vessel is exposed to four different storm conditions generated by the *linear optimization* process, with integrated Rogue Waves with ratios of H_{max}/H_s in the range of 2.40 to 2.68. These are the identical Rogue Wave

Responses of crane vessel due to experimentally optimized Rogue Wave					
	$s_{exp,max}$	$s_{exp,min}$	s_{sig}	$s_{sig,max}$	$ s_{exp} _{max}/s_{sig,max}$
moment [10^6 kNm]	3.14	-2.40	1.33	2.47	1.27
heave [m]	7.86	-5.07	2.14	3.98	1.97
pitch [$^\circ$]	9.72	-9.70	3.52	6.55	1.48

Table 4.11: Bending moments, heave and pitch motions of the crane vessel comparing statistical and measured values: Measured maximum and minimum responses $s_{exp,max}$ and $s_{exp,min}$, significant amplitudes s_{sig} , maximum significant amplitudes $s_{sig,max}$, and ratio of maximum measured response to maximum significant response $|s_{exp}|_{max}/s_{sig,max}$. The observed heave motion is nearly twice as large than predicted by frequency-domain analysis.

scenarios the FPSO has been exposed to and results are therefore comparable.

Results of these Rogue Wave encounters are presented in Fig. 4.21 to Fig. 4.24. In particular, Fig. 4.21 and Fig. 4.22 give the vertical bending moments and the associated heave and pitch motions for the wave scenarios with $H_s = 13$ m, comparing numerical simulations by WAMIT and by SEAWAY to model test data. Fig. 4.23 and Fig. 4.24 show the results for sea states with $H_s = 12$ m. The most extreme ratio of $H_{max}/H_s = 2.68$ realized by the *linear optimization* process can be found in Fig. 4.24.

In general, the agreement between results of numerical simulations and of model tests is convincing, although differences are noticeable. Even though both numerical programs are based on linear wave theory and therefore only valid for small waves, the embedded Rogue Wave events are well represented. In Table 4.12 the maximum values of the vertical sagging and hogging moments are given and compared to the (maximum) significant bending moment amplitudes. A maximum ratio of measured moment to significant bending moment amplitude $|M_{exp}|_{max}/M_{sig,max}$ of 1.51 is found for wave scenario C, i. e. the measured value is 51% larger than could be expected from statistics. This is amazing, as wave sequence C has the smallest ratio of $H_{max}/H_s = 2.4$ in combination with the smallest significant wave height of $H_s = 12$ m. These result points out, that the maximum responses are sensitive to local wave pattern and wave grouping. The traditional frequency-domain approach underestimates the maximum responses clearly.

In comparison to requirements from classification societies, the registered maximum hogging moment of $3.69 \cdot 10^6$ kNm is 62% larger than the $2.28 \cdot 10^6$ kNm estimated by the rules. In consequence, a crane vessel designed

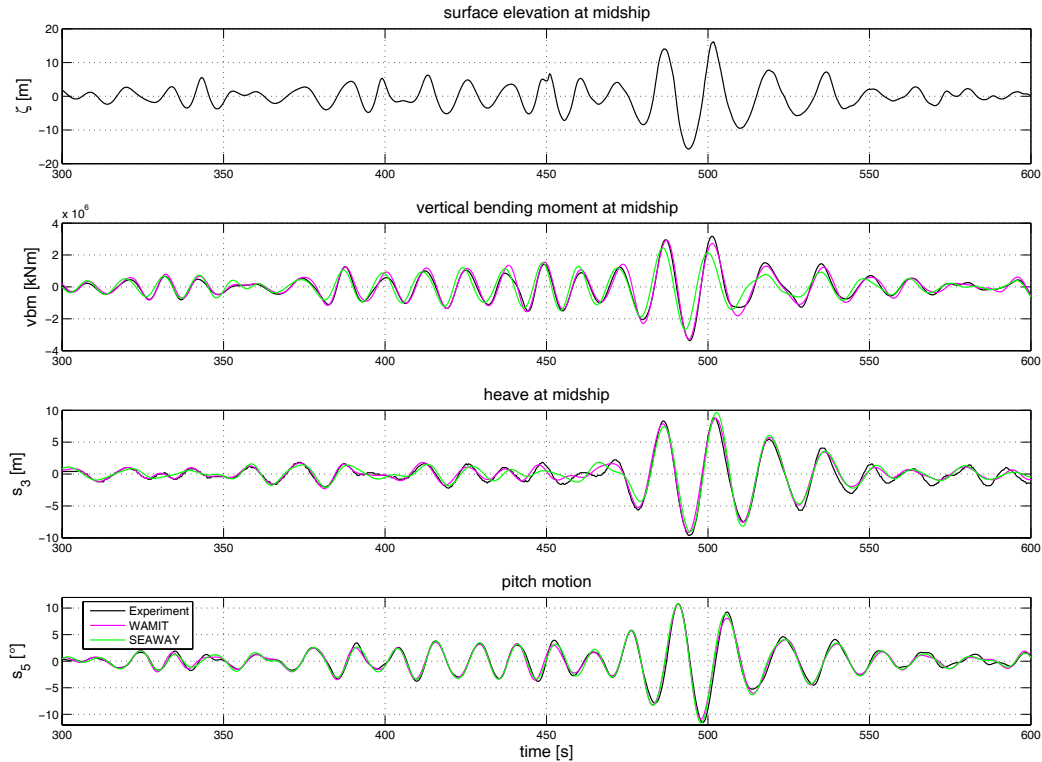


Figure 4.21: Responses of the crane vessel due to storm scenario A, generated by the *linear optimization* approach: $T_p = 15$ s, $H_s = 13$ m, $H_{max} = 31.85$ m and $H_{max}/H_s = 2.45$. The bending moments as well as the heave and pitch motions are well predicted by the seakeeping codes, although this codes are based on linear wave theory.

according to these rules should avoid encountering a Rogue Wave. For the future, a system warning the crew of a ship some time before the occurrence of a Rogue Wave is desirable. Such systems could be based on the nautical radar measuring the surrounding wave field and a prediction method calculating the wave sequence that the ship will encounter in advance.

Concerning the heave and pitch motions of the crane vessel due to the wave scenarios synthesized by the *linear optimization* process, Table 4.13 and 4.14 summarize the responses obtained by model tests. In all four wave scenarios, the maximum motions, both heave and pitch, due to the embedded Rogue Waves exceed the statistically estimated values by around 50%. These findings are in accordance with the results of the FPSO vessel, also the degree of underestimation of the maximum values by statistical means it similar.

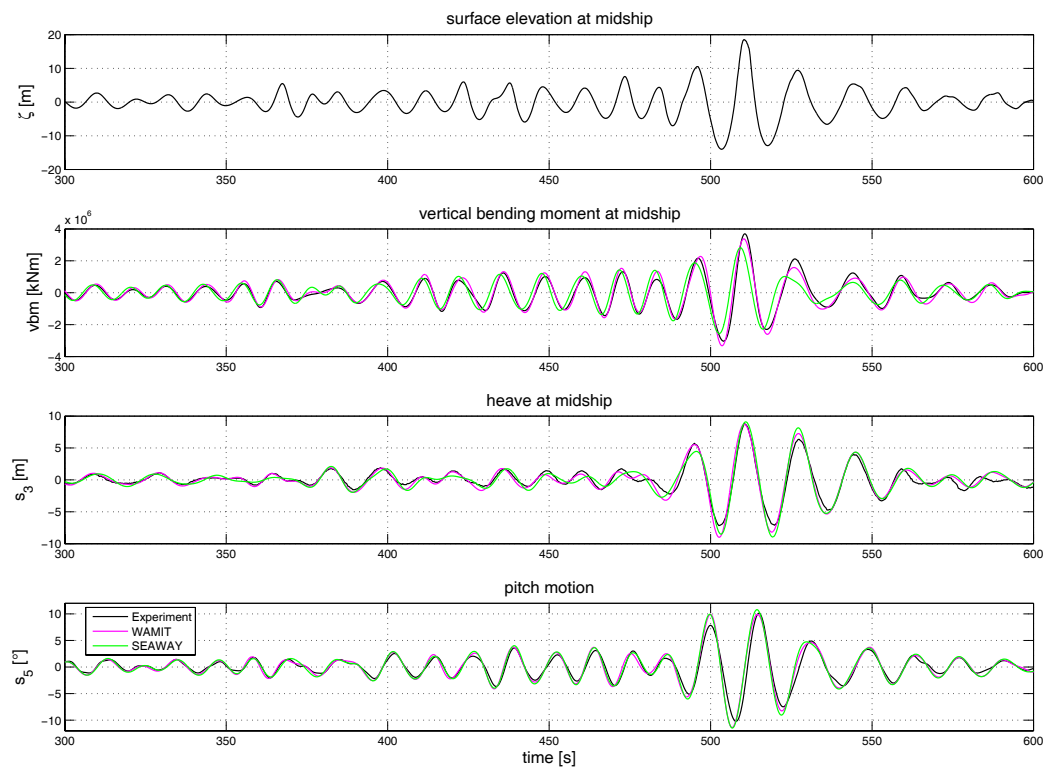


Figure 4.22: Responses of the crane vessel due to storm scenario B: $T_p = 15$ s, $H_s = 13$ m, $H_{max} = 32.56$ m and $H_{max}/H_s = 2.50$. The time-domain analysis reveals the significance of the Rogue Wave impact, as statistical methods underestimate the consequences of these extreme events.

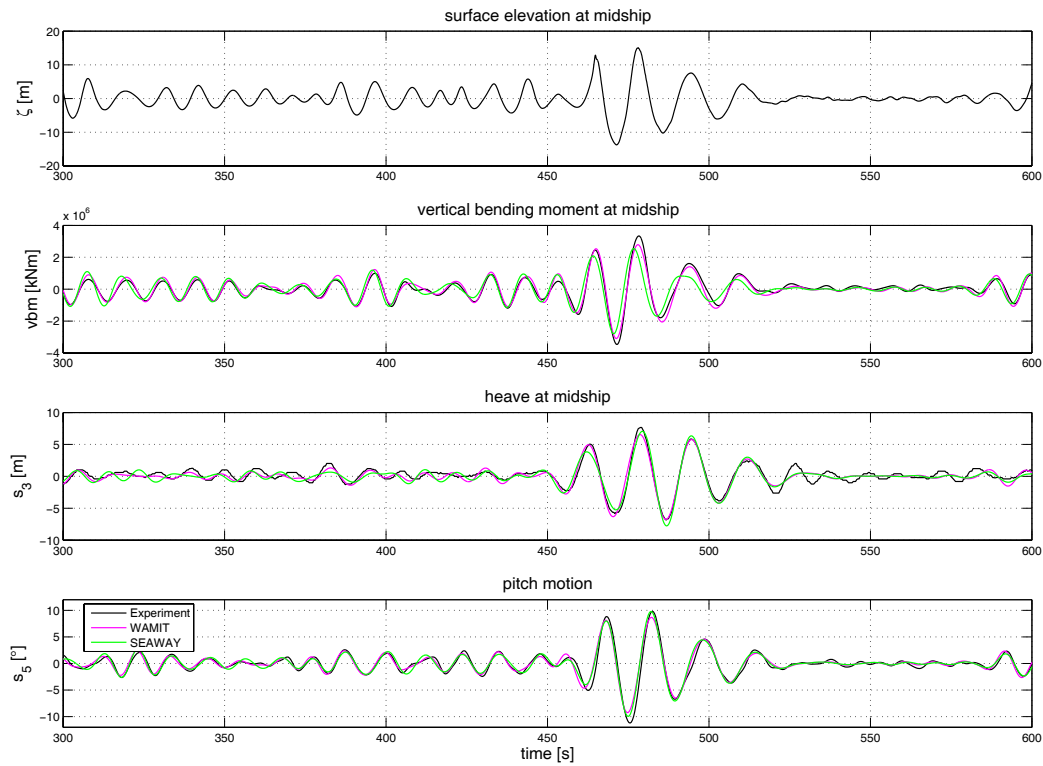


Figure 4.23: Responses of the crane vessel due to storm scenario C: $T_p = 14$ s, $H_s = 12$ m, $H_{max} = 28.83$ m and $H_{max}/H_s = 2.40$. Storm scenario C appears to be the worst for the crane vessel since the exceedance of the statistical values is largest. This is surprising, as this storm scenario has the lowest ratio of $H_{max}/H_s = 2.40$ of the four Rogue Wave sequences synthesized by the *linear optimization* approach.

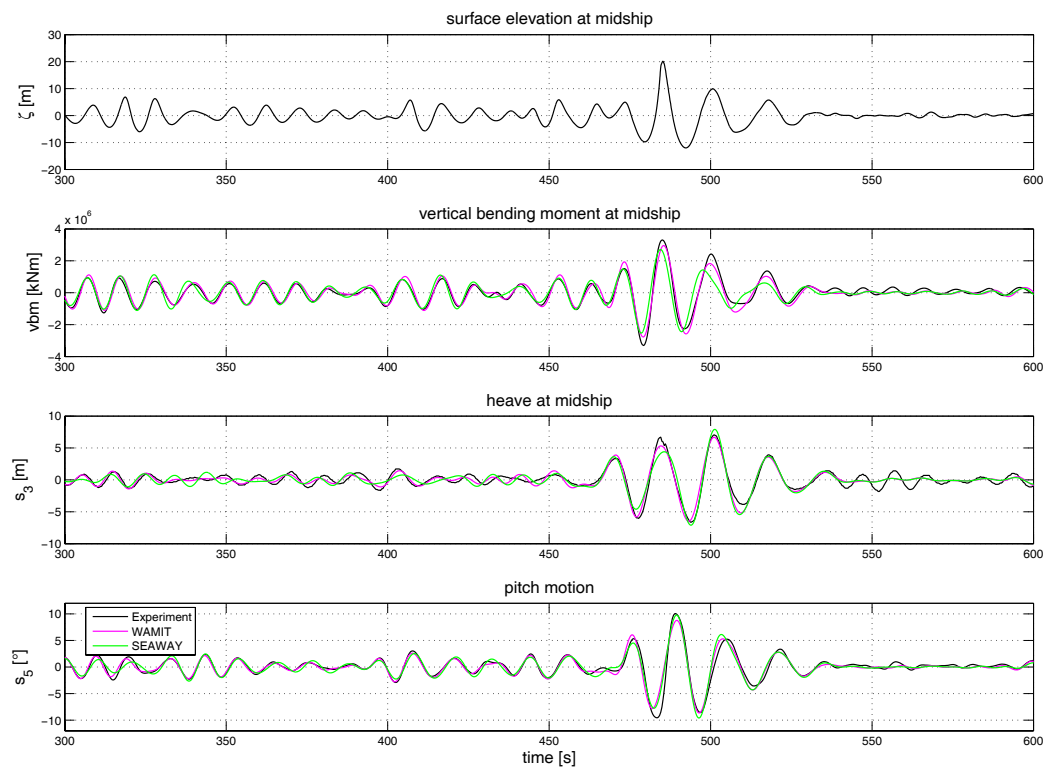


Figure 4.24: Responses of the crane vessel due to storm scenario D: $T_p = 14$ s, $H_s = 12$ m, $H_{max} = 32.15$ m and $H_{max}/H_s = 2.68$. The largest wave causes not inevitably the highest responses, rather the local wave characteristics as well as the wave pattern determine the reactions.

Bending moments of the crane vessel						
Sea state		Experiment		Statistics		
	H_{max}/H_s	$M_{hogg,max}$	$M_{sagg,max}$	M_{sig}	$M_{sig,max}$	$ M_{exp} _{max}/M_{sig,max}$
	[-]	[10 ⁶ kNm]	[10 ⁶ kNm]	[10 ⁶ kNm]	[10 ⁶ kNm]	[-]
(A)	2.45	3.31	3.51	1.33	2.47	1.42
(B)	2.50	3.69	3.04	1.33	2.47	1.49
(C)	2.40	3.42	3.51	1.25	2.32	1.51
(D)	2.68	3.31	3.31	1.25	2.32	1.43

Table 4.12: Vertical bending moments of the crane vessel due to storm seas: Sea state parameters, maximum measured hogging moment $M_{hogg,max}$ and sagging moment $M_{sagg,max}$, significant bending moment amplitude M_{sig} , maximum significant bending moment $M_{sig,max} = 1.86 \cdot M_{sig}$ and ratio of maximum measured moment to maximum significant bending moment $|M_{exp}|_{max}/M_{sig,max}$.

Heave motions of the crane vessel							
Sea state		Experiment			Statistics		
	H_{max}/H_s	H_{max}	$s_{3,exp,max}$	$s_{3,exp,min}$	$s_{3,sig}$	$s_{3,sig,max}$	$ s_{3,exp} _{max}/s_{3,sig,max}$
	[-]	[m]	[m]	[m]	[m]	[m]	[-]
(A)	2.45	31.85	8.76	-9.62	3.30	6.13	1.57
(B)	2.50	32.65	8.81	-7.16	3.30	6.13	1.44
(C)	2.40	28.83	7.66	-6.86	2.52	4.69	1.63
(D)	2.68	32.15	7.06	-6.66	2.52	4.69	1.51

Table 4.13: Heave motions of the crane vessel due to storm seas: Sea state parameters, maximum measured heave motion $s_{3,exp,max}$ (up) and $s_{3,exp,min}$ (down), significant heave motion amplitude $s_{3,sig}$, maximum significant heave motion $s_{3,sig,max} = 1.86 \cdot s_{3,sig}$ and ratio of maximum measured heave to maximum significant heave motion $|s_{3,exp}|_{max}/s_{3,sig,max}$.

Pitch motions of the crane vessel							
Sea state		Experiment		Statistics			
	H_{max}/H_s	H_{max}	$s_{5,exp,max}$	$s_{5,exp,min}$	$s_{5,sig}$	$s_{5,sig,max}$	$ s_{5,exp} _{max}/s_{5,sig,max}$
	[-]	[m]	[°]	[°]	[°]	[°]	[-]
(A)	2.45	31.85	10.80	-11.52	3.94	7.33	1.57
(B)	2.50	32.65	10.12	-10.23	3.94	7.33	1.40
(C)	2.40	28.83	9.82	-11.21	3.52	6.54	1.71
(D)	2.68	32.15	10.05	-9.55	3.52	6.54	1.54

Table 4.14: Pitch motions of the crane vessel due to storm seas: Sea state parameters, maximum measured pitch motion $s_{5,exp,max}$ and $s_{5,exp,min}$, significant pitch amplitude $s_{5,sig}$, maximum significant pitch $s_{5,sig,max} = 1.86 \cdot s_{5,sig}$ and ratio of maximum measured pitch to maximum significant pitch motion $|s_{5,exp}|_{max}/s_{5,sig,max}$.

4.3 Conclusions of the experimental and numerical investigation of the FPSO and the crane vessel encountering Rogue Waves

This chapter presents a comprehensive study of the vertical bending moments as well as the heave and pitch motions of an FPSO ship and a crane vessel due to Rogue Wave impacts with subsequent results:

- All three seakeeping codes applied for the investigation give reliable results, both for structural loads and motions. The overall agreement of the transfer functions is convincing, although differences in peak values and frequencies are noticeable.
- The method to calculate responses in time-domain, based on the transfer functions obtained by WAMIT and SEAWAY and subsequent inverse Fourier transformation, enables the investigation of responses due to Rogue Wave impacts. The overall agreement between simulation results and experimental data is good, although the procedure is based on linear wave theory and neglects nonlinear effects. Thus, these method can be trusted for the investigation of wave-structure interactions in extreme conditions.
- The intensive analysis of the *New Year Wave* scenario reveals that this wave is really an extreme event as responses are partly exceeding the estimations from statistics and rule values.
- By exposing both ships relatively to the incoming *New Year Wave* further downstream and upstream, it is found, that the *New Year Wave* is even more severe at a position upstream confirming the importance of time and phase information and the need for precise simulations and model tests.
- Applying the wave generation method of Hennig (2005) variations of the *New Year Wave* with elongated period and height are generated, keeping the history of the wave train unchanged. Thus, differences in responses can be directly related to the modified Rogue Wave. In consequence the modified *New Year Wave* turned out to be even worse than the original one, resulting in bending moments and motions only predictable with time-domain methods.

- The potential of the *experimental optimization* process presented in Chapter 2 is demonstrated by tailoring a Rogue Wave satisfying pre-defined local and statistical parameter resulting in extreme bending moments and motions.
- The *linear optimization* process is applied to synthesize four sea states with integrated Rogue Waves with H_{max}/H_s ratios of up to 2.68 that give responses clearly exceeding estimations by statistical means an rules.

Summarizing, frequency-domain standard procedures for evaluating maximum bending moments turn out to cover not all Rogue Wave impacts. Maximum values of the observed vertical bending moments are up to twice as large than predicted by the statistical analysis if a ratio of maximum response to significant response of 1.86 is applied. The heave and pitch motions due to Rogue Wave impacts are in some cases also significantly underestimated. Maximum allowable bending moments given by classification rules are underestimating the consequences of such extreme conditions.

However, with time-domain investigation methods and deterministic wave generation methods for model tests, extreme loads and motions due to Rogue Wave impacts can be reliably identified and analyzed in detail.

Chapter 5

Analysis of Splitting Forces, Airgap and Motions of the Semisubmersible *GVA 4000* due to Rogue Wave Impacts

In this chapter, the motions and forces of the semisubmersible *GVA 4000* are investigated. Heave, pitch and roll motions as well as airgap are key characteristics of semisubmersibles in extreme seas. For the ultimate limit state – the 100 years return period – the NORSOK (2004) standard defines a minimum airgap of 1.5 m. For the accidental limit state, either a positive airgap is required, or the structure has to be designed to survive wave impacts on the deck structure.

In this work, the airgap at midship is considered, although large pitch and roll angles can significantly reduce the airgap in the corners, resulting in an increased susceptibility for slamming (Wilde (2003)). Transfer functions for the splitting forces – calculated either by the Morison equation or the radiation-diffraction program WAMIT – are compared to results from model tests. Heave motion, airgap and splitting forces are analyzed by time-domain methods and compared to results of the statistical approach.

5.1 Determination of the transfer function of the splitting forces by the Morison equation

In the following, the transfer function of the splitting forces of the *GVA 4000* is calculated based on the Morison equation. It is assumed that the structure does not disturb the incoming wave field, i. e. diffraction and radiation are not accounted for. The structure is then called hydrodynamic transparent. The geometry of the semisubmersible is simplified. The cross bracings are neglected and the submerged hulls are modelled as cuboids with displacement identical to the original geometry.

The Morison equation describes the total wave forces on offshore structures, i. e. the sum of inertia forces – Froude-Krylov force and hydrodynamic mass force – and nonlinear drag force:

$$F_{Morison} = F_{inertia} + F_{drag}. \quad (5.1)$$

Supposing, that the mass term in the Morison equation prevails over the nonlinear drag force – which is valid for Keulegan-Carpenter numbers $KC < 10$ – the drag force is neglected and the Morison equation can be written as

$$F_{Morison} = F_{inertia} = c_m \rho V \omega^2 \zeta_a e^{-kd}, \quad (5.2)$$

where c_m denotes the inertia coefficient, ρ the density of the fluid, V the submerged volume, ω ($\omega = \frac{2\pi}{T}$) the wave frequency, ζ_a the wave amplitude, k the wave number and d the effective draft. The inertia coefficient c_m is derived from the added mass coefficient c_a by $c_m = 1 + c_a$.

The horizontal forces on the *GVA 4000* consist of the forces acting on the hulls, F_{hull} , and on the columns, F_{column} . The horizontal force acting on one submerged hull is:

$$F_{hull} = c_{m_{hull}} \rho V_{hull} \omega^2 \zeta_a e^{-(k(h_c + h_h/2))}, \quad (5.3)$$

where $h_c + h_h/2$ denotes the effective draft of the hull, with h_c the submerged depth of the columns and h_h the height of the pontoon. For rectangular cylinders, with a breadth to depth ratio of 2.13, a c_a value of 1.7 is found by Wendel (1955). This value is normalized by a reference volume of $V = \pi b^2$

where b is half the depth. With the actual volume of the pontoon of the *GVA 4000*, a value of $c_a = 0.65$ is obtained.

The horizontal forces acting on one column are (Clauss et al. (1988)):

$$F_{column} = c_{m_{column}} \rho g A_{column} \zeta_a (1 - e^{-kh_c}), \quad (5.4)$$

where A_{column} is the cross section area of the column. c_a of the column equals 1 and therefore $c_{m_{column}} = 2$.

The total wave force acting on one side of the semisubmersible is the sum of the forces acting on the hull and on both columns:

$$F_{oneside} = F_{hull} + 2F_{column}. \quad (5.5)$$

The horizontal force on the entire semisubmersible, which is responsible for the resultant horizontal motions, is the phase correct addition of the forces on both sides:

$$F_{external} = F_{oneside} (\sin(kb_0/2 - \omega t) + \sin(-kb_0/2 - \omega t)) \quad (5.6)$$

Here, the phase shift between the forces acting on both sides is considered, where b_0 denotes the distance between the hulls. Applying the relation $\sin \alpha + \sin \beta = 2 \sin(\frac{\alpha+\beta}{2}) \cos(\frac{\alpha-\beta}{2})$, the total force can be rewritten as:

$$F_{external} = -2F_{oneside} \cos(kb_0/2) \sin(\omega t). \quad (5.7)$$

Note, that the maximum external force on the semisubmersible is twice the force on one side. This is the case for long waves with respect to the structure, when forces acting on both sides are in phase.

The splitting forces are calculated from the difference of the forces acting on both sides:

$$F_{splitting} = F_{oneside} \frac{\sin(kb_0/2 - \omega t) - \sin(-kb_0/2 - \omega t)}{2}, \quad (5.8)$$

Applying the relation $\sin \alpha - \sin \beta = 2 \cos(\frac{\alpha+\beta}{2}) \sin(\frac{\alpha-\beta}{2})$, the splitting forces can be rewritten as:

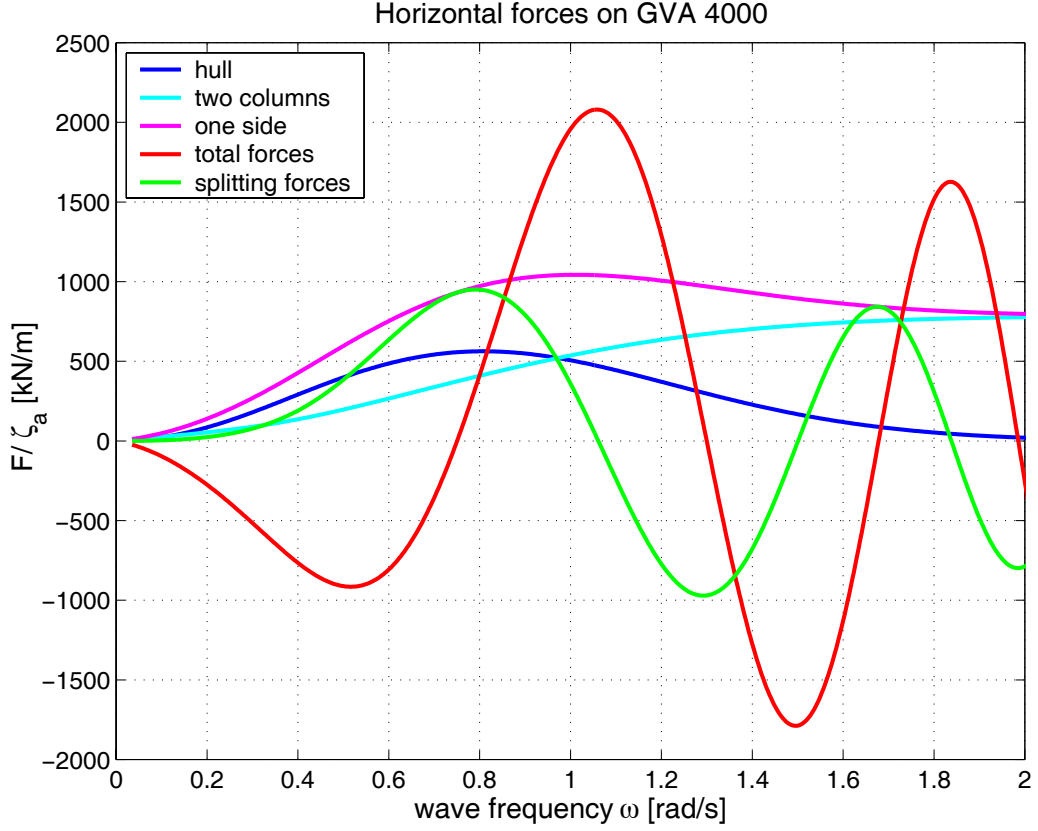


Figure 5.1: Horizontal forces on the semisubmersible *GVA 4000*. The splitting forces (green line) are at a maximum, where the sum of the external forces (red line, denoted as total forces) vanishes, i. e. structural forces are maximal when the horizontal motions are minimal and vice versa.

$$F_{splitting} = F_{oneside} \cos(-\omega t) \sin(-kb_0/2). \quad (5.9)$$

The maximum splitting forces correspond to the maximum forces acting on one hull. This coincides with the forces acting on the hulls in opposite directions, i. e. forces are inversely phased. These conditions are achieved, when the wave length L is $(n + 0.5)$ times the distance b_0 between the hulls ($L = (n + 0.5) \cdot b_0$ with $n = 0, 1, 2, \dots$). As a result, the external horizontal forces vanish and horizontal motions are at a minimum. Since the splitting forces are of important dimensions, they are taken up by cross bracings and by additional stiffeners at the column deck joint.

Fig. 5.1 presents the horizontal forces on: Both, one hull and the columns of one side, the total forces on one side, the resultant forces on the entire

structure and the internal splitting forces as functions of the wave frequency. Note, that the splitting forces (green line) are at a maximum where the sum of the external forces (red line) vanishes and vice versa.

5.2 Transfer functions of the splitting forces and motions of the semisubmersible determined by WAMIT

Response amplitude operators are still an excellent and handy tool for assessing the general seakeeping behavior of a structure, either for comparing the hydrodynamic qualities of different designs, or as a basis for stochastic analysis. Results from WAMIT have been validated and verified by numerous model tests and CFD simulations. Fig. 5.2 shows the transfer function of the splitting forces of the *GVA 4000* calculated by WAMIT and using the Morison equation in comparison to results from model tests. The results are given for beam seas ($\beta = 90^\circ$).

Calculations from the Morison equation show the largest deviation from experimental data due to the fact, that radiation and diffraction phenomena are neglected, the geometry of the semisubmersible is simplified and also viscous forces are not accounted for. Nevertheless, this approach is still useful to estimate the magnitudes of loads on structures. WAMIT results agree well with model test data, although differences are noticeable. For comparison, the transfer function of the splitting forces for the survival draft (blue line) is given. The splitting forces are increased at survival draft, because the hulls are closer to the free surface and therefore orbital water motions as well as velocities and accelerations are larger.

In Fig. 5.3, the transfer functions of the heave motion for two different drafts and wave headings – beam seas (90°) and head seas (180°) – are given. Since the semisubmersible is not rotationally symmetrical the heave transfer functions show a slightly differently behavior for different wave angles. For comparison, the transfer function for heave in head seas at drilling draft, obtained by model tests, is also shown. For long waves, the semisubmersible follows the wave elevation. The heave resonance is around $\omega = 0.28$ rad/s ($T = 22.4$ s) and is therefore located in a range, where most sea states contain only a small amount of energy. The cancellation frequency can be found around $\omega = 0.29$ rad/s. Note, that the measured heave resonance peak gives maximum values of $s_{3a}/\zeta_a = 2.07$, whereas WAMIT gives significant larger values due to the fact that viscous damping is not accounted for.

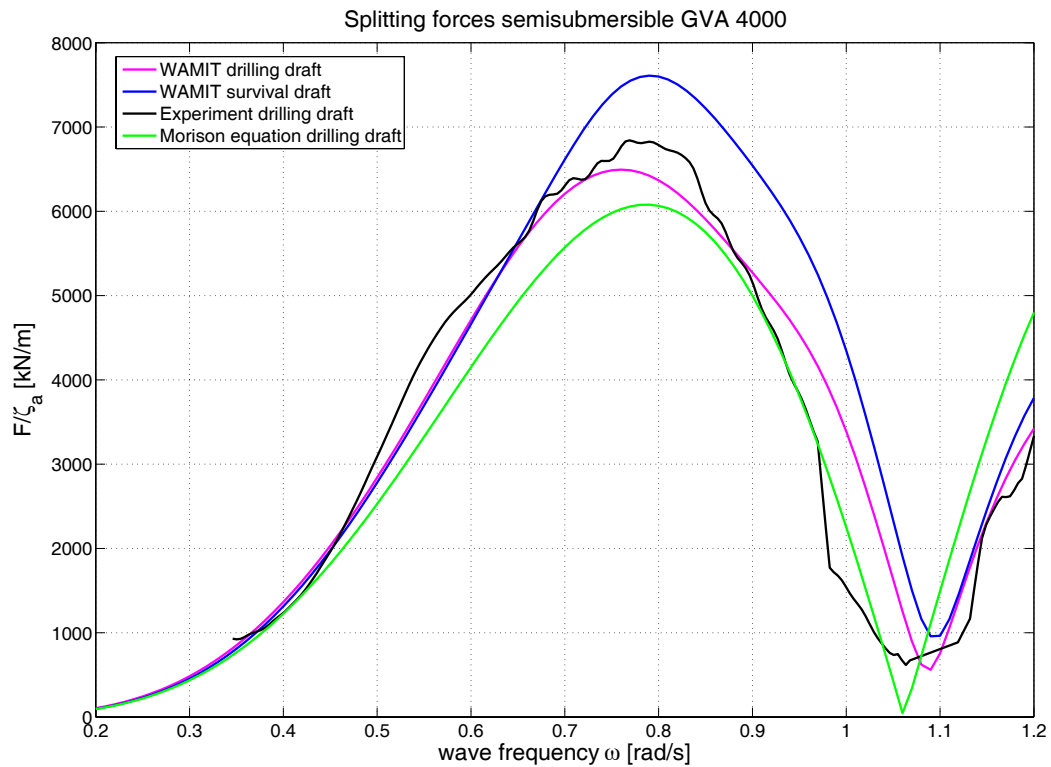


Figure 5.2: Transfer function of the splitting forces of the semisubmersible *GVA 4000* at drilling draft as a result of model tests and calculations in beam seas. For comparison, the blue line gives the transfer function of the splitting forces at survival draft. At survival draft structural responses are larger than for the drilling draft, since the hulls are closer to the water surface with the consequence of higher wave forces.

Generally, viscous damping forces are overestimated in model tests and neglected – therefore underestimated – by WAMIT calculations. This fact allows for the conclusion, that full scale motions at heave resonance are expected to be located between experimental and numerical data. Thus, for the frequency-domain approach presented in the next section, the heave transfer function is truncated at $s_{3a}/\zeta_a = 3$. A profound study of semisubmersible motion behavior at heave resonance (and at the cancellation period) reveals that this value is typical in higher seas as viscous effects are quite significant (Clauss (1978)). In general, viscous effects are beneficial for the motion behavior of semisubmersibles in extreme waves, as the increasing viscous effects force the floating platform to follow the waves, thus increasing the airgap (Östergaard and Schellin (1987)).

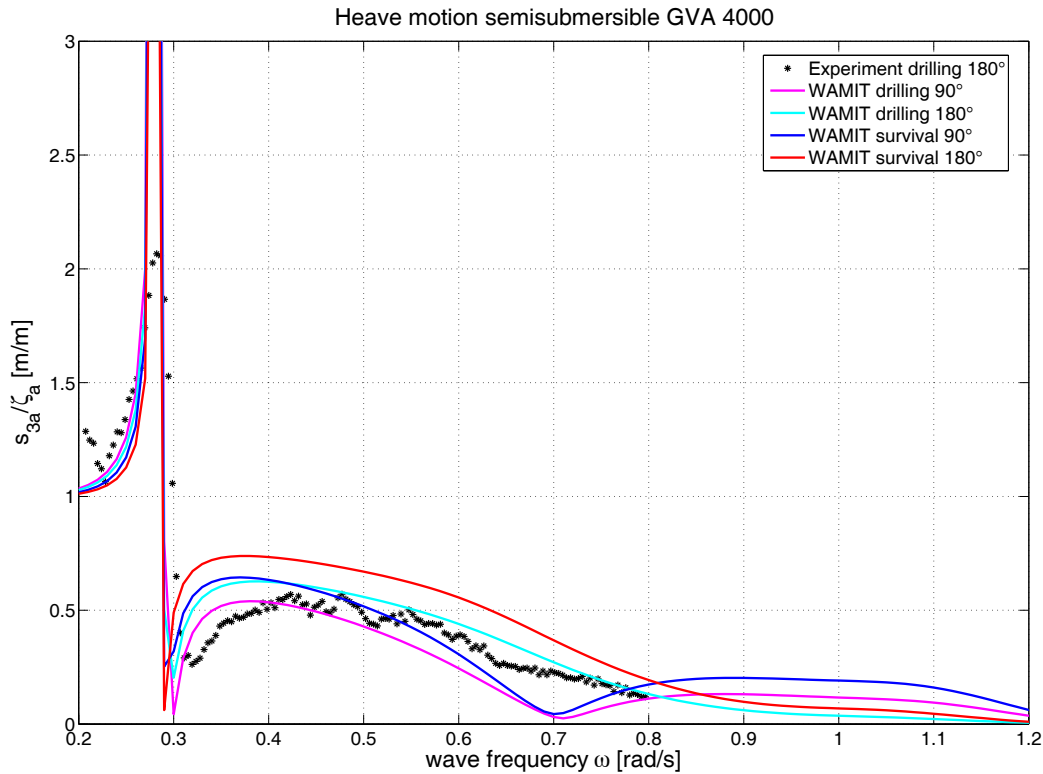


Figure 5.3: Transfer functions of the heave motion of the semisubmersible *GVA 4000* at drilling draft and survival draft for wave angles 90° and 180° . For comparison the experimentally obtained heave transfer function is also given and agrees well with calculations by WAMIT.

The transfer function of the variation in airgap – in the following simply denoted as the transfer function of the airgap – is presented in Fig. 5.4. The resultant airgap is obtained by adding the still water airgap to the variation of airgap as introduced in chapter 3. The airgap transfer functions are derived from the heave transfer functions (Fig. 5.3) by complex subtraction of 1 (see equation 3.8).

For long waves, the transfer function of the variation in airgap equals zero. No relative motion between the semisubmersible and the wave is observed, i. e. the semisubmersible follows the wave motion and the heave transfer function equals one. The resonance peak of the airgap is in the same frequency range as for the heave motion. For short waves, the transfer function of the airgap converges towards one. No vertical motions are observed and the wave amplitude governs the change in airgap.

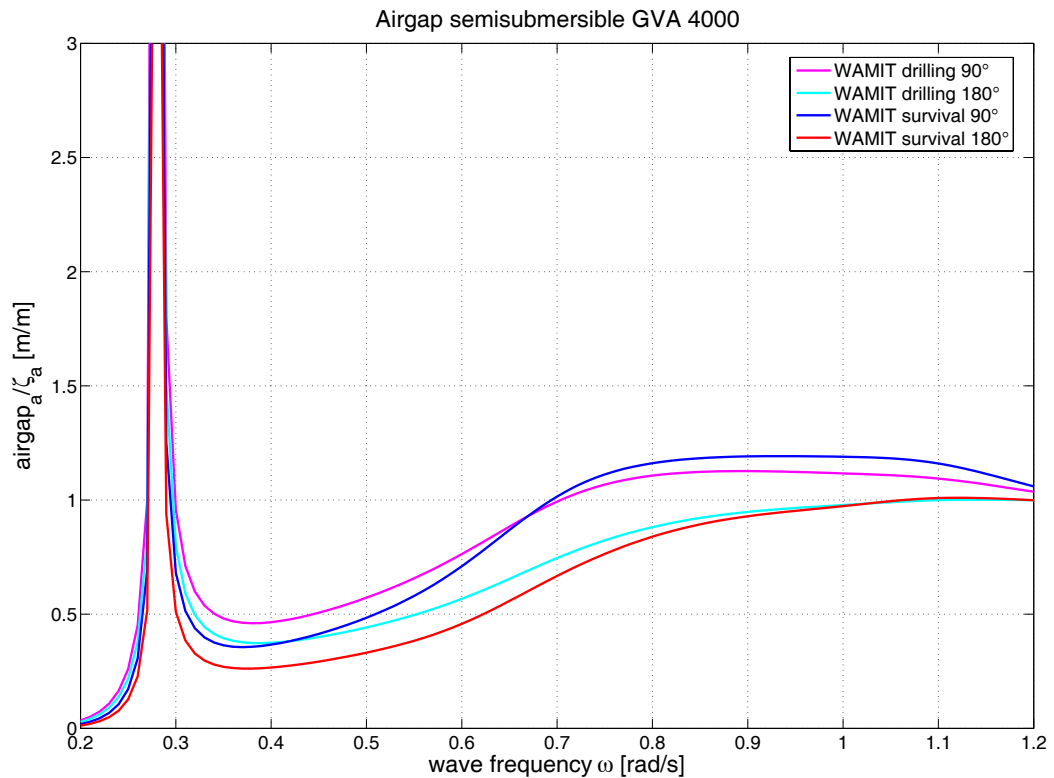


Figure 5.4: Transfer function of the variation in airgap of the semisubmersible *GVA 4000* comparing results from numerical simulations and model tests. The resultant airgap in time-domain is the sum of still water airgap and variation of airgap. The transfer function is derived from the heave transfer function presented in Fig. 5.3.

5.3 Frequency-domain analysis of the splitting forces, airgap and motions of the *GVA 4000*

In analogy to the investigation of the bending moments and motions of the FPSO and the crane vessel presented in chapter 4, the splitting forces, airgap and heave motion of the semisubmersible *GVA 4000* are analyzed statistically. Fig. 5.5 presents the graphs of the normalized Pierson-Moskowitz spectra (top). In addition, the smoothed spectrum of the 20-minutes registration of the *New Year Wave* is included in the upper diagram. Note, that the *New Year Wave* registration coincides well with the Pierson-Moskowitz spectrum. The unusually high wave (within the 20-minutes sequence) leaves

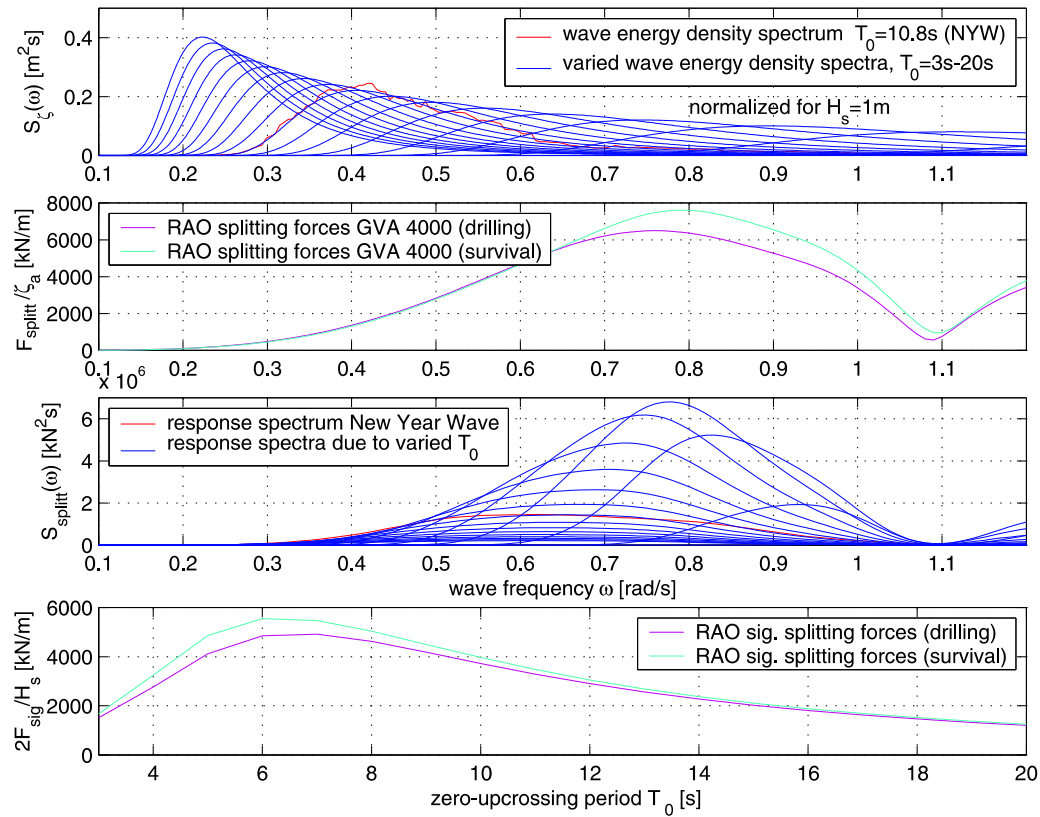


Figure 5.5: Frequency-domain analysis of the splitting forces of the semisubmersible *GVA 4000*: Sea spectra – response amplitude operators – response spectra – significant double amplitudes of splitting forces for drilling and survival draft. The differences observed between drilling and survival draft in the significant transfer functions are only small. Largest responses are expected for sea states with short periods.

no trace in the spectrum. Thus, the *New Year Wave* sequence represents a quite exotic sample of a conventional Pierson-Moskowitz spectrum.

By multiplication of the exciting wave spectra with the squared transfer functions of the splitting forces the response spectra are obtained. From the area under the response spectra follow the significant double amplitudes of the splitting forces for the drilling draft as well as for the survival draft. Maximum responses are observed in sea states with periods in the range $T_0 = 6 \text{ s} - 7 \text{ s}$. For larger zero-upcrossing periods, which are common for storm seas, the significant splitting forces are smaller, i. e. when the environments gets harsher, significant structural responses are fortunately decreasing.

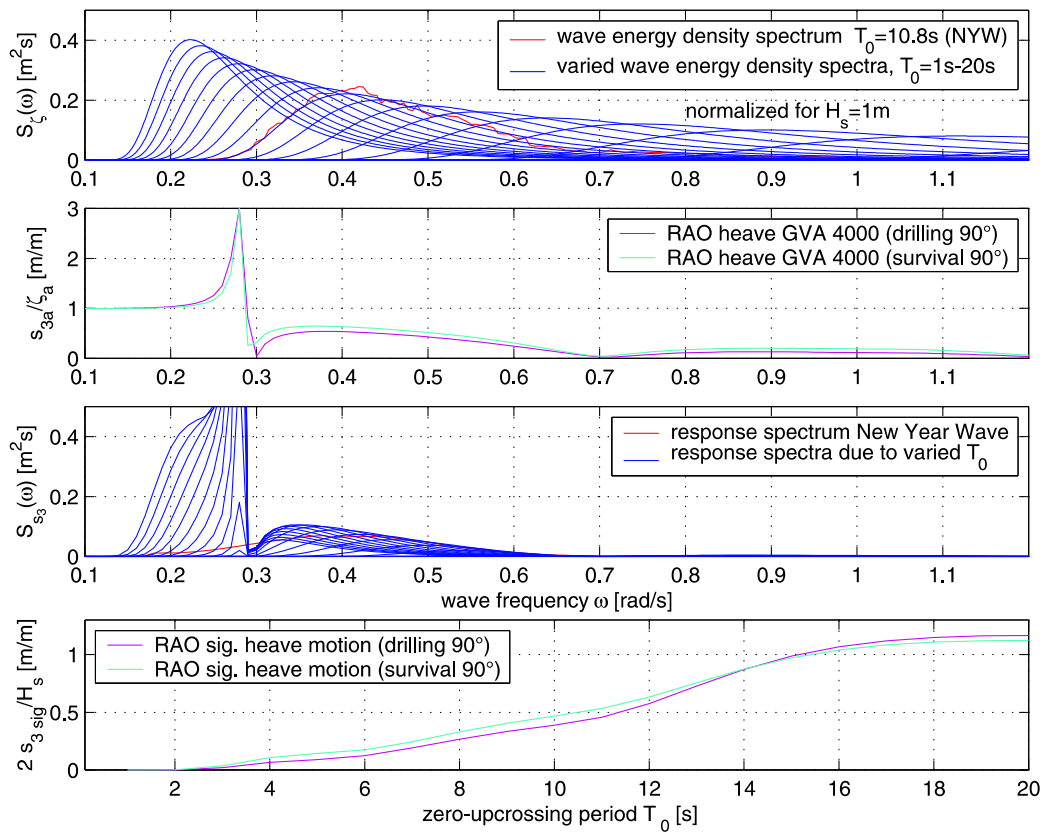


Figure 5.6: Frequency-domain analysis of the heave motion of the semisubmersible *GVA 4000*: Sea spectra – response amplitude operators – response spectra – significant heave double amplitudes. The significant heave transfer function of the *GVA 4000* is very similar to the significant heave transfer function of the FPSO and crane vessel.

In Fig. 5.6, the analysis of the heave motion of the semisubmersible is given. For larger wave periods, the significant amplitudes are increasing. This is not surprising, as for sea states with zero-upcrossing periods larger than 10 s, wave energy is also found in the range of the heave resonance. In these sea states, the magnitude of the significant double amplitudes is therefore strongly dependent on the maximum of the heave transfer function. The significant heave transfer function of the semisubmersible is similar to the significant heave transfer function of the FPSO and the crane vessel (see Figs. 4.4 and 4.16), although the heave transfer function of the ship type structures have no pronounced resonance peak.

The analysis of the airgap by statistical means is shown in Fig. 5.7. Surprisingly, in contrast to the heave motion analysis, the transfer function of the

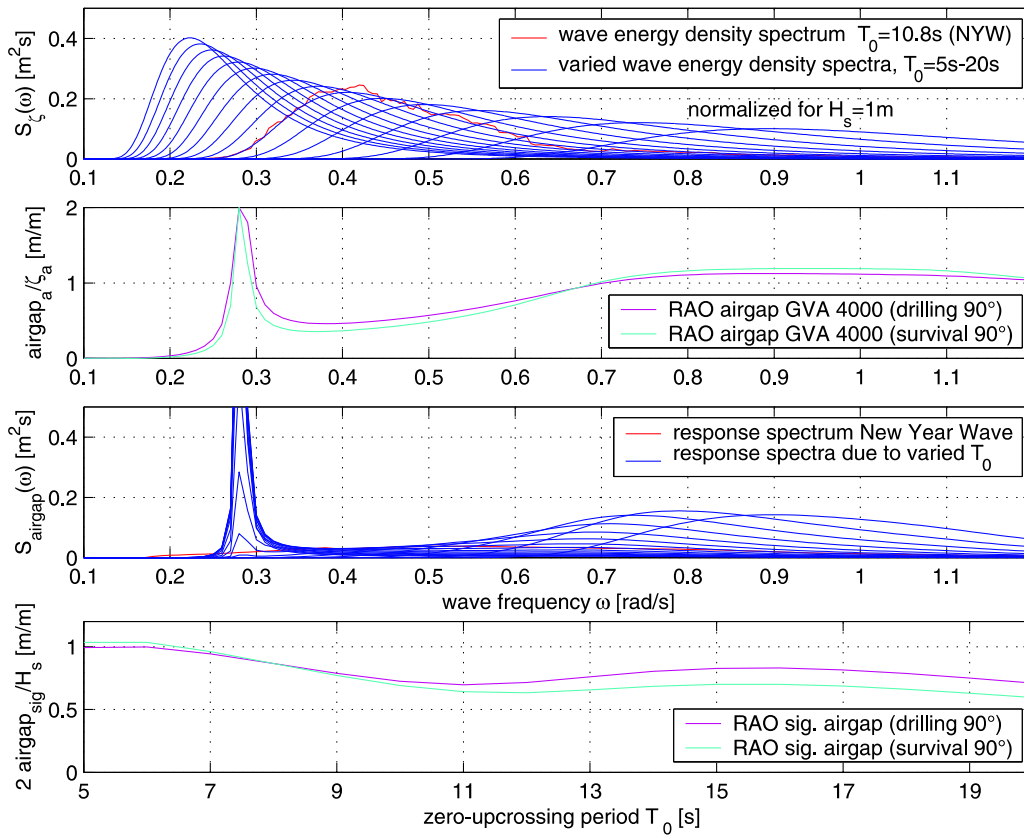


Figure 5.7: Frequency-domain analysis of the airgap of the semisubmersible *GVA 4000*: Sea spectra – transfer function for operation and survival draft – response spectra – significant airgap double amplitudes. The significant responses are relatively insensitive to the zero-upcrossing period of the sea state.

significant double amplitudes of the variation in airgap is relatively insensitive to the zero-upcrossing period of the sea state.

So far, the traditional statistical analysis in this thesis is based on the Pierson-Moskowitz spectrum, which describes a fully developed wind sea. In such sea conditions, Rogue Waves can occur as the example of the *New Year Wave* proves. For comparison, the airgap of the *GVA 4000* is statistically analyzed based on the JONSWAP spectrum with a peak enhancement factor of $\gamma = 3.3$ as presented in Fig. 5.8. The JONSWAP sea spectra (top diagram) are also normalized for $H_s = 1$ m and multiplied with the squared transfer function of the airgap. From the area under the response spectra the significant amplitudes are derived (bottom diagram). In comparison to the analysis

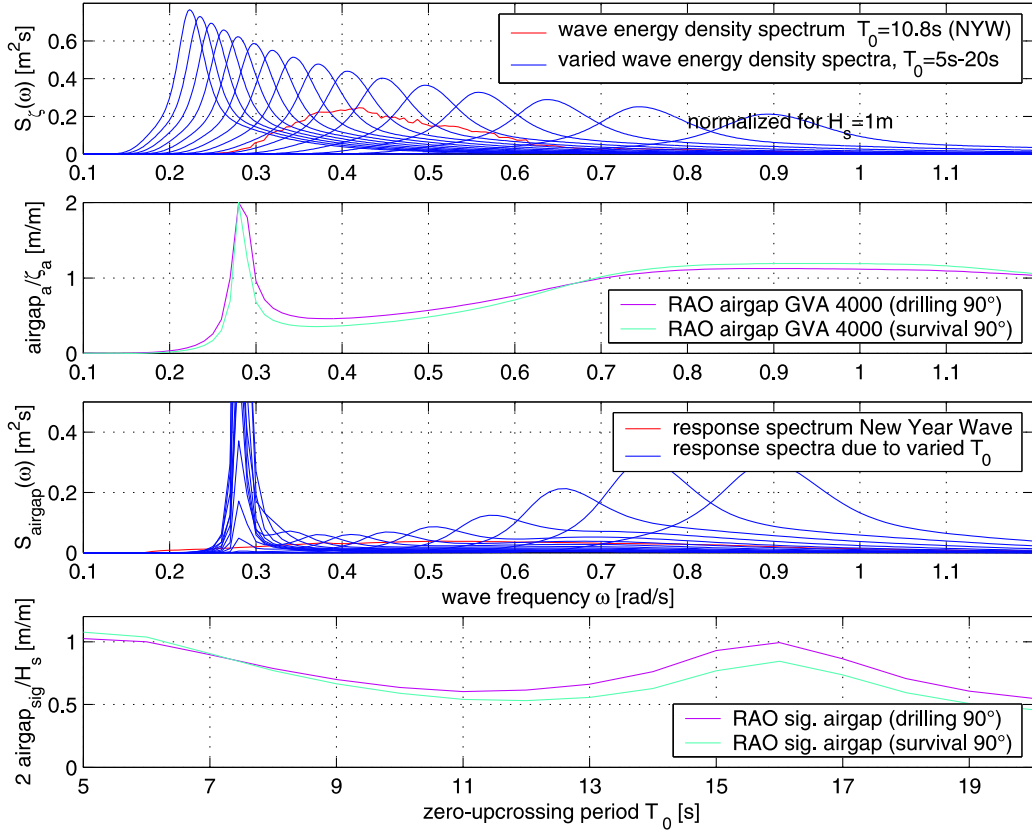


Figure 5.8: Frequency-domain analysis of airgap of semisubmersible *GVA 4000* applying the JONSWAP spectrum with $\gamma = 3.3$: Sea spectra – response amplitude operators – response spectra – significant airgap double amplitudes. The statistical analysis based on the JONSWAP spectrum gives smaller significant amplitudes for the airgap in the range of 9 s – 14 s, but larger responses below and above this frequency range.

based on Pierson-Moskowitz spectra, the JONSWAP spectra induces more pronounced peaks into the transfer function of the significant airgap as the JONSWAP spectra are more narrow banded. For the sea states investigated in this work, with T_0 in the frequency range 9 s – 11 s, the analysis based on JONSWAP spectra results in smaller significant amplitudes. Nevertheless, due to the smaller band width, larger responses are obtained if the period of the JONSWAP spectrum coincides with the maximum of the transfer function. Thus, the choice of the spectrum influences the resultant motion and forces.

5.4 Time-domain investigation of the semi-submersible encountering the *New Year Wave*

In normal sea states with no local exotic Freak Waves, frequency-domain results are satisfactory, and the seakeeping behavior is easily determined by standard evaluation methods. However, in extreme wave conditions it may be advisable to focus on local wave phenomena and analyze whether maximum motions or forces are underestimated by frequency-domain methods.

Fig. 5.9 gives the time registrations of the modelled *New Year Wave* and the corresponding splitting forces, heave motions and airgap, both from model tests and simulations by WAMIT. The draft is adjusted to 20.5 m resulting in a still water airgap of 20.5 m. The time traces are calculated by complex multiplication of the Fourier transform of the exciting wave sequence by the corresponding transfer function and subsequent inverse Fourier transformation. Thus, the phase information of the incoming wave field is preserved. The results of numerical simulation and experiment correspond quite well. Negative values – tension – of the splitting forces denote forces acting in opposing directions, trying to tear the semisubmersible apart, whereas positive values – compression – denote forces squeezing the hulls together.

Tab. 5.1 summarizes the results from the stochastic analysis based on Pierson-Moskowitz spectra with a significant wave height of 11.92 m and zero-up-crossing period of 10.8 s. Maximum significant responses are derived by the relation $s_{sig,mas} = 1.86 \cdot s_{sig}$. For comparison, maximum registered responses from model tests are also listed. The last column in Tab. 5.1 gives the ratio of maximum recorded response to maximum significant amplitude. Splitting forces observed due to the *New Year Wave* are 25% larger than estimated by statics, whereas the heave motion is well below (71%). The decrease in airgap recorded (-12.31 m) is 59% larger than could be expected from statistical analysis (7.76 m). Summarizing, the traditional frequency approach estimates the heave motion well, i. e. the estimation is on the safe side. However, the splitting forces and the reduction of the airgap due to the *New Year Wave* are substantially underestimated.

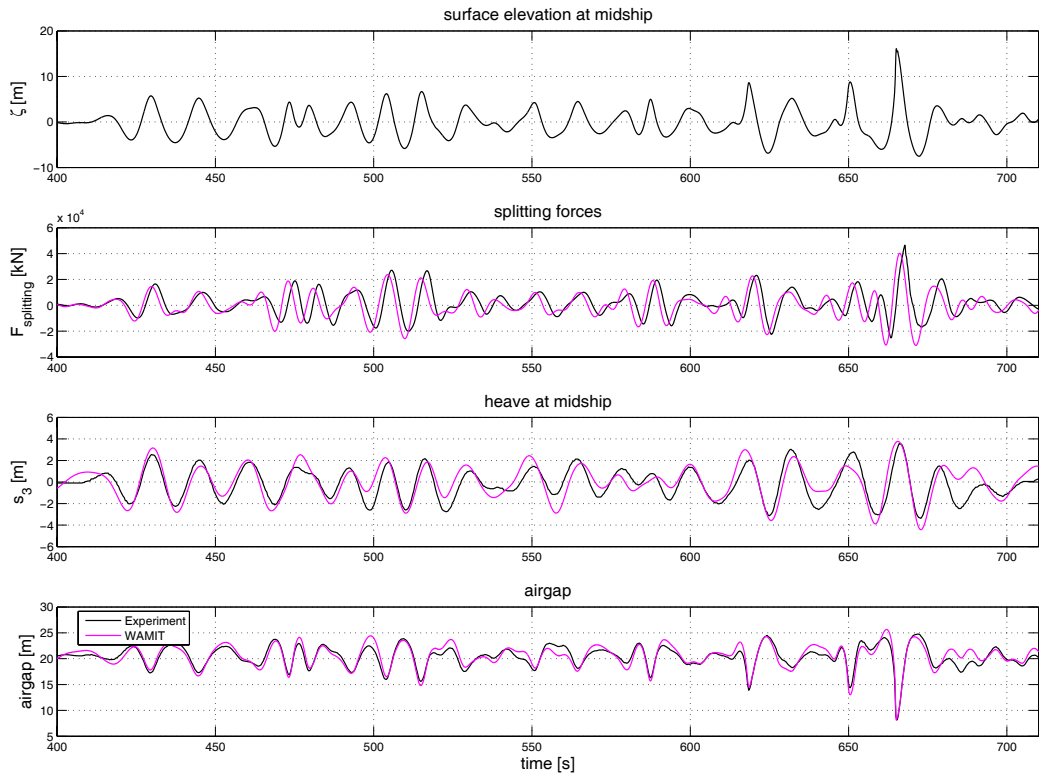


Figure 5.9: Comparison of model test data and calculated splitting forces, heave motions and airgap of the semisubmersible *GVA 4000* in the *New Year Wave*. Fortunately, the airgap remains positive when the Rogue Wave passes beneath the main deck.

Responses of the semisubmersible <i>GVA 4000</i> due to the <i>New Year Wave</i>					
	$s_{exp,max}$	$s_{exp,min}$	s_{sig}	$s_{sig,max}$	$ s_{exp} _{max}/s_{sig,max}$
splitting [10^4 kN]	4.57	-2.61	1.96	3.65	1.25
heave [m]	3.62	-3.32	2.74	5.10	0.71
airgap [m]	4.32	-12.31	4.17	7.76	1.59

Table 5.1: Splitting forces, heave motions and airgap of the *GVA 4000* due to the *New Year Wave* comparing results from statistics and model tests: Measured maximum and minimum responses $s_{exp,max}$, $s_{exp,min}$, significant amplitudes s_{sig} , maximum significant amplitudes $s_{sig,max}$, and ratio of maximum measured response to maximum significant response $|s_{exp}|_{max}/s_{sig,max}$. The decrease in airgap and the resultant splitting forces are clearly underestimated by statistics.

5.5 Time-domain investigation of the GVA 4000 encountering Rogue Waves integrated in storm seas

In chapter 4, the bending moments of the FPSO and the crane vessel are investigated with the conclusion that the significant maximum values estimated by statistics are clearly exceeded if a Rogue Wave is encountered. Therefore, the GVA 4000 is exposed to exactly the same sea conditions. This is possible, as all three models are built according to the same scale and as the test conditions are reproducible due to a computer controlled wave generator.

Fig. 5.10 gives the time traces of the measured wave sequence from the *experimental optimization* approach (compare Figs. 4.9 and 4.20 for the responses of the FPSO and the crane vessel) and the associated splitting forces, heave motions as well as the resultant airgap. For the model tests, the draft is adjusted to survival conditions, which means the draft is 16.2 m and the still water airgap is 24.8 m.

In Tab. 5.2 maximum responses observed in the model tests are compared to the significant values from statistics. The statistical approach covers well the splitting forces and the variation in airgap, whereas the maximum heave is underestimated by 33%. This is surprising, as in the case of the *New Year Wave*, heave is well covered by the statistics, but splitting forces and airgap are under predicted. This emphasizes, that the local characteristics of the encountered Rogue Wave is of great importance, and the statistical parameters, significant wave height and period are not sufficient to determine extreme responses.

In a next step, the splitting forces, airgap and heave motion of the semi-submersible are investigated in four storm seas with integrated Rogue Waves generated by the *linear optimization* scheme from chapter 2. In Figs. 5.11 and 5.12, the semisubmersible is exposed to storm seas A and B with $T_p = 15$ s and $H_s = 13$ m. From the significant transfer function of the splitting forces (Fig. 5.5) it can be seen, that the significant splitting forces are smaller in sea conditions with larger periods. Nevertheless, for storm sea B ($H_{max}/H_s = 2.50$) values from the statistical analysis are exceeded by 10%.

Figs. 5.13 and 5.14 present the time traces for semisubmersible encountering storm seas C and D with $T_p = 14$ s and $H_s = 12$ m. The extreme large Rogue Wave of storm sea D, with $H_{max} = 32.15$ m and $H_{max}/H_s = 2.68$, causes

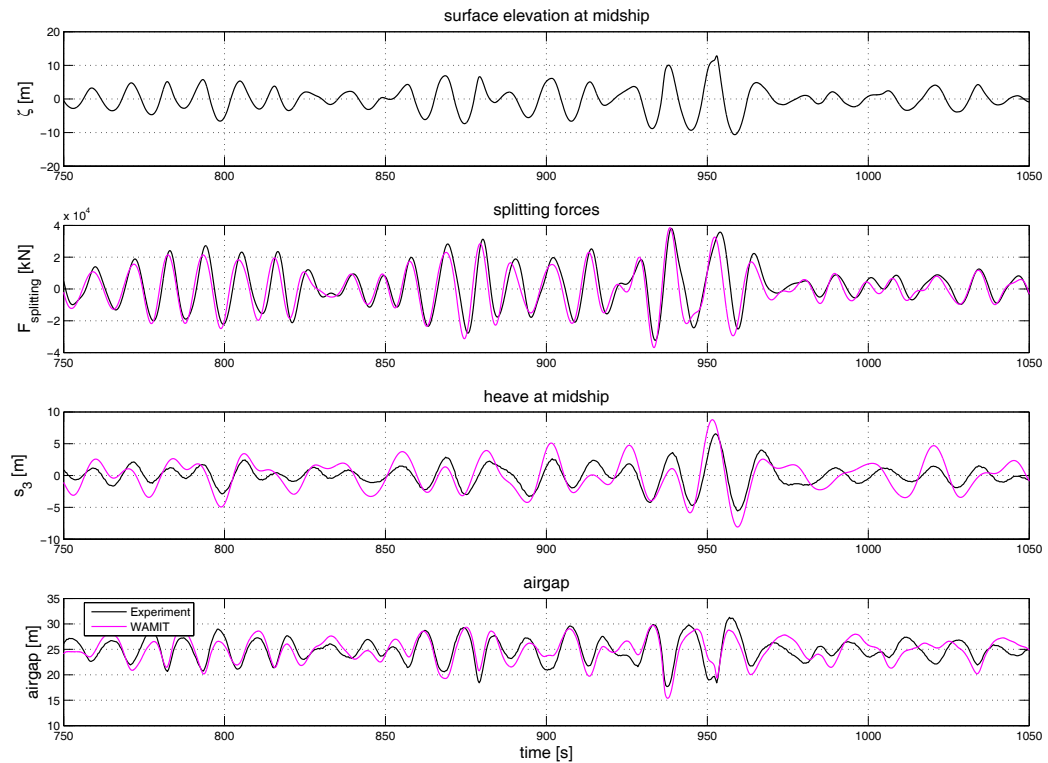


Figure 5.10: Semisubmersible *GVA 4000* in storm sea with embedded Rogue Wave generated by the *experimental optimization* approach as proposed in chapter 2, $H_{max}/H_s = 2$, $H_s = 13$ m, $T_p = 13$ s, $\gamma = 1$. The splitting forces of the semisubmersible are of impressive dimensions of $4.57 \cdot 10^4$ kNm, which equals the gravitational force corresponding to a mass of 4570 t. Without cross bracings taking up these enormous forces, the resultant moments would be cracking the column deck joint.

splitting forces that are 28% larger than expected from statistical analysis, pointing out that the statistical approach does not cover Rogue Wave impacts in either case.

In Tab. 5.3, maximum measured splitting forces are compared to the significant (maximum) values. The extreme large wave of storm sea D causes the largest forces resulting in the largest underestimation by statistical methods. That the highest wave is not always the worst can be concluded from Tab.5.4: For the heave motion, largest deviations between model test data and statistics are observed for storm sea C. Unsettling results for the airgap are presented in Tab. 5.5: The decrease in airgap in all four investigated Rogue Wave sequences is underestimated. For sea state B, the reduction in

Responses of GVA 4000 due to experimentally optimized Rogue Wave					
	$s_{exp,max}$	$s_{exp,min}$	s_{sig}	$s_{sig,max}$	$ s_{exp} _{max}/s_{sig,max}$
splitting [10^4 kN]	4.65	-3.23	2.93	5.44	0.85
heave [m]	6.58	-5.57	2.67	4.96	1.33
airgap [m]	6.52	-7.10	5.01	9.31	0.70

Table 5.2: Splitting forces, heave motions and airgap of the GVA 4000 in the Rogue Wave sequence from the *experimental optimization* approach, $H_s = 13$ m, $T_p = 13$ s, for survival conditions, 16.2 m draft, comparing statistical and experimental values: Measured maximum and minimum responses $s_{exp,max}$, $s_{exp,min}$, significant amplitudes s_{sig} , maximum significant amplitudes $s_{sig,max}$, and ratio of maximum measured response to maximum significant response $|s_{exp}|_{max}/s_{sig,max}$. With respect to the splitting forces, this Rogue Wave sequence appears to be rather moderate. Note, that this Rogue Wave sequence causes bending moments of the FPSO 83% larger than estimated by statistics.

airgap (-15.61 m) is nearly twice the predicted one (-7.70 m). Fortunately, the airgap is still 9.19 m, confirming that in harsh seas the semisubmersible is forced to follow wave motions due to viscous effects.

The overall agreement between numerical results based on WAMIT and experimental data is convincing, although differences, in particular for the motion calculations, are noticeable. The differences can be mainly attributed to the fact, that the semisubmersible surges due to a soft mooring modeled by springs. These drift motions cause the GVA 4000 to encounter the Rogue Waves at a slightly different position and instance compared to the numerical simulations. In addition, for the numerical simulation, small motions of the semisubmersible are assumed. Since, pitch angles of up to 8° were observed during the model tests, this presumption may be violated. Furthermore, in the numerical simulations, second order effects originating from the mooring, and nonlinear loads caused by wave breaking and wave run up at the columns are not included. This influences the pitch motion as well as the heave motion as the semisubmersible has a small water plane area and therefore small hydrostatic restoring forces. For the future fast numerical codes considering some of these effects are desirable.

The large pitch motion observed during the experiments of up to 8° result in a reduction of the airgap of up to 4 m in the corners of the semisubmersible (breadth of main deck 57.72 m). The minimum airgap measured is 10 m (see Fig. 5.14). Therefore, no direct wave impact on the main deck occurs.

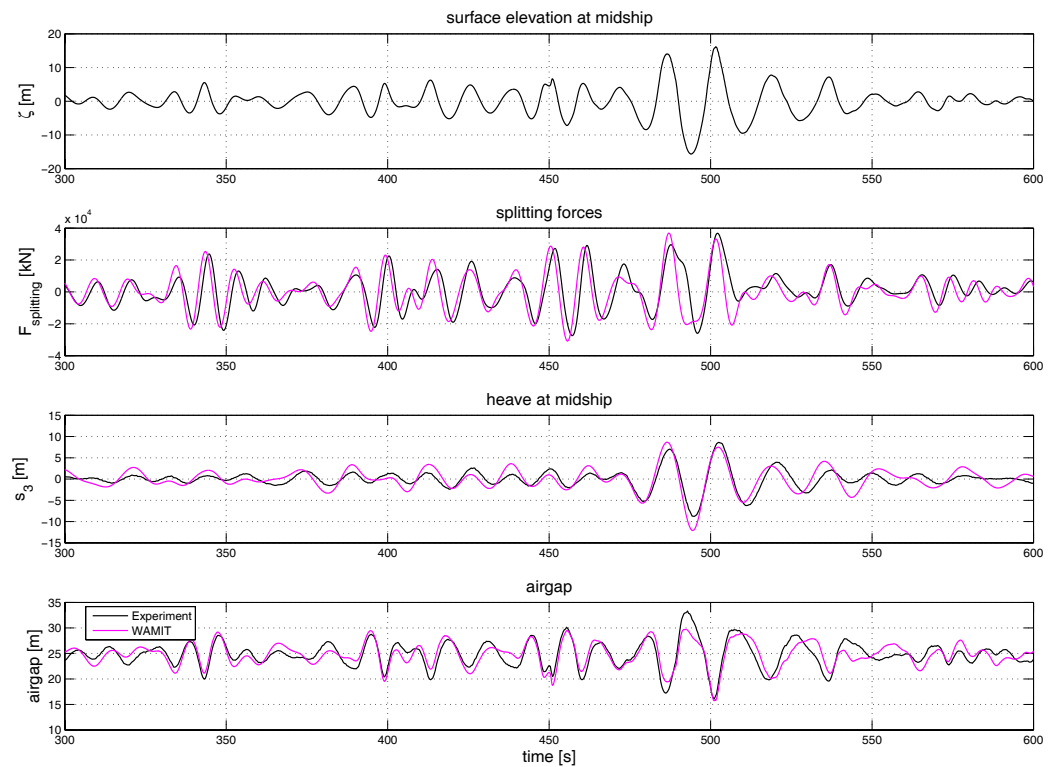


Figure 5.11: Responses of the semisubmersible *GVA 4000* due to storm scenario A generated by the *linear optimization* approach: $T_p = 15$ s, $H_s = 13$ m, $H_{max} = 31.85$ m and $H_{max}/H_s = 2.45$. Although this wave sequence causes very large bending moments of the FPSO and the crane vessel, the splitting forces of the semisubmersible are small and well covered by statistics.

Nevertheless, wave run up is quite dramatic at the columns when a Rogue Wave is encountered, causing significant structural loads to the underside of the main deck.

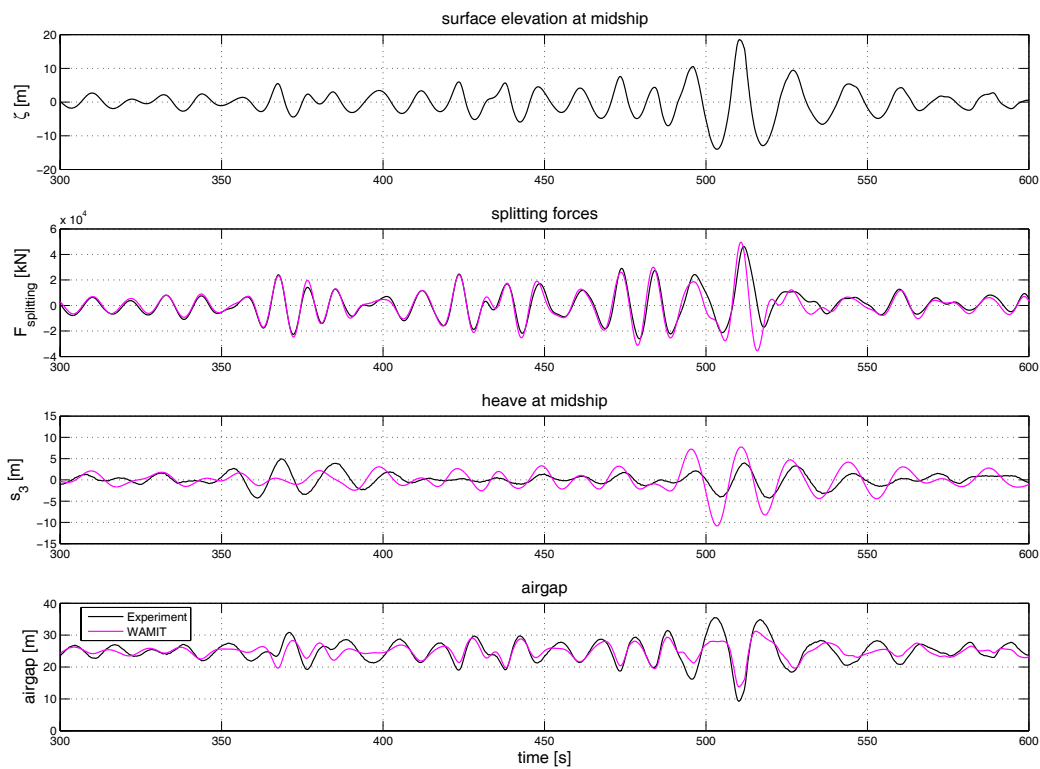


Figure 5.12: Responses of the semisubmersible *GVA 4000* due to storm scenario B: $T_p = 15$ s, $H_s = 13$ m, $H_{max} = 32.56$ m and $H_{max}/H_s = 2.50$. This wave scenario gives the maximum decrease in airgap of -15.61 m. Nevertheless, the airgap remains still sufficient with 9.19 m.

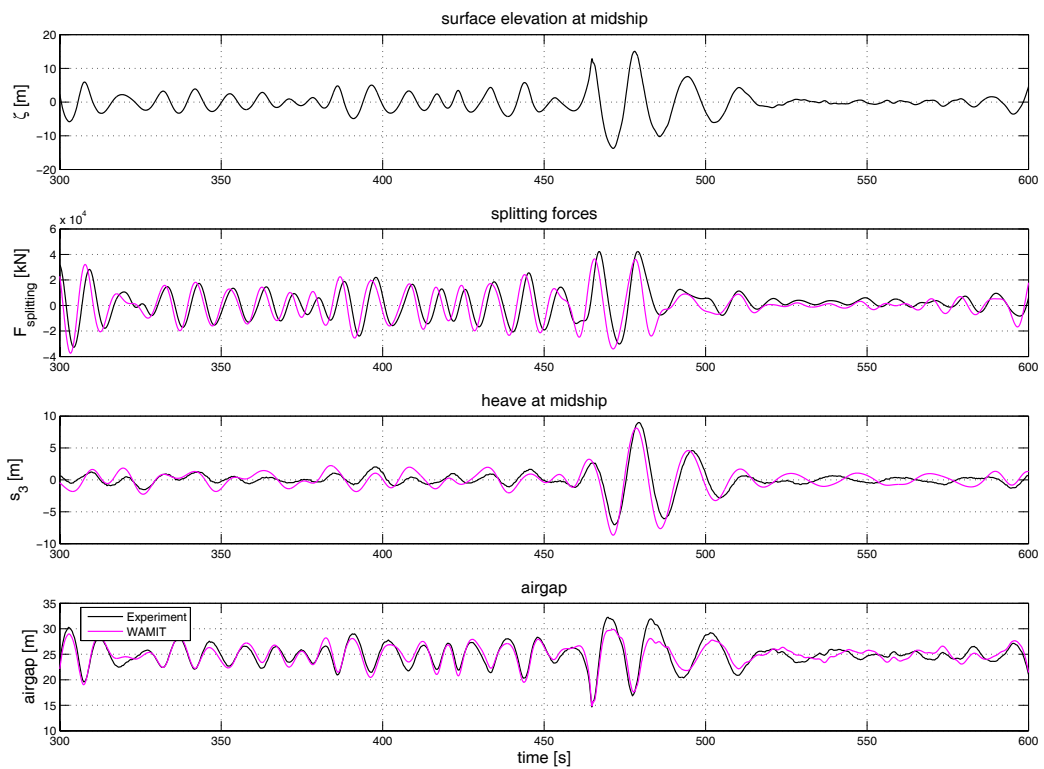


Figure 5.13: Responses of the semisubmersible *GVA 4000* due to storm scenario C: $T_p = 14$ s, $H_s = 12$ m, $H_{max} = 28.83$ m and $H_{max}/H_s = 2.40$. The wave sequence with the smallest ratio of H_{max}/H_s gives the largest heave motion. This phenomena is also observed for the FPSO and the crane vessel.

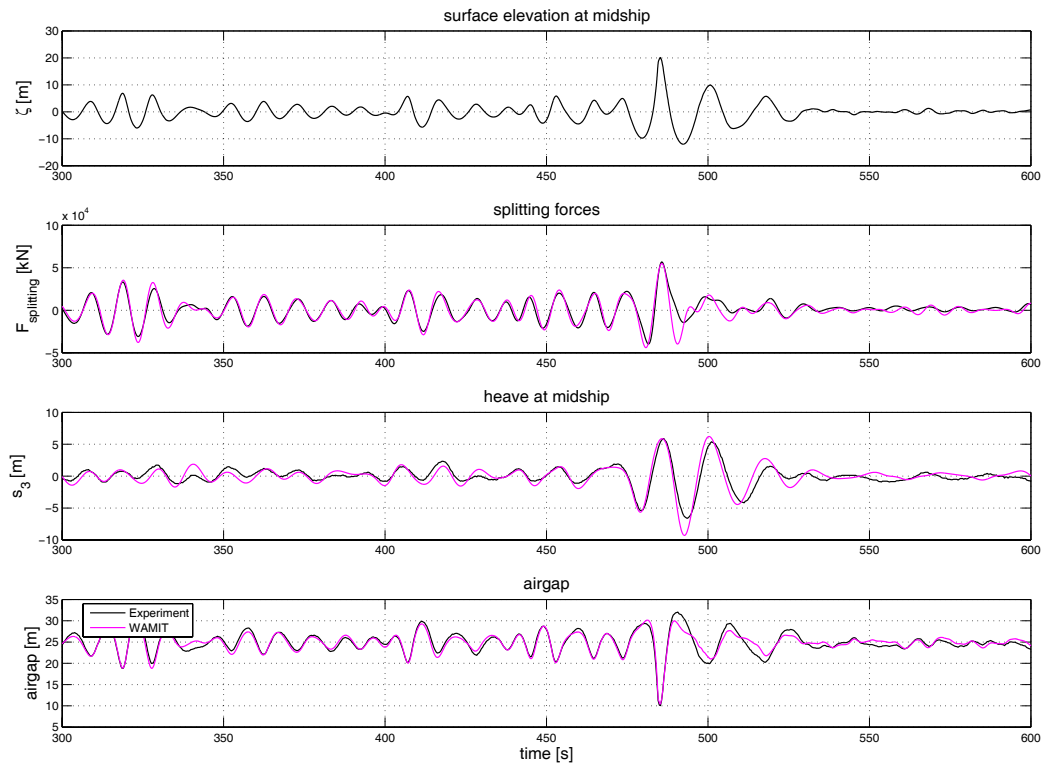


Figure 5.14: Responses of the semisubmersible *GVA 4000* due to storm scenario D: $T_p = 14$ s, $H_s = 12$ m, $H_{max} = 32.15$ m and $H_{max}/H_s = 2.68$. The largest splitting forces are caused by the extremely high Rogue Wave.

Splitting forces of the semisubmersible <i>GVA 4000</i>							
Sea state		Experiment		Statistics			
	H_{max}/H_s	H_{max}	$F_{comp.}$	$F_{tension}$	F_{sig}	$F_{sig,max}$	$ F_{exp} _{max}/F_{sig,max}$
	[-]	[m]	[10 ⁴ kN]	[10 ⁴ kN]	[10 ⁴ kN]	[10 ⁴ kN]	[-]
(A)	2.45	31.85	3.72	-3.45	2.26	4.21	0.88
(B)	2.50	32.65	4.62	-3.04	2.26	4.21	1.10
(C)	2.40	28.83	4.38	-3.28	2.38	4.43	0.99
(D)	2.68	32.15	5.68	-3.97	2.38	4.43	1.28

Table 5.3: Splitting forces of the *GVA 4000* due to storm seas: Sea state parameters, maximum splitting forces from model tests (compression and tension), significant splitting force amplitude F_{sig} , maximum splitting force amplitude $F_{sig,max} = 1.86 \cdot F_{sig}$, and ratio of maximum measured splitting force to maximum significant splitting force amplitude $|F_{exp}|_{max}/F_{sig,max}$. In comparison to the findings of the analysis of the bending moments of the FPSO, the deviations found between statistical values and experimental data for the splitting forces are rather small, i. e. an underestimation of maximal 28%.

Heave motions of the semisubmersible <i>GVA 4000</i>							
Sea state		Experiment		Statistics			
	H_{max}/H_s	H_{max}	$s_{3,exp,max}$	$s_{3,exp,min}$	$s_{3,sig}$	$s_{3,sig,max}$	$ s_{3,exp} _{max}/s_{3,sig,max}$
	[-]	[m]	[m]	[m]	[m]	[m]	[-]
(A)	2.45	31.85	8.63	-8.76	3.45	6.41	1.37
(B)	2.50	32.65	4.86	-4.34	3.45	6.41	0.76
(C)	2.40	28.83	8.97	-7.03	2.82	5.25	1.71
(D)	2.68	32.15	5.89	-6.63	2.82	5.25	1.26

Table 5.4: Heave motion of the *GVA 4000* due to storm seas: Sea state parameters, maximum measured heave motion (up $s_{3,exp,max}$ and down $s_{3,exp,min}$), significant heave amplitude $s_{3,sig}$, maximum heave amplitude $s_{3,sig,max} = 1.86 \cdot s_{3,sig}$, and ratio of maximum measured heave amplitude to maximum significant heave amplitude $|s_{3,exp}|_{max}/s_{3,sig,max}$. The semisubmersible shows a nonlinear system behavior, thus, heave responses cannot be directly related to the wave height or the ratio of H_{max}/H_s .

Airgap of the semisubmersible <i>GVA 4000</i>							
Sea state		Experiment		Statistics			
	H_{max}/H_s	H_{max}	$s_{7,exp,max}$	$s_{7,exp,min}$	$s_{7,sig}$	$s_{7,sig,max}$	$ s_{7,exp} _{max}/s_{7,sig,max}$
	[-]	[m]	[m]	[m]	[m]	[m]	[-]
(A)	2.45	31.85	8.52	-8.72	4.16	7.74	1.13
(B)	2.50	32.65	10.67	-15.61	4.16	7.74	2.02
(C)	2.40	28.83	7.47	-10.13	4.14	7.70	1.32
(D)	2.68	32.15	7.25	-14.76	4.14	7.70	1.92

Table 5.5: Variation in airgap of the semisubmersible due to storm seas: Sea state parameters, maximum airgap from measurement (up $s_{7,exp,max}$ and down $s_{7,exp,min}$), significant airgap amplitude $s_{7,sig}$, maximum airgap amplitude $s_{7,sig,max} = 1.86 \cdot s_{7,sig}$ and ratio of maximum measured airgap amplitude to maximum significant airgap amplitude $|s_{7,exp}|_{max}/s_{7,sig,max}$. For all four Rogue Wave scenarios, the influence of the extreme wave on the airgap is underestimated. Nevertheless, the *GVA 4000* is not in danger, since the airgap remains large enough in all Rogue Wave sequences.

5.6 Conclusions of the experimental and numerical analysis of the semisubmersible encountering Rogue Waves

In this chapter, the splitting forces, heave motions and airgap of the semisubmersible *GVA 4000* due to Rogue Wave impacts are investigated numerically and by model tests with the following findings:

- The splitting forces can be calculated by the Morison-equation, although the geometry of the semisubmersible is simplified.
- The transfer functions for the heave motion and structural loads obtained by Wamit are in good agreement with results from model tests. For the airgap, the transfer function can be derived from the heave transfer function. By the simulation of the time-domain responses based on linear transfer functions, the structure behavior due to Rogue Wave impacts can be assessed.
- Applying JONSWAP sea spectra with $\gamma = 3.3$ to the statistical analysis of the splitting forces, differences in significant responses are observed in comparison to the analysis based on Pierson-Moskowitz spectra.
- The Rogue Wave scenarios investigated – the *New Year Wave* sequence as well as wave scenarios generated by the *experimental* and by the *linear optimization* approaches – give responses for some cases exceeding clearly the estimations by statistics.
- The analysis shows, that the maximum responses are depending on the local wave pattern. Thus, only with methods which catch the responses due to the local wave characteristics, extreme values of motions and forces can be derived.

Chapter 6

Numerical Simulation of Wave Propagation

For the deterministic analysis of extreme structure behavior, the hydrodynamics of the exciting wave field, i. e. pressure, velocity and acceleration fields, are required. Responses of structures, e. g. motions, can easily be obtained by model tests, whereas the detailed characteristics of the exciting waves are often difficult to determine by measurements. Therefore, numerical wave tanks (NWT) promise to be a handy tool for providing detailed insight into wave hydrodynamics.

In this chapter, numerical wave tanks based on two different approaches are introduced and used for the simulation of Rogue Wave sequences. The wave tanks are characterized by the following key features:

- a) Potential theory with Finite Element discretization (denoted in the following as Pot/ FE)
- b) Reynolds-Averaged Navier-Stokes Equations (RANSE) using the Volume of Fluid (VOF) method for describing the free surface (denoted RANSE/ VOF).

Two different commercial RANSE codes – FLUENT and COMET – are applied to calculate wave propagation, whereas simulations based on potential theory are carried out with a wave simulation code developed at the Technical University Berlin (WAVETUB). It is shown that the potential theory method allows a fast and accurate simulation of the propagation of

nonbreaking waves. In contrast, the RANSE/ VOF method allows the calculation of breaking waves but is much more time-consuming, and the effects of numerical diffusion cannot be neglected.

To benefit from the advantages of both solvers, i. e. the calculation speed (Pot/ FE solver WAVETUB) and the capability of simulating breaking waves (RANSE/ VOF solver), the coupling of both simulation methods is introduced at a given position in the wave tank. WAVETUB is used to simulate the propagation of the wave train from the wave board towards the coupling position. Subsequently, the velocity field and the contour of the free surface are handed over as boundary to the RANSE/ VOF solver and the simulation process is continued.

To simulate wave evolution in a numerical wave tank, the elevation of the free surface has to be calculated for each time step. It can be calculated using an interface tracking method, where the computational grid is adapted to the moving free surface boundary in every time step, or using an interface capturing method, solving an additional transport equation for the deformation of the free surface. Interface capturing methods are performed on a time independent computational grid. In this work, both methods – the interface tracking method in combination with potential theory and a Finite Element approach – and the interface capturing method using RANS equations and the VOF method – are applied.

To validate these approaches, different types of model seas for the investigation of wave-structure interaction are generated in a physical wave tank and compared to the numerical simulations.

6.1 WAVETUB - Numerical wave tank based on potential theory

In WAVETUB, developed by Clauss and Steinhagen (1999), the two dimensional nonlinear free surface flow problem is solved in time domain using potential theory: The fluid is inviscid and incompressible, and the flow is irrotational. Long crested nonbreaking waves are considered. For the discretization of the fluid domain, the Finite Element Method is applied as proposed by Wu and Eatock-Taylor (1994). The atmospheric pressure above the free surface is constant and surface tension is neglected. Hence, the flow field can be described by a velocity potential which satisfies the Laplace equation. At each time step, the velocity potential is calculated in the entire fluid

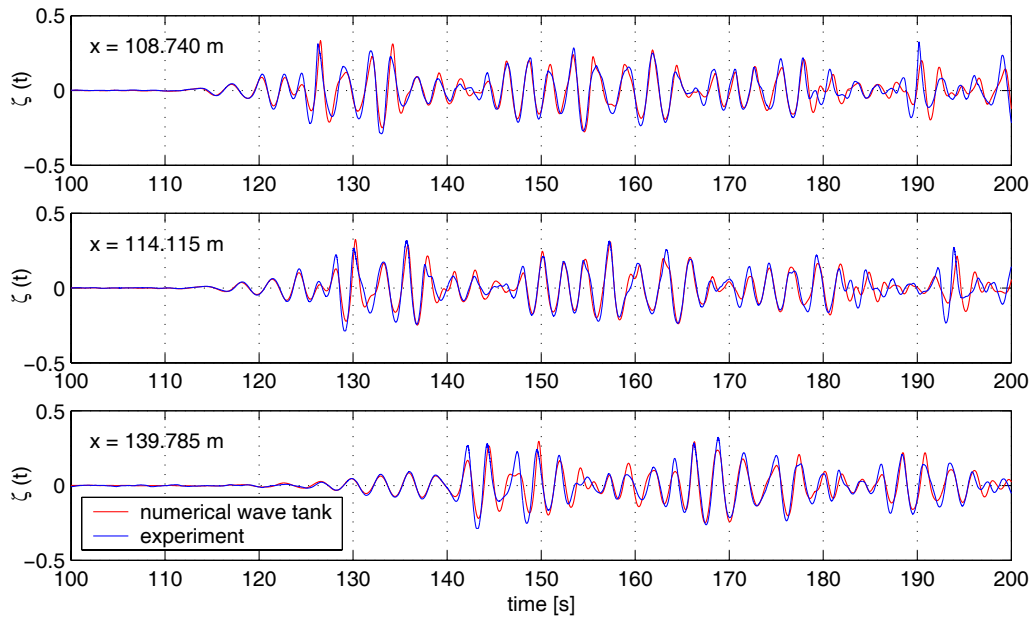


Figure 6.1: WAVETUB – Comparison of numerical (Pot/ FE) and experimental wave sequence generated by the same wave maker signal ($T_P = 14.6$ s, $H_s = 15.3$ m): registrations at different positions at the Hamburg Ship Model Basin (double flap wave generator).

domain using the finite element method. From this solution, the velocities at the free surface are determined by second-order differences.

To develop the solution in time, the fourth-order Runge-Kutta formula is applied. At each time step, a new boundary-fitted mesh is created. The procedure is repeated until the desired time step is reached, or the wave train becomes unstable and breaks. The numerical wave tank is able to simulate wave generators of types piston, single flap and double flap (and combinations of this). A complete description of this numerical wave tank can be found in Steinhagen (2001).

Fig. 6.1 presents numerical results as well as experimental data to validate this nonlinear approach at different positions in the wave tank. The storm sea realization ($T_P = 14.6$ s, $H_s = 15.3$ m) has been modelled at the Hamburg Ship Model Basin (length 300 m, width 18 m, water depth 5.6 m, double flap wave generator) at a scale of 1:34 by the nonlinear wave generation method developed by Hennig (2005). The wave sequence has been used to investigate large roll motions and capsizing phenomena of ships (Clauss and Hennig (2003)).

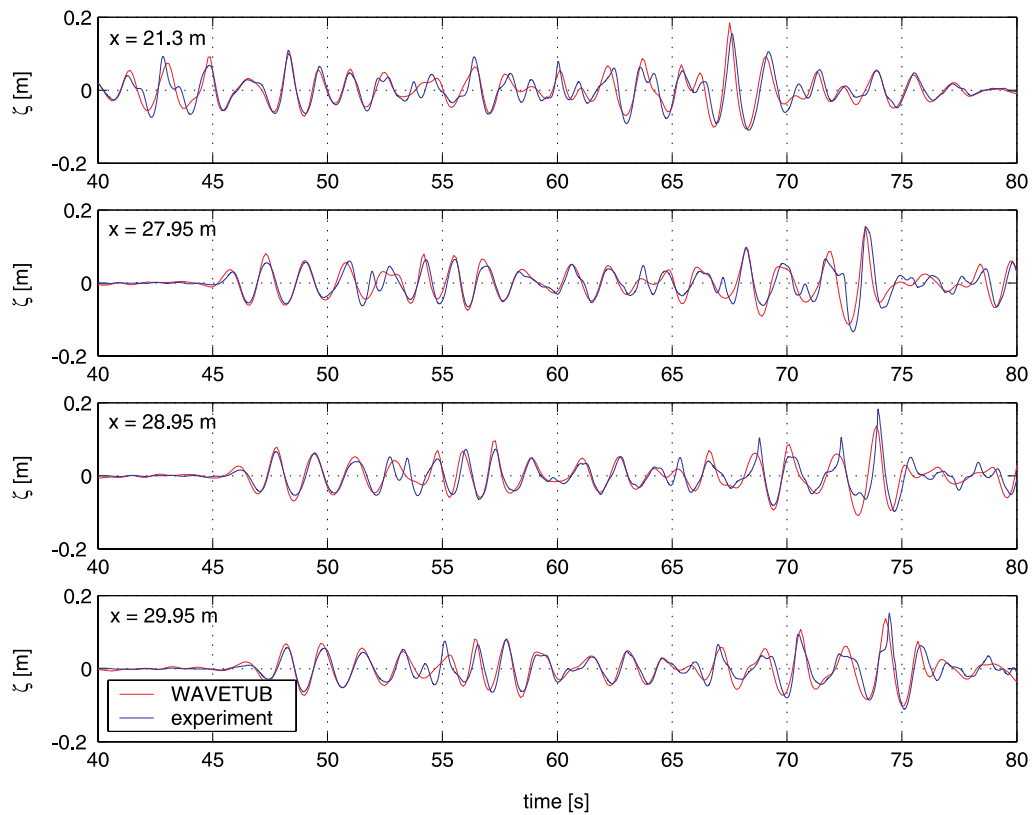


Figure 6.2: WAVETUB – *New Year Wave* – Comparison of wave tank simulation at TUB, piston type wave generator, and numerical wave tank calculation by means of Pot/ FE at scale 1:81.

Fig. 6.2 shows a simulation of the *New Year Wave*. The wave is modelled in the large wave tank at TUB at scale 1:81 (water depth 1.5 m, piston type wave generator). The figure shows that the result from the numerical simulation and the experiment are in good agreement at all positions.

Figs. 6.1 and 6.2 document the universality of WAVETUB for the calculation of wave propagation for different wave tanks with different water depth and types of wave generators. The numerical wave tank predicts the nonlinear evolution of wave trains and the wave-wave interaction reasonably well. As the potential field is calculated at each time step, also velocity, acceleration and pressure fields are known. Nevertheless, a drawback of this numerical wave tank based on a Finite Element Method is the inability to deal with wave breaking phenomena. If wave breaking is encountered during calculation, the simulation gets unstable and stops. To overcome these limitations a numerical wave tank using a commercial computational fluid dynamics

(CFD) solver is introduced in the next section.

6.2 Numerical wave tanks based on RANSE solvers

The following two numerical wave tanks presented here are set up using the commercial state of the art CFD solvers FLUENT and COMET. For all flows, the program systems solve the conservation equations for mass and momentum (Navier-Stokes equations). For simulating the free surface the Volume of Fluid method (VOF) is applied which allows the modelling of wave breaking phenomena. The volume elements of the fluid domain are filled with two phases: air and water. The VOF formulation relies on the fact that two or more fluids are not interpenetrating. For each phase, a new variable is introduced: the volume fraction. The sum of all volume fractions in a control volume must be unity.

6.2.1 FLUENT

In FLUENT, the tracking of the interface is accomplished by solving a continuity equation for the volume fraction (Fluent (2003)). To convert the governing equations to algebraic equations, a second order approach is used. The pressure-velocity coupling is done by the Pressure-Implicit with Splitting of Operators (PISO) scheme.

For the calculation of wave propagation as proposed here, a grid with approximately 80000 hexahedral cells is created. In order to save computational effort, the grid is adapted in the near field of the wave generator and around the free surface. The water depth for the simulation is 1.5 m, and the total height of the tank is 2.5 m. As a wall boundary condition (no-slip) is used at the end of the tank, the length of the numerical wave tank is set to 100 m in order to get enough simulation time without reflections from the end. At the end of the wave tank larger cells are generated leading to an increased numerical diffusion. Thus, the waves are damped and reflections are minimized. Alternatively, a real beach could be modelled by the RANSE solver. At the bottom of the tank and at the wave board, a wall boundary condition is applied (see also Fig. 6.3). At the top of the tank, a pressure boundary condition with atmospheric pressure is defined allowing fluid flow through the boundary.

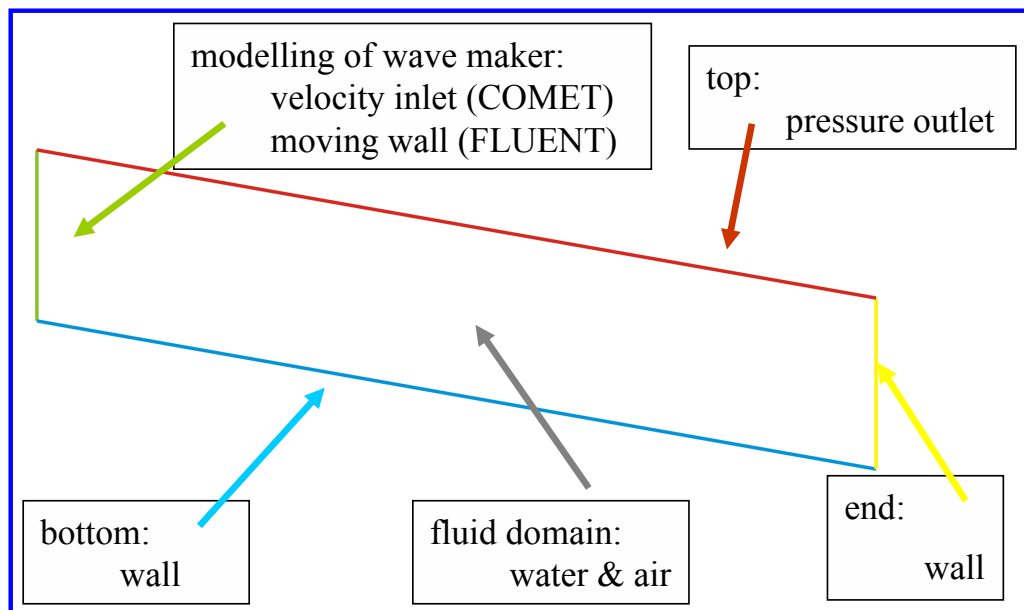


Figure 6.3: Definition of the boundary conditions for the numerical wave tanks based on FLUENT and COMET.

For simulating the wave board motion of the piston type wave generator at the large wave tank at TUB, a dynamic mesh approach (dynamic layering) is introduced. The motion of the wave board is simulated by moving the boundary forwards and backwards like the wave board in the experiment. Therefore, cells have to be added to or deleted from the fluid domain as the size of the calculation domain changes with time. The computational grid in the far field of the moving wave generator is a time independent fixed grid.

To determine the position of the moving boundary at each time step, a user defined function written in C language is implemented that provides the wave board velocity. The velocities are calculated from the measured wave board motion. As the numerical wave paddle is not an exact representation of the original wave board used in the experiments a transfer function between both systems is determined. Applying the transient wave technique (Clauss and Kühnlein (1995)) a wave packet is generated in the physical wave tank and in the simulation, and the wave elevation is recorded, calculated respectively, at the same position downstream of the wave board. Dividing the Fourier transformation of the numerical simulated wave elevations by the Fourier transformation of the measured wave elevations, the transfer function describing the different behavior of both systems is obtained. This transfer function is then used to adapt the measured wave board motion to

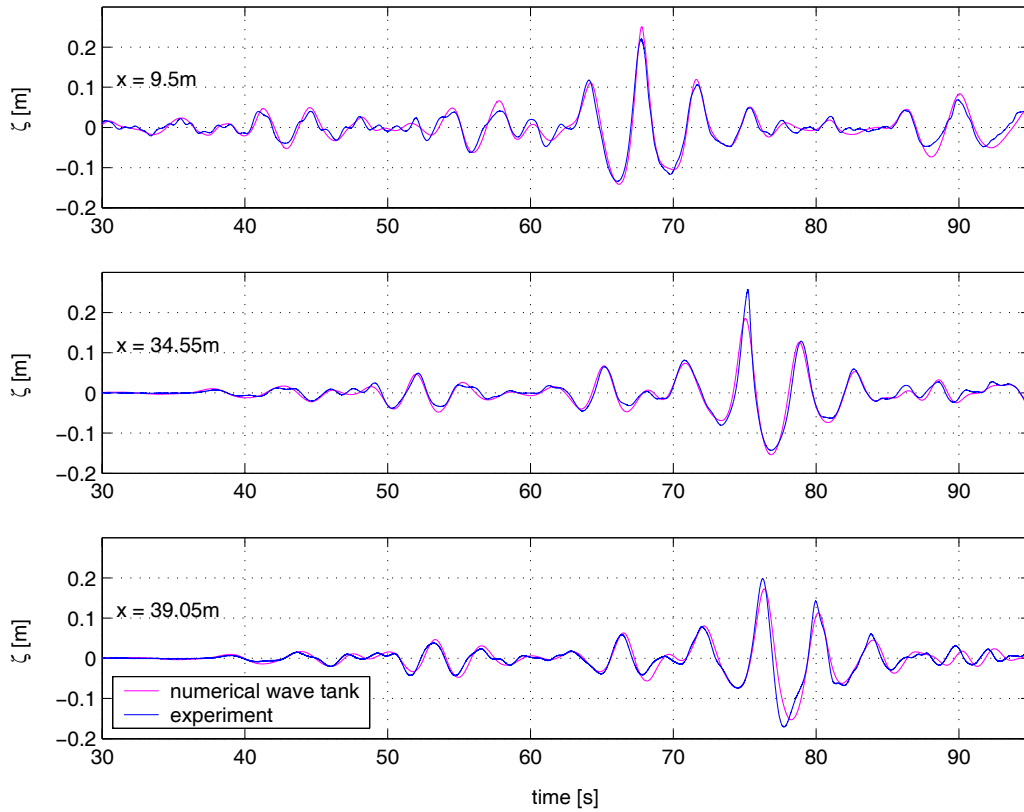


Figure 6.4: FLUENT – Numerical simulation of irregular sea based on a JONSWAP spectrum applying the RANSE/ VOF method, $T_P = 2.2$ s and $H_s = 0.1$ m, with integrated wave packet, $H_{max} = 0.35$ m, $H_{max}/H_s = 2.3$, as Three Sisters wave, at different positions in the wave tank in comparison to wave tank realization (scale 1:81).

the virtual wave tank.

As a result, Fig. 6.4 and Fig. 6.5 show the comparison between calculation and experiment of irregular seas with an integrated Rogue Wave at different positions in the large wave tank at TUB. Applying the transient wave technique, a single wave events is integrated in a random sea by superposition of a random sea state and a wave packet as presented by Hennig (2005). For the numerical simulations the time step size is set to 0.005 s. The agreement between simulation and experiment is convincing. In comparison to WAVE-TUB, numerical diffusion effects leading to decreasing wave heights at wave propagation over several wave length is noticeable.

Fig. 6.6 presents the simulation of the wave packet that is imbedded in the

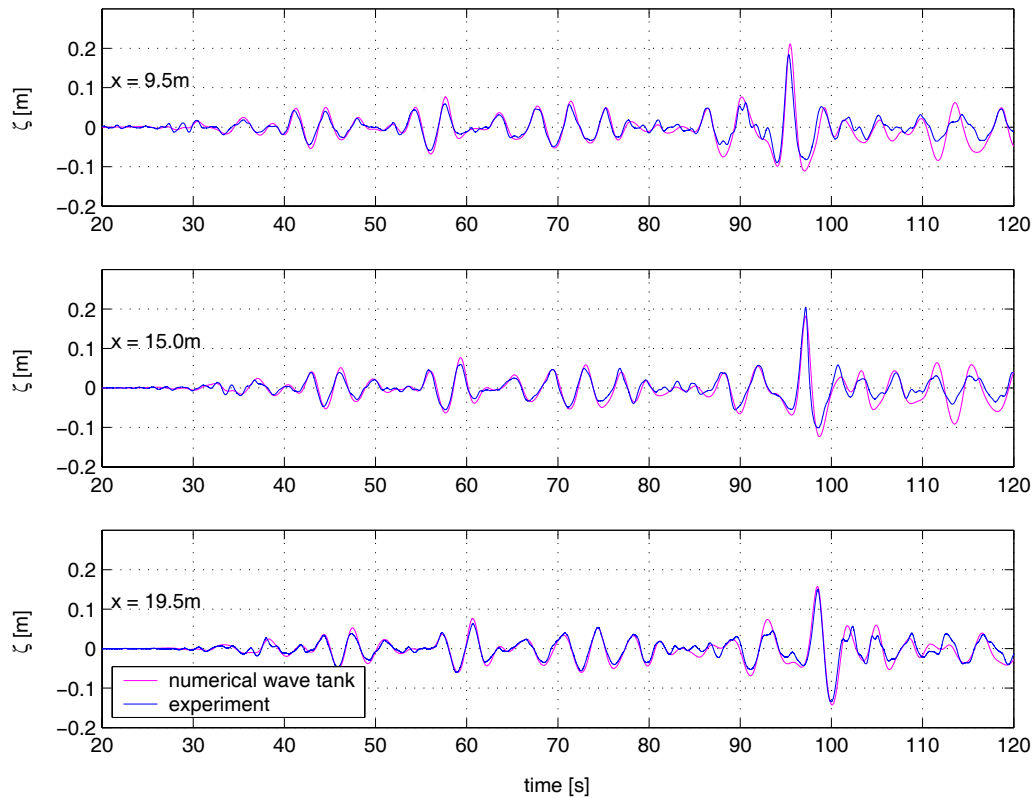


Figure 6.5: FLUENT – Numerical simulation of irregular sea based on JONSWAP spectrum, $T_P = 2.2$ s, $H_s = 0.1$ m, with integrated wave packet, $H_{max} = 0.35$ m, as Rogue Wave, at different positions in the wave tank (scale 1:81). Numerical simulation based on RANSE/VOF.

random seas as Rogue Wave presented in Fig. 6.5. The wave packet is modelled based on the same JONSWAP spectrum as used for modelling the wave environment and the concentration point is 15 m downstream from the wave board. It can easily be seen, that the phases and amplitudes are well predicted by the numerical wave tank. Wave packets can therefore be used to model high wave groups within a natural sea state or to simulate extreme waves (Kühnlein et al. (2002)).

Summarizing the results of the simulations by FLUENT, one can observe that the wave heights close to the wave generator are predicted slightly to large. At greater distances numerical diffusion is observed leading to an decreasing wave height. The introduced transfer function, describing the different system behavior of numerical and experimental wave tank, enables the calculation of wave propagation also in cases where the physical wave

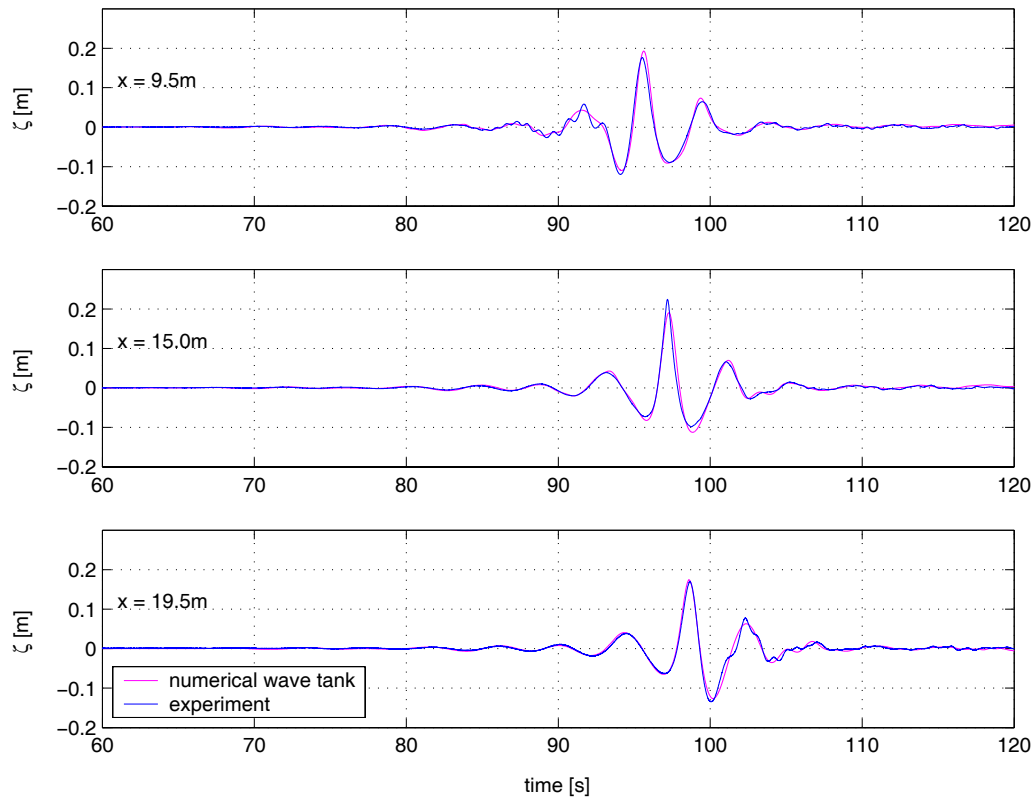


Figure 6.6: FLUENT – Numerical simulation based on RANSE/ VOF of a wave packet, with same JONSWAP spectrum as in Fig. 6.5, in comparison to wave tank realization (scale 1:81).

board can not exactly be modelled.

6.2.2 COMET

The second commercial code applied is the continuum mechanics solver COMET (ICCM (2001)). For the numerical wave tank a block structured grid is generated with 26.260 control volumes, i. e. cells near the undisturbed free surface are of dimension 31.25 mm x 6.25 mm (see Fig. 6.7). For tracking the motion of the free water surface, the High Resolution Interface Capturing scheme (HRIC) of COMET is applied, giving a sharp interface between water and air. A blending between second order central differencing and first order approximation scheme is used to calculate surface and volume integrals of the conservation equations within the first 25 m of the calculation domain. The blending allows to combine the accuracy of the second order approach with the numerical stability of the first order solution. From 25 m on, to the end of the tank, first order upwind differencing scheme is selected.

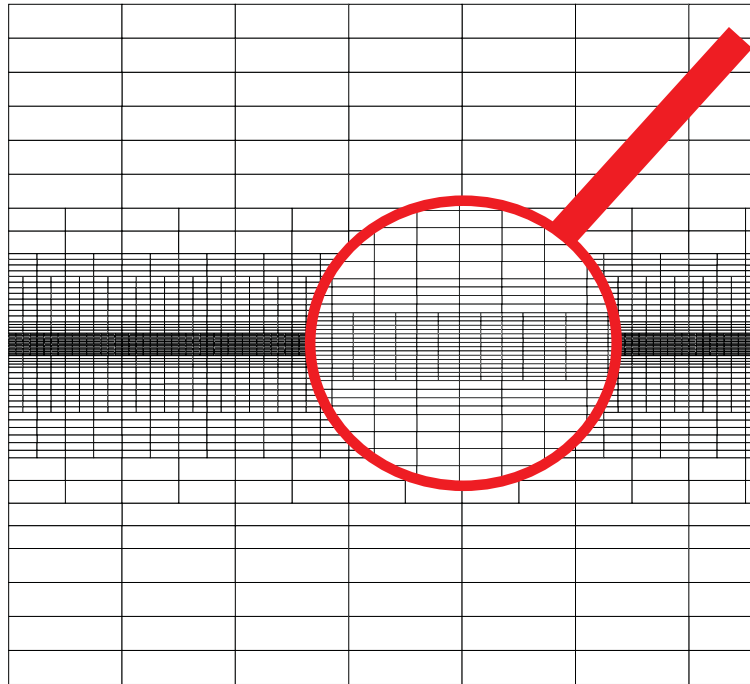


Figure 6.7: Computational block structured grid for all simulations using COMET with 26.260 control volumes. Smaller cells are generated near the free surface in order to improve the accuracy of the simulations.

The wave board is modelled by a nonstationary velocity inlet. The velocities impressed on the inlet are derived from the measured wave board motion by

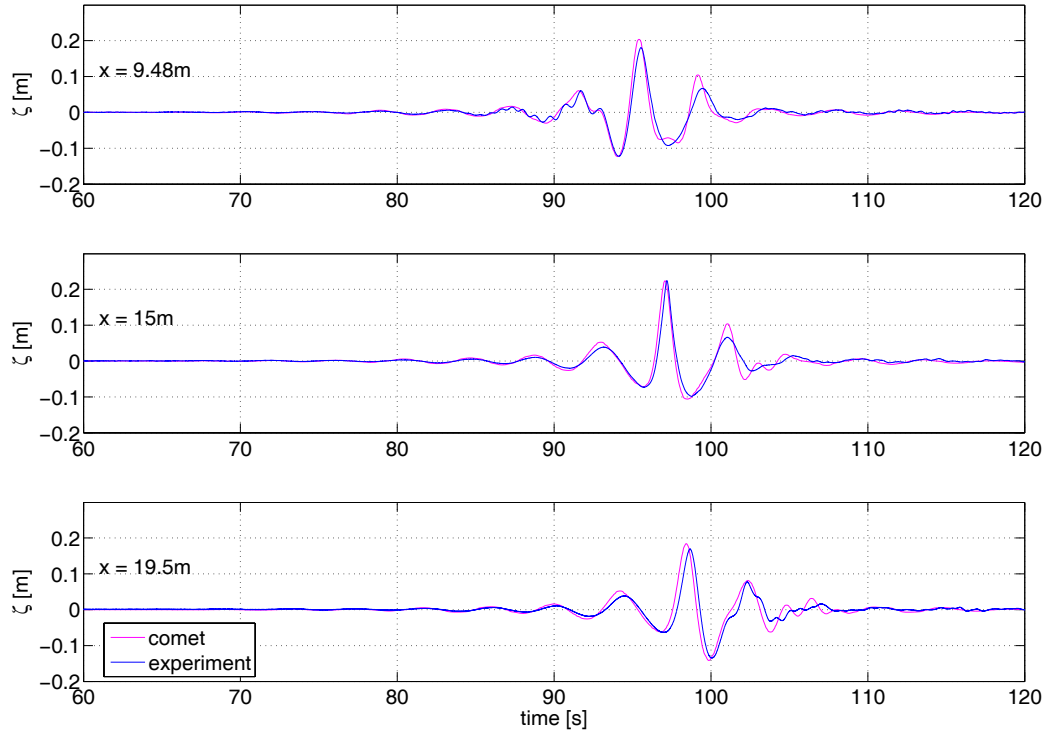


Figure 6.8: COMET – Numerical simulation of the wave packet based on JONSWAP spectrum, $T_P = 2.2$ s and $H_s = 0.1$ m, with time step size $dt = 0.005$ s, in comparison to experimental data.

differentiation. As a piston type wave generator is used for the experiments, the distribution of the velocity at the inflow is constant with depth. Also for the air above the free water surface the same inflow velocity is specified. A wave packet and the superposition of a wave packet with an irregular sea state (Clauss et al. (2004a)) are used to validate the numerical approach.

Fig. 6.8 presents the simulation of a wave packet in comparison to experimental data (large wave tank TUB). In Fig. 6.9 simulation results of an irregular sea with integrated wave packet are shown. For the simulations of the wave packet the time step size is set to 0.005 s. The calculation of the irregular sea requires smaller time steps ($dt = 0.002$ s) in order to ensure convergent results. The phases and amplitudes are well predicted by COMET in both cases, which also verifies the velocity inlet approach to model the piston type wave maker. To further improve the accuracy of the simulations, a transfer function between numerical and real wave board can be applied as it is proposed in the previous section 6.2.1 for the simulations applying FLUENT.

As a RANSE solver is used for this wave tank, the duration of the calculation

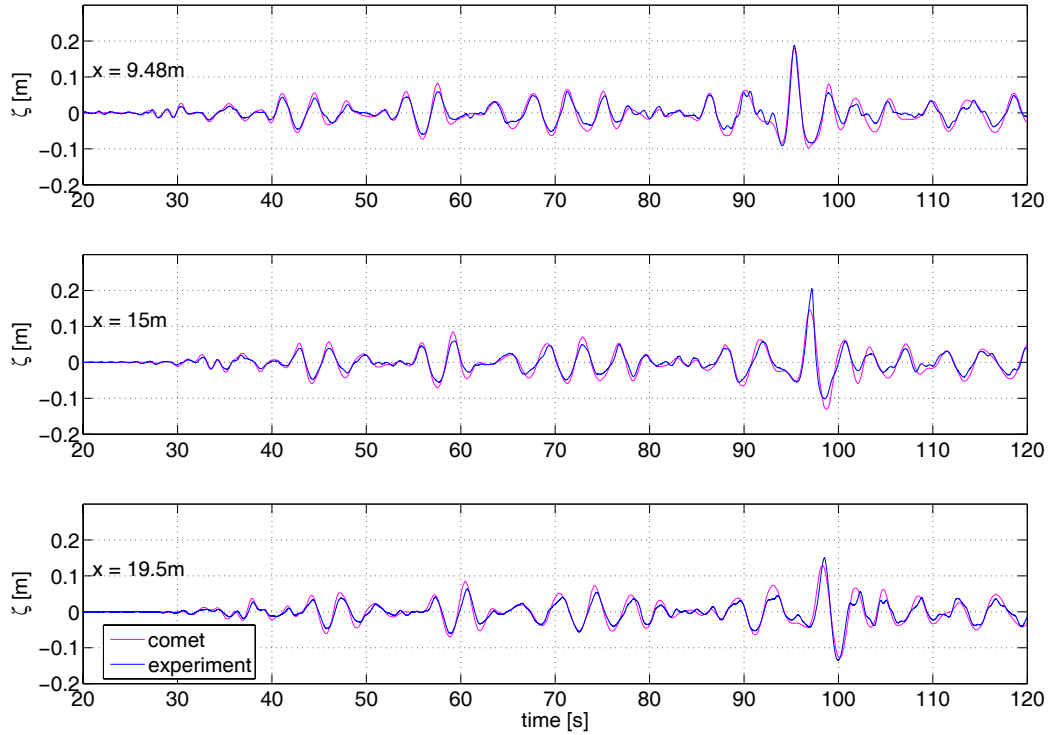


Figure 6.9: COMET – Numerical simulation of irregular sea based on JON-SWAP spectrum, $T_P = 2.2$ s, $H_s = 0.1$ m, with integrated wave packet, $H_{max} = 0.35$ m, at different positions in the wave tank. The simulation applies the RANSE/VOF method with time step size of $dt = 0.002$ s.

is significantly higher as compared to the numerical wave tank based on potential theory and FEM. To make use of the benefits of both methods, a combined approach is proposed: Potential theory is applied as long as no wave breaking occurs, and switches to the RANSE code if wave breaking is encountered. In particular, this concept is applicable for the given wave examples since Rogue Waves and wave packets are generated, which are known to focus and thus to steepen on their way towards the concentration point.

6.3 Coupling of Pot/ FE and RANSE solver

As presented in the previous sections, both, the Pot/ FE solver and the RANSE solvers are able to simulate wave propagation satisfactorily. Nevertheless, higher accuracy and faster calculations are advantages of the WAVE-

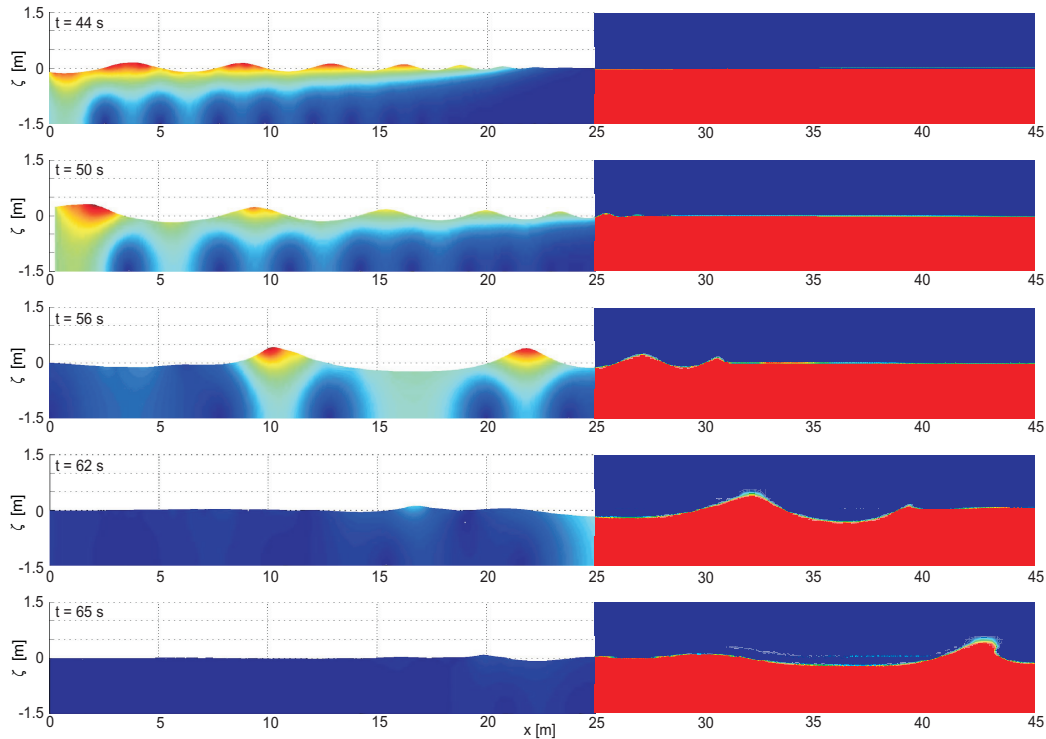


Figure 6.10: Coupling of WAVETUB and COMET at position 25 m from wave board. Showing a wave packet advancing from the Pot/ FE solver domain (left hand side) to the RANSE/ VOF solver COMET domain (right hand side) at five instants.

TUB solver. As a rule of thumb, one hour calculation time of WAVETUB equals one day of calculation time with a RANSE solver. This is due to the fact, that for qualitative similar results significant more cells are required for the RANSE simulations and the RANSE code has to solve additional equations in comparison to the Pot/ FE solver. The possibility to simulate breaking waves and to include wave-structure interaction (also in 3D) into the calculation domain are key benefits of the RANSE codes. This implies the idea of combining both approaches and profit from the advantages of both strategies.

Therefore, the RANSE solver COMET is attached to the Pot/ FE solver at a selected position, i. e. from wave board towards the coupling position, wave propagation is calculated by WAVETUB and from this position on by COMET. For the example presented, the coupling is done at a position 25 m downstream of the wave generator. The time dependent velocity profile from bottom to the actual surface elevation and the surface elevation itself are cal-

culated at position 25 m by WAVETUB. These data are used to specify the velocity and volume fraction as inflow boundary in COMET. Since different meshes – triangular cells for WAVETUB and hexahedral cells for COMET – and different sizes of time steps – 0.01 s WAVETUB and 0.002 s COMET – are used, the input data have to be interpolated accordingly. For the coupled calculation the same computational grid (see Fig. 6.7) as for the previously presented simulations by COMET is used. In Fig. 6.10 five time steps of a coupled calculation are presented. The wave packet generated at the left hand boundary (wave board) converges and gets steeper. Advancing from the potential theory domain to the RANSE domain and approaching the concentration point, the wave focuses, becomes steeper and wave crest breaking is observed, which can be handled by COMET in contrast to WAVETUB.

Using this coupling approach significant computational time is saved as RANSE methods are only used in areas where wave breaking is observed. This is of special importance if wave-structure interaction is investigated numerically as a fully developed wave field can be given to the RANSE code at a short distance upstream of the model position.

6.4 Conclusive comparison of the proposed methods for the numerical simulation of wave propagation

In this chapter, different methods for modelling nonlinear wave propagation numerically are presented:

- Numerical wave tank based on potential theory in combination with a Finite Element method – WAVETUB
- Numerical wave tanks using RANSE codes – COMET and FLUENT (moving mesh and velocity inlet as boundary conditions to simulate the wave maker)
- Combination of potential theory and RANSE codes – WAVETUB and COMET.

In general, good agreement between experiments and numerical simulations is observed. the Pot/ FE solver WAVETUB is most accurate and fast, whereas wave breaking and wave-structure interaction can be modelled by the RANSE

codes. All solvers applied tend to overpredict wave heights near the wave board. At greater distances decreasing wave heights due to numerical diffusion are noticeable in the calculation results based on RANSE/VOF.

For simulating the wave board motion within WAVETUB and FLUENT, the calculation mesh is deformed whereas for COMET an inflow boundary condition is applied. Both methods give similar results. The accuracy of the simulations can be improved by using transfer functions adapting the measured wave board motion to the virtual wave tank (Clauss et al. (2004b)).

For time discretization a first order Euler scheme is applied. COMET offers also second order approaches for unsteady calculations. For the calculation of wave propagation comparative calculation using second order time discretization reveal no further improvements of results.

The coupling of WAVETUB and RANSE solvers enables fast and accurate simulation of breaking waves and the investigation of wave-structure interaction. Nevertheless, calculation duration for the simulation of wave-structure interaction (in particular for 3D cases) are still too long for day to day application.

All numerical wave tanks are not capable to transform a given wave train backwards to the position of the wave generator. In order to generate a pre-determined wave sequence at a target location the numerical wave tank has to be combined with optimization routines (Clauss and Steinhagen (2000)). This is the reason, why for the wave generation in the wave tank the optimization approach proposed in chapter 2 is applied. However, for further detailed analysis of the exciting wave field numerical wave tanks provide unique insight into the pressure, velocity and acceleration fields, thus revealing the underlying physical mechanism of waves.

Chapter 7

Conclusions and Perspectives

This thesis is dedicated to Rogue Waves and their impact on marine structures. Rogue Waves have been feared by seafarers since centuries and have been considered as story-telling. The aim of this work is to highlight the existence of Rogue Waves and to quantify the consequences of their impacts. Therefore, method for the investigation of Rogue Wave impacts on floating structures are developed and applied.

- In chapter 1, the existence of Rogue Waves is highlighted by observations and records. The analysis of a storm recorded at *North Alwyn*, reveals that Rogue Waves are usual appearances that can be expected in a storm: Within the record of a six day storm more than 20 Rogue Waves are found. Nevertheless, current design practice often ignores the consequences of Rogue Wave impacts. Therefore, in this work, techniques to bring these Rogue Waves into the wave basin are proposed.
- In the second chapter, new methods for the realization of extreme wave sequences in a physical wave tank are introduced. The *linear optimization* approach synthesizes Rogue Waves within a random sea state based on predefined target parameters and is successfully applied to the generation of extreme wave scenarios. The *experimental optimization* scheme considers nonlinearities like wave-wave interaction and wave breaking inherently, as the Rogue Wave is optimized in the wave tank. The optimization is performed in a small wave tank and the resultant wave regime – satisfying all given target parameters precisely – is transferred to a large wave basin, thus enabling the investigation of

wave-structure interactions in deterministic sea states at a larger model scale.

- The analysis of the vertical bending moments, heave and pitch motions of an FPSO and of a crane vessel as well as the airgap and splitting forces of a semisubmersible demonstrates, that Rogue Waves can cause extreme loads and motions, often exceeding maximum values estimated by both classification rules and frequency-domain analysis. As model test conditions are reproducible, the responses of all three structures can be compared, showing that the danger of a certain wave scenario depends on the structure exposed to it. Thus, to examine if a structure is well designed for Rogue Wave impacts, model tests with deterministic wave sequences tailored particularly for the structure are carried out.
- The potential of numerical wave tanks for the nonlinear simulation of wave propagation is demonstrated in chapter 6. WAVETUB, a numerical wave tank based on potential theory and finite element discretization, provides fast and precise results. With commercial solvers like COMET and FLUENT, which are based on the Reynolds-averaged Navier-Stokes equations and the volume of fluid discretization, the inclusion of wave-structure interactions and wave breaking is possible. Therefore, a new coupling approach combining the advantages of both methods is proposed: The wave propagation is calculated with WAVETUB up to a predefined position in the wave tank where the velocity field and surface elevation is handed over to the RANSE/ VOF solver. Thus, for future investigations a powerful tool is available for the time-domain analysis of wave-structure interactions in extreme or even breaking waves.

As a consequence, Rogue Waves should be considered for the design of offshore structures since they can impose extreme loads and motions to the structure. This can be achieved, if maximum responses are determined by time-domain simulation tools or by model tests in deterministic wave groups. If the design is based on frequency-domain methods, one should bear in mind, that Rogue Waves occurrences are not covered at all times. Thus, a vessel designed according to frequency domain-methods or according to classification rules should avoid encountering a Rogue Wave. To cover all Rogue Wave scenarios generated within the scope of this work by statistics, a ratio of 4.01 between significant and maximum response would be required! Therefore, instead of the relation $s_{max} = 1.86 \cdot s_{sig}$ larger ratios should be considered for design, although structures will become more expensive. Nevertheless, it

might be cheaper to design FPSOs and other floating structures with risers and moorings that are easily detachable, thus they can leave location if an extreme storm is forecasted and avoid to be hit by a Rogue Wave.

Summarizing, the main findings of this thesis are:

- Rogue waves exist and occur regularly in storms. In consequence, during the lifetime of a structure, encountering a Rogue Wave is very probable.
- Rogue Waves impose higher loads on offshore structures than predicted by statistics and required by classification rules.
- New numerical and experimental time-domain simulation methods for the analysis of structure responses should be applied in order to include the consequences of Rogue Wave impacts into the design of offshore structures.

Bibliography

- F. Biésel and F. Suquet. Les appareils générateurs de houle en laboratoire. *La Houille Blanche*, (2):147–165, Mars-Avril 1951.
- B. Buchner and A. Voogts. Wave impacts due to steep fronted waves. In *Rogue Waves 2004*, Brest, France, 2004.
- J. R. Chaplin. On Frequency-Focusing Unidirectional Waves. *International Journal of Offshore and Polar Engineering*, 6(2):131–137, 1996.
- G. F. Clauss. Multi-scale model tests with a ring-shaped semi-submersible. In *Offshore Technology Conference*, Houston, Texas, USA, 1978. OTC 3297.
- G. F. Clauss and J. Hennig. Deterministic Analysis of Extreme Roll Motions and Subsequent Evaluation of Capsizing Risk. In *STAB 2003 - 8th International Conference on the Stability of Ships and Ocean Vehicles*, Madrid, Spain, 2003.
- G. F. Clauss, J. Hennig, and C. E. Schmittner. Modelling Extreme Wave Sequences for the Hydrodynamic Analysis of Ships and Offshore Structures. In *PRADS 2004 - 9th International Symposium on Practical Design of Ships and Other Floating Structures*, Lübeck-Travemünde, Germany, 2004a.
- G. F. Clauss, J. Hennig, C. E. Schmittner, and W. L. Kühnlein. Non-linear Calculation of Tailored Wave Trains for the Experimental Investigation of Extreme Structure Behaviour. In *OMAE 2004 - 23rd International Conference on Offshore Mechanics and Arctic Engineering*, Vancouver, Canada, 2004b. OMAE2004-51195.
- G. F. Clauss and W. L. Kühnlein. Transient wave packets – an efficient technique for seakeeping tests of self-propelled models in oblique waves. In *Third International Conference on Fast Sea Transportation*, pages 1193–1204, Vol. 2, Lübeck-Travemünde, Germany, September 1995.

- G. F. Clauss, E. Lehmann, and C. Östergaard. *Meerestechnische Konstruktionen*. ISBN 3-540-18964-5. Springer Verlag, Berlin, 1988.
- G. F. Clauss and U. Steinhagen. Numerical simulation of nonlinear transient waves and its validation by laboratory data. In *Proceedings of 9th International Offshore and Polar Engineering Conference (ISOPE)*, volume III, pages 368–375, Brest, France, 1999.
- G. F. Clauss and U. Steinhagen. Optimization of transient design waves in random sea. In *Proceedings of 10th International Offshore and Polar Engineering Conference (ISOPE)*, volume III, pages 229–236, Seattle, USA, 2000.
- G. F. Clauss, K. Stutz, and C. E. Schmittner. Rogue Wave Impact on Offshore Structures. In *Offshore Technology Conference*, Houston, Texas, USA, 2004c. OTC 16180.
- I. Daubechies. Orthonormal bases of compactly supported wavelets. *Communications on Pure and Applied Mathematics*, 41:909–996, 1988.
- R. G. Dean and R. A. Dalrymple. *Water wave mechanics for engineers and scientists*, volume 2 of *Advanced Series on Ocean Engineering*. World Scientific, 2000.
- WAMIT. *WAMIT Version 5.1 – A Radiation-Diffraction Panel Program For Wave-Body Interactions*. Department of Ocean Engineering, MIT, 1994. Userguide.
- Det Norske Veritas. Rules for Classification of Ships. Electronic Rulebook, 2000.
- Det Norske Veritas. Offshore Standard DNV-OS-C102, Structural Design of Offshore Ships, April 2004.
- R. van Dijk. Venturing into the deep with DP-FPSO. *MARIN Report*, (79), April 2003.
- R. van Dijk. Extreme conditions no problem; DP FPSO study proves a success. *MARIN Report*, (82), March 2004.
- D. Faulkner. Rogue Waves – Defining their Characteristics for Marine Design. In *Rogue Waves 2000*, Brest, France, 2000.
- D. Faulkner. Freak waves. *Navigation News*, pages 7–10, July-August 2003.

- Fluent. *FLUENT 6.1 User's Guide*. Fluent Inc., New Hampshire, USA, 2003.
- N. Fonseca and C. Guedes Soares. Nonlinear Wave Induced Responses of Ships in Irregular Seas. In *OMAE 1998 - 17th International Conference on Offshore Mechanics and Arctic Engineering*, Lisbon, Portugal, 1998a. OMAE 98-0446.
- N. Fonseca and C. Guedes Soares. Time-Domain Analysis of Large-Amplitude Vertical Motions and Wave Loads. *Journal of Ship Research*, 42(2):100–113, 1998b.
- N. Fonseca and C. Guedes Soares. Comparison of Numerical and Experimental Results of Nonlinear Wave-Induced Vertical Ship Motions and Loads. *Journal of Marine Science and Technology*, 6:139–204, 2002.
- N. Fonseca, C. Guedes Soares, and R. Pascoal. Prediction of Ship Dynamic Loads in Heavy Weather. In *RINA Design and Operation for Abnormal Conditions II*, pages 169–182, London, UK, 2001.
- S. González Sánchez, N. González Prelicic, and S. García Galán. *UviWave, Wavelet Toolbox for use with Matlab*. Departamento de TecnoloXías das Comunicacóns. Universidade de Vigo, Vigo, second edition, 1996.
- P. Gorf. FPSO concept increasingly popular. *MARIN Report*, (82), March 2004.
- C. Guedes Soares, Z. Cherneva, and E. M. Antão. Abnormal Waves during the Hurricane Camille. *Journal of Geophysical Research*, 2004a.
- C. Guedes Soares, Z. Cherneva, and E. M. Antão. Characteristics of Abnormal Waves in North Sea Storm Sea States. *Applied Ocean Research*, 2004b.
- C. Guedes Soares, N. Fonseca, and R. Pascoal. Experimental and Numerical Study of the Motions of a Turret Moored FPSO in Waves. In *OMAE 2001 - 20th Conference on Offshore Mechanics and Arctic Engineering*, Rio de Janeiro, Brasil, 2001. OMAE2001/OFT-1071.
- S. Haver and O. J. Anderson. Freak Waves: Rare Realization of a Typical Population or Typical Realization of a Rare Population? In *Proceedings of the 10th International Offshore and Polar Engineering Conference (ISOPE)*, pages 123–130, Seattle, USA, 2000.

- J. Hennig. Generation and Analysis of Harsh Wave Environments. *Dissertation*, Technische Universität Berlin (D 83), 2005.
- ICCM. *COMET VERSION 2.0 USER MANUAL*. ICCM Institute of Computational Continuum Mechanics GmbH, Hamburg, Germany, 2001.
- ISO. Petroleum and natural gas industries - Specific requirements for offshore structures - Part 1: Metocean design and operating conditions. Technical Report ISO/DIS 19901-1, 2003.
- P. Jonathan, P. H. Taylor, and P. S. Tromans. Storm waves in the northern north sea. In *Proceedings of the International Conference on Behaviour of Offshore Structures (BOSS)*, pages 481–495, Boston, 1994.
- J. M. J. Journee. Theoretical Manual of SEAWAY. Report no. 1216, Delft University of Technology, Ship Hydromechanics Laboratory, Mekelweg 2, 2628 CD Delft, Netherland, 2000.
- S. P. Kjeldsen. Determination of severe wave conditions for ocean systems in a 3-dimensional irregular seaway. In *Contribution to the VIII Congress of the Pan-American Institute of Naval Engineering*, pages 1–35, 1983.
- S. P. Kjeldsen. Breaking waves. In A. Tørum and O.T. Gudmestad, editors, *Proceedings of the NATO Advanced Research Workshop on Water Wave Kinematics*, pages 453–473, Molde, Norway, 1990. Kluwer Academic Publishers, Dordrecht. NATO ASI Series, Series E - Volume 178.
- W.L. Kühnlein, G.F. Clauss, and J. Hennig. Tailor Made Freak Waves Within Irregular Seas. In *OMAE 2002 - 21st Conference on Offshore Mechanics and Arctic Engineering*, Oslo, 2002. OMAE2002-28524.
- A. MacMillan. Effective FPSO/FSO Hull Structural Design. In *Offshore Technology Conference*, Houston, Texas, USA, 2001. OTC 13212.
- N. Mori, T. Yasuda, and S. Nakayama. Statistical Properties of Freak Waves Observed in the Sea of Japan. In *Proceedings of the 10th International Offshore and Polar Engineering Conference (ISOPE)*, volume 3, pages 109–122, Seattle, USA, 2000.
- J. N. Newman. Algorithms for the free-surface green function. *Journal of Engineering Mathematics*, 19:57–67, 1985.
- J. N. Newman. Wave effects on deformable bodies. *Applied Ocean Research*, 16:47–59, 1994.

- NORSOK. Standard - actions and action effects. Technical Report N-003, 2004.
- T. Nutter and P. E. Albaugh. 2004 Worldwide Survey of Floating Production Storage and Offloading (FPSO) Units. *Offshore Magazine*, (ISSN 0030-0608), September 2004.
- C. Östergaard and T. E. Schellin. Comparison of experimental and theoretical wave actions on floating and compliant offshore structures. volume 9, pages 192–213, 1987.
- T. Rowan. *Functional Stability Analysis of Numerical Algorithms*. PhD thesis, University of Texas at Austin, 1990.
- S. E. Sand, H. N. E. Ottesen, P. Klinting, O. T. Gudmestadt, and M. J. Sterndorff. *Freak Wave Kinematics*, pages 535–549. Kluwer Academic Publisher, NATO ASI Series edition, 1990.
- M. Schulz. "Ich spürte den Atem Gottes". *Der Spiegel*, December 2001. No. 51/2001.
- U. Steinhagen. Synthesizing nonlinear transient gravity waves in random seas. *Dissertation*, Technische Universität Berlin (D 83), 2001.
- N. Terdre. Frigg contract entrusts Aker Kvaerner with biggest removal project yet. *Offshore Magazine*, (ISSN 0030-0608):82–84, May 2005.
- T. Terpstra, B. B. d’Hautefeuille, and A. MacMillan. FPSO Design and Conversion: A Designer’s Approach. In *Offshore Technology Conference*, Houston, Texas, USA, 2001. OTC 13210.
- The Institute of Measurement and Control. *Guide to the Measurement of Force*. The Institute of Measurement and Control, London, UK, 1998.
- D. W. Wang, D. A. Mitchel, W. J. Teague, E. Jarosz, and M. S. Hulbert. Extreme Waves under Hurricane Ivan. *SCIENCE*, 309, August 2005.
- K. Wendel. Hydrodynamische Massen und hydrodynamische Massenträgheitsmomente. In *Jahrbuch der Schiffbautechnischen Gesellschaft*, pages 207–255, 1955.
- J.-H. Westhuis. *The Numerical Simulation of Nonlinear Waves in a Hydrodynamic Model Test Basin*. PhD thesis, Universiteit Twente, Enschede, MARIN, Wageningen (ISBN: 90-365-1575-0), 2001.

- Jaap de Wilde. Storms and even hurricanes no problem for Atlantis PQ semi. *MARIN Report*, (79), April 2003.
- J. Wolfram, B. Linfoot, and P. Stansell. Long- and short-term extreme wave statistics in the North Sea: 1994-1998. In *Rogue Waves 2000*, pages 363–372, Brest, France, 2000.
- G. X. Wu and R. Eatock-Taylor. Finite element analysis of two-dimensional non-linear transient water waves. *Applied Ocean Research*, (16):363–372, 1994.

Nomenclature

A_{column}	[m ²]	cross section area of column
B	[m]	breadth
C_0	[-]	Biésel transfer function
E	[Nm]	wave energy
EI_y	[Nm ²]	flexural stiffness
F	[N]	force
F_{column}	[N]	horizontal force on one column
$F_{comp.}$	[N]	compression force
F_{drag}	[N]	drag force
$ F_{exp} _{max}$	[N]	maximum absolut value of measured splitting forces
$F_{external}$	[N]	horizontal force the semisubmersible
F_{hull}	[N]	horizontal force on one hull
$F_{inertia}$	[N]	inertia forc
$F_{Morison}$	[N]	Morison force
F_n	[-]	Froude number
$F_{oneside}$	[N]	horizontal force on one side
F_{sig}	[N]	significant splitting force
$F_{sig,max}$	[N]	maximum significant splitting force
F_{splitt}	[N]	splitting force
$F_{splitting}$	[N]	splitting force
$F_{tension}$	[N]	tension force
H	[m]	wave height
H_i	[m]	height of the i^{th} wave
H_{max}	[m]	maximum wave height
H_{max100}	[m]	maximum wave height within a 100 year storm
$H_{max10000}$	[m]	maximum wave height within a 10000 year storm
H_s	[m]	significant wave heigth
H_{target}	[m]	target wave heigth

L	[m]	wave length
L_{oa}	[m]	length over all
L_{pp}	[m]	length between perpendiculars
L_{target}	[m]	target wave length
M	[Nm]	bending moment
M_b	[Nm]	bending moment
$ M_{exp} _{max}$	[Nm]	maximum absolut value of measured bending moment
$M_{hogging}$	[Nm]	hogging moment
$M_{hogg,max}$	[Nm]	maximum measured hogging moment
M_{max}	[Nm]	maximum bending moment
$M_{sagging}$	[Nm]	sagging moment
$M_{sagg,max}$	[Nm]	maximum measured sagging moment
M_{sig}	[Nm]	significant bending moment
$M_{sig,max}$	[Nm]	maximum significant bending moment
N	[-]	number of waves
P	[W]	power
P_i	[-]	Legendre polynomials
$P_{m_{add}}$	[W]	power for acceleration of added mass
P_{max}	[W]	maximum power
P_{mov}	[W]	power for acceleration of moving parts
RAO_{airgap}	[m/m]	transfer function of variation in airgap
RAO_{s_3}	[m/m]	transfer function of heave motion
$RAO_{forces\ horizontal}$	[N/m]	transfer function of horizontal exciting forces
$RAO_{forces\ side\ 1}$	[N/m]	transfer function of forces on side one
$RAO_{forces\ side\ 2}$	[N/m]	transfer function of forces on side two
$RAO_{splitting\ forces}$	[N/m]	transfer function of splitting forces
RAO_{ζ}	[m/m]	transfer function of the wave
S_{airgap}	[m ² s]	response spectrum of airgap
S_M	[N ² m ² s]	response spectrum of bending moments
S_{s3}	[m]	response spectrum of heave motion
S_{s5}	[m]	response spectrum of pitch motion
S_{splitt}	[N ² s]	response spectrum of splitting forces
S_{ζ}	[m ² s]	wave energy density spectrum
T	[m]	Draft
T	[s]	period
T_0	[s]	zero-upcrossing period
T_i	[s]	period of the i^{th} wave
T_p	[s]	peak period
T_{target}	[s]	target wave period
V	[m ³]	volume

V_{hull}	[m ³]	volume of hull
W	[Nm]	work
a	[m]	wave amplitude
\bar{a}	[m]	wave board stroke
a_m	[m]	wave board amplitude
a_{max}	[m ² /s]	maximum wave board acceleration
a_{new}	[rad/s]	new amplitudes of component waves
a_{old}	[rad/s]	old amplitudes of component waves
$a_{recorded}$	[rad/s]	recorded amplitudes of component waves
a_{target}	[rad/s]	target amplitudes of component waves
$airgap_a$	[m]	amplitude of airgap variation
$airgap_{sig}$	[m]	significant airgap
b_0	[m]	distance between hulls
c	[°]	phase angles
c^3	[-]	wavelet approximation coefficients
c_a	[-]	added mass coefficient
c_B	[-]	block coefficient
c_{gr}	[m/s]	group velocity
c_m	[-]	inertia coefficient
$c_{m_{column}}$	[-]	inertia coefficient of column
$c_{m_{hull}}$	[-]	inertia coefficient of submerged hull
c_w	[-]	wave coefficient
$c_{wavelet}$	[-]	wavelet coefficients
d	[m]	water depth
$d^1 \dots d^3$	[-]	wavelet detail coefficients
dt	[s]	time step size
$f_1 \dots f_4$	[-]	function values
f_j	[-]	function values
f_m	[-]	measure of merit
g	[m/s ²]	gravitational acceleration
h_c	[m]	draft of columns
h_h	[m]	draft of hull
h_{hinge}	[m]	height of hinge above bottom
i	[-]	index
j	[-]	index
k	[1/m]	wave number
m	[kg]	mass
m_{add}	[kg]	hydrodynamic or added mass
n	[-]	index
n	[-]	number of target parameters
s_3	[m]	heave motion

s_{3a}	[m]	heave motion amplitude
$ s_{3,exp} _{max}$	[m]	maximum absolut value of measured heave motion
$s_{3,exp,max}$	[m]	maximum measured heave motion
$s_{3,exp,min}$	[m]	minimum measured heave motion
$s_{3,sig}$	[m]	significant amplitude of heave motion
$s_{3,sig,max}$	[m]	maximum significant heave motion
s_5	[°]	pitch motion
s_5a	[°]	pitch motion amplitude
$ s_{5,exp} _{max}$	[°]	maximum absolut value of measured pitch motion
$s_{5,exp,max}$	[°]	maximum measured pitch motion
$s_{5,exp,min}$	[°]	minimum measured pitch motion
$s_{5,sig}$	[°]	significant amplitude of pitch motion
$s_{5,sig,max}$	[°]	maximum significant pitch motion
$s_{7,sig}$	[m]	significant amplitude of airgap variation
$ s_{7,exp} _{max}$	[m]	maximum absolut value of variation in airgap
$s_{7,exp,max}$	[m]	maximum measured variation in airgap
$s_{7,exp,min}$	[m]	minimum measured variation in airgap
$ s_{exp} _{max}$	[-]	maximum absolut value of measured response
$s_{exp,max}$	[-]	maximum measured amplitude
$s_{exp,min}$	[-]	minimum measured amplitude
s_{sig}	[-]	significant amplitude
$s_{sig,max}$	[-]	maximum significant amplitude
s_{ia}	[m]	amplitude of deflection
t	[s]	time
t_i	[s]	time of occurrence of the i^{th} wave
u_{max}	[m/s]	maximum wave board velocity
t_{target}	[s]	target time of occurrence
vbm	[Nm]	vertical bending moment
w_i	[m]	deflection line
w''	[1/m]	curvature of deflection line
x	[m]	horizontal space coordinate
x_B	[m]	wave board stroke
x_{max}	[m]	maximum wave board stroke
\dot{x}_B	[m/s]	wave board velocity
\ddot{x}_B	[m ² /s]	wave board accelaration
β	[°]	angle of wave encounter
γ	[-]	peak enhancement factor
γ_1	[-]	parameter for the Biésel transfer function

$\gamma_{1,flap}$	[-]	parameter for the Biésel transfer function of a flap type wavemaker
$\gamma_{1,piston}$	[-]	parameter for the Biésel transfer function of a piston type wavemaker
γ_2	[-]	parameter for the Biésel transfer function
ζ	[m]	surface elevation
ζ_a	[m]	wave amplitude
ζ_c	[m]	wave crest height
ζ_{ci}	[m]	crest height of the i^{th} wave
$\zeta_{c\,target}$	[m]	target wave crest height
λ	[-]	scale
ρ	[kg/m ³]	density
φ_{new}	[°]	new phase angles of component waves
φ_{old}	[°]	old phase angles of component waves
$\varphi_{recorded}$	[°]	recorded phase angles of component waves
φ_{target}	[°]	target phase angles of component waves
ω	[rad/s]	wave frequency
\mathfrak{S}	[W]	average energy flux
\mathfrak{S}_{max}	[W]	maximum energy flux
∇	[t]	Displacement

Abbreviations

3D	three dimensional
CFD	Computational Fluid Dynamics
DP-FPSO	Dynamically Positioned FPSO
FE	Finite Elements
FFT	Fast Fourier Transform
FPSO	Floating Production, Storage and Offloading Ship
HSVA	Hamburg Ship Model Basin
IACS	International Association of Classification Societies
JONSWAP	Joint North Sea Wave Project
LED	Light Emitting Diode
NWT	Numerical Wave Tank
NYW	New Year Wave
Pot	Potential theory
RANSE	Reynolds Averaged Navier-Stokes equations
RAO	Response Amplitude Operator
TUB	Technische Universität Berlin
VOF	Volume of Fluent method

WAMIT	Wave Analysis, developed at Massachusetts Institute of Technology
WAVETUB	Wave simulation code developed at Technical University Berlin

Optical System for the Registration of Motions

Within the scope of this thesis, various motion measurements are performed by a contact-free motion measuring system which applies standard video equipment. Not only the hardware setup, but also the algorithm is newly developed resulting in time series for three degrees of freedom. The advantage of an optical system in comparison to cable actuated position sensors is, that the system does not influence the motions of the examined structure, as the sensor has no physical connection to the model.

The implemented motion tracking algorithm, assumes that the model motion is two-dimensional. This premise is valid for the presented model tests in this thesis, since head seas and stern seas are considered, resulting in heave, surge and pitch motions. Excitation of roll motions during the model tests is minimized by the application of side wall wave absorbers. The developed motion capturing system consists of a digital video camera, optical markers mounted on the model and a personal computer with the implemented post processing software for analyzing the video sequences.

The digital video camera which records the measurement features a standard PAL-video resolution of 720x576 pixels at 25 frames per second. The measuring range of the video system can be adapted to the test purpose by variation of the distance between object and camera and adjustment of the focal length of the camera.

During the model tests, the digital video camera captures the motions of the markers on tape. For the investigation of surge, heave and pitch motions, two markers i. e. battery operated LEDs are attached to the model as shown in Fig. 1 for the semisubmersible *GVA 4000* and in Fig. 3.3 (chapter 4) for the FPSO. The markers are bright spots, that are clearly identifiable in comparison to the surrounding area. To calibrate the system, the distance between both markers has to be determined.



Figure 1: Active markers mounted on the model of the semisubmersible *GVA 4000*. The red LEDs are easy detectable by the motion tracking algorithm since they are surrounded by a black area giving a high contrast.

When the model tests are completed, the recorded video sequences are transferred into the computer via a firewire interface (IEEE1394) in a first post processing step and afterwards converted into uncompressed audio video interleaved (avi) files with 24bit color depth. The video sequences can then be analyzed by the implemented tracking algorithm. Briefly, this algorithm comprises the following steps:

- The first frame of the video sequence to be analyzed is loaded into the memory and shown on the screen. The user defines by mouse clicks into the picture which markers are to be tracked.
- Based on the definition of the starting points, the brightest spots in each surrounding area are searched and stored as x- and y-coordinates for the first frame.
- The next frame is loaded into the memory and based on the old marker position a new search for the brightest spot in the surrounding of this position is performed resulting in new positions for the markers.
- From the third frame on, the search radius is adapted, i. e. the area where the search for the markers is performed, based on the velocity obtained from the coordinates of the last two frames. Thus, the new marker positions can be found fast and reliably.
- The search continues until the last frame of the video sequence is reached.

The number of markers is not restricted in general, but in practice, the distance between two markers should be as large as possible. To synchronize the video system with the computer – which is both, steering the wave generator as well as measuring the wave elevations and loads – a third LED is positioned within the field of view of the camera. The LED is switched off when the experiment starts, which gives a clearly instance of the start in the video registration. The tracking system has been successfully validated against cable actuated position sensors for various test cases. Based on the coordinates of the markers obtained for each frame, the program calculates the surge, heave and pitch motions that are presented throughout this thesis.

Registration of Forces and Moments

In order to register structural loads during the model tests, elastic load bearing elements are applied. These are deflected if a force or moment is applied to them and the distortion is sensed by transducers, so-called strain gauge load cells, that are based on elastic elements (foil) with attached loops of wire. If the strain element is deflected, the length of the wire increases with corresponding decrease in its diameter and change of its electrical resistance. To increase the response of the load cell and to minimize the effects of environmental changes, four strain gauges are arranged in a wheatstone bridge configuration. The voltage output of the bridge is linearly related to the resistance change of the strain gauges and is therefore a function of the load applied to the element (The Institute of Measurement and Control (1998)).

The strain elements applied are built as double bending beams from stainless steel, as this material is insensitive to corrosion and exhibits a linear relation between stress and strain, a low hysteresis as well as a low creep in the working range. If a force is applied to the double bending beam as presented in Fig. 2, the free end of the beam is displaced translatorily. Strain gauges A and D are tensed and strain gauges B and C are compressed resulting in a differential voltage across the wheatstone bridge.

If a moment acts on the load cell, the beam is bend and strain gauges C and D are compressed, whereas strain gauges A and B are tensed (Fig. 3). These two different modes of deformation allow for the construction of force transducers that measure forces independently of the applied moment as well as – vice versa – moment transducers for the registration of moments independently of the applied force. This can be achieved by rearranging the strain gauges in the wheatstone bridge.

Fig. 2 gives the configuration of the strain gauge resistances within the wheatstone bridge for the registration of forces and Fig. 3 for the registration of

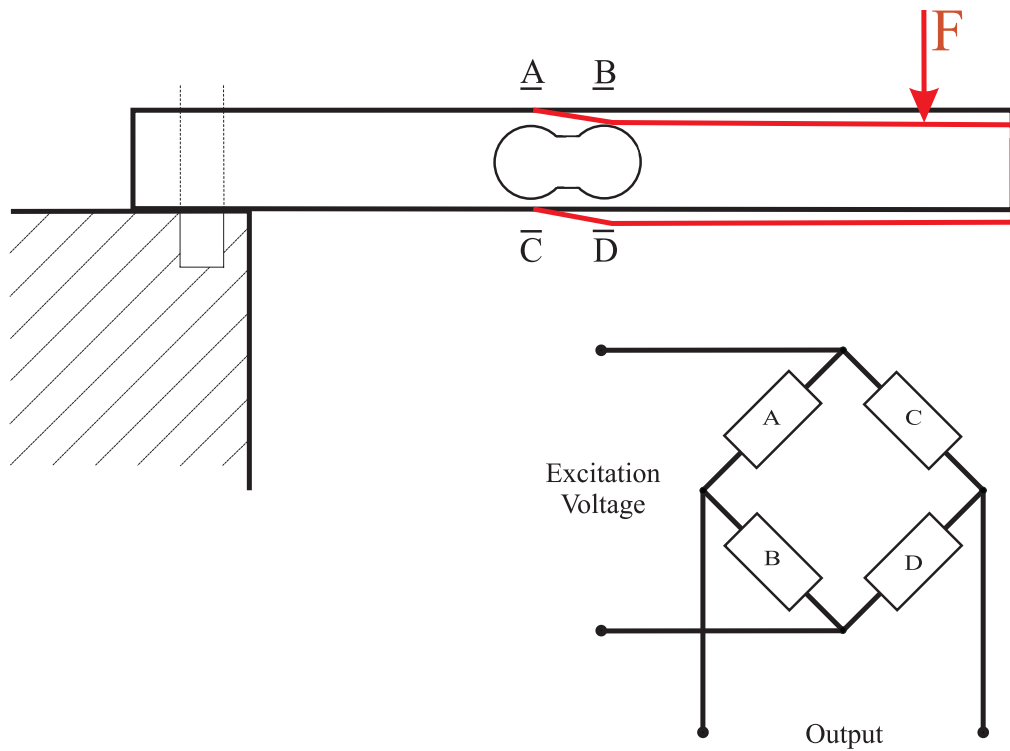


Figure 2: Deflection of force and moment transducer and arrangement of resistive type strain gauges in a wheatstone bridge configuration for force measurement.

moments. With the latter configuration, the bending moments of the FPSO and of the crane vessel are registered, as presented in chapter 4.

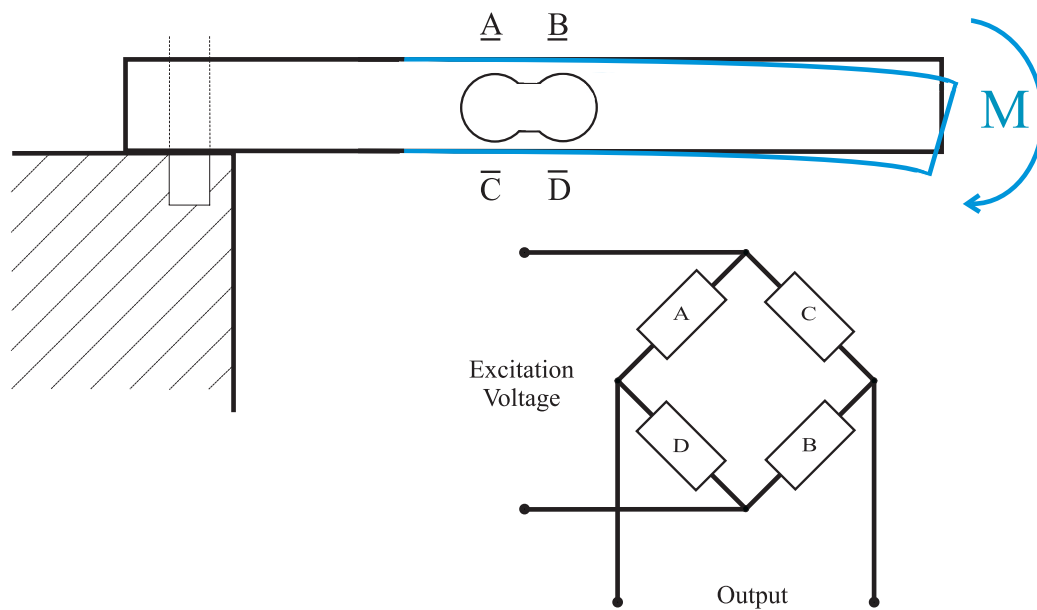


Figure 3: Deflection of force and moment transducer and arrangement of resistive type strain gauges in a wheatstone bridge configuration for the measurement of bending moments. Along the different arrangement of the strain gauges in the wheatstone bridge makes the difference between moment and force transducer.

Design of a Wave Maker for the Small Wave Tank at TUB

In general, many kinematics are applied to generate waves in a basin (Biésel and Suquet (1951)), where the five mechanics shown in Fig. 4 are of practical relevance. These are namely:

- Piston type, moving the wave board translatorily, which is applied in particular for the generation of shallow water waves,
- Flap type, with rotational kinematics,
- Duplex type, as a combination of flap and piston type,
- Double flap, with the upper flap for the generation of rather short waves and the main flap for the generation of longer waves,
- Plunger type, with a translatorily up and down moving wedge.

For the piston type wave board, the velocity profile is constant with depth which is beneficial for the generation of shallow water waves. Deep water waves are best generated by a flap or even double flap wave generator.

The most common way of actuation for wave generators is electrical for smaller installations, and hydraulical for large facilities. The back side of the wave generator can be dry, which requires sealings at the side and the bottom of the wave paddle, or wet, which is easier to build with the drawback that waves are also generated on the back side of the board.

In the following, basic principles for the design of a piston type wave maker for the small wave tank at TUB are described and the power requirement is determined based on linear wave theory. The maximum wave height H that can be generated is restricted by the wave breaking limit as given e. g. by Clauss et al. (1988):

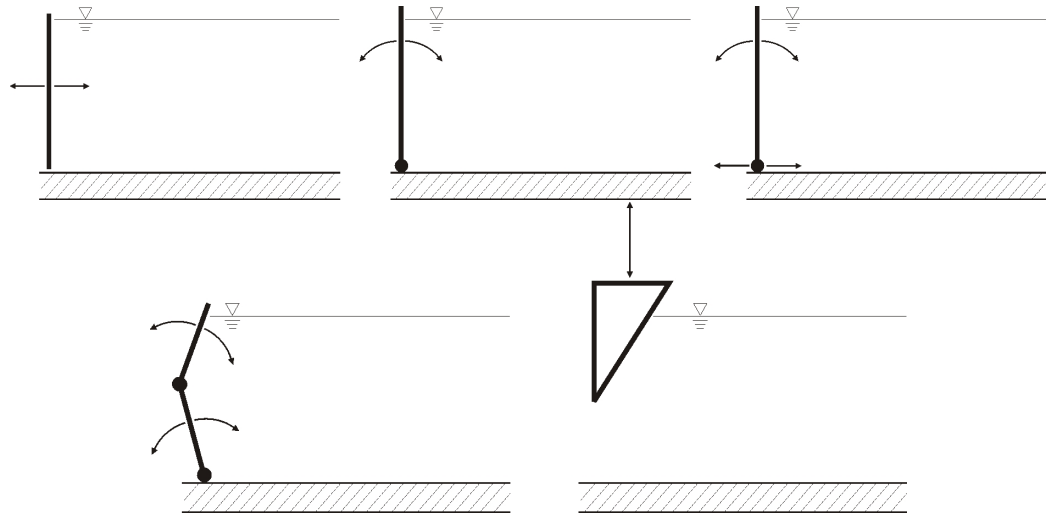


Figure 4: Most common types of wave generators: Piston type, flap type, duplex type, double flap type and plunger type (from left to right, top to bottom).

$$\left(\frac{H}{L}\right)_{max} = 0.142 \cdot \tanh kd, \tag{1}$$

with wave length L and water depth d . For transitional water depth ($0.04 < \frac{d}{L} < 0.5$) the wave number k is determined by the dispersion relation:

$$kd \tanh kd = \frac{\omega^2}{g}d, \tag{2}$$

where ω denotes the wave frequency and g the gravitational acceleration. In Fig. 5, the maximum wave height depending on wave frequency for a water depth of 0.4 m is shown (blue line). For the piston type wave generator to be designed, the maximum reasonable wave height to be generated is 0.2 m due to the height of the side walls of the wave basin (red line).

The wave amplitude a is related to the wave board stroke \bar{a} by the Biésel transfer function C_0 as proposed by Biésel and Suquet (1951):

$$\bar{a} = C_0 \cdot a \tag{3}$$

with the Biésel function itself as given by Westhuis (2001):

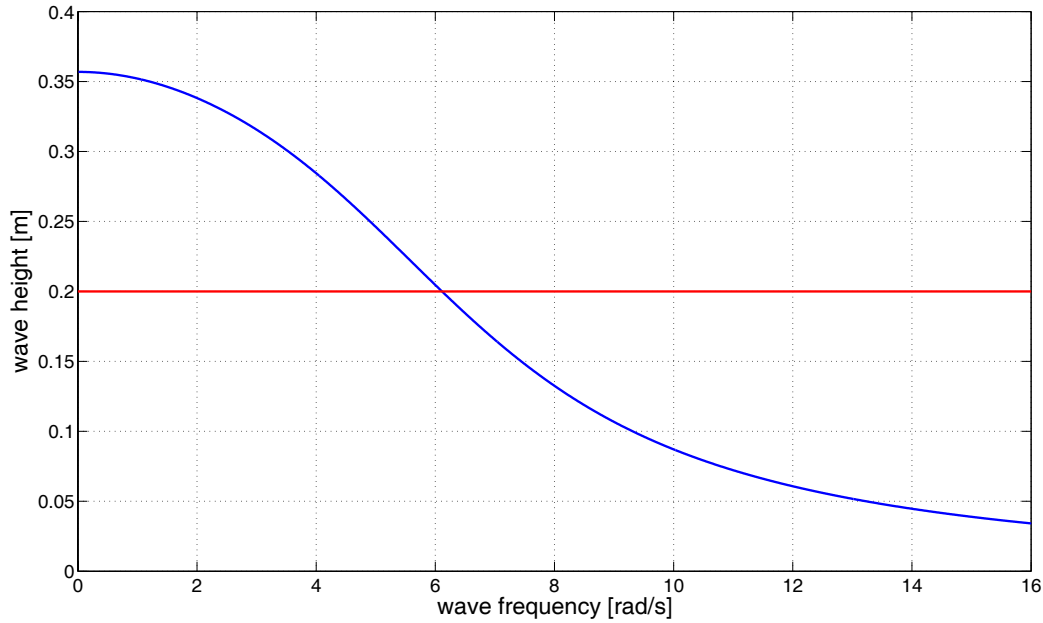


Figure 5: Maximum wave height restricted by the wave breaking limit depending on wave frequency for a water depth of 0.4 m (blue line). The maximum feasible wave height is smaller than the water depth. The red line gives the maximum reasonable wave height for the small wave tank at TUB.

$$C_0 = \sinh kd \cdot \frac{\gamma_1}{\gamma_2} \quad (4)$$

with parameter $\gamma_{1,piston}$ for piston type:

$$\gamma_{1,piston} = \sinh kd, \quad (5)$$

and parameter $\gamma_{1,flap}$ for flap type:

$$\gamma_{1,flap} = \sinh kd + \frac{(\cosh kh_{hinge} - \cosh kd)}{(d - h_{hinge})k}. \quad (6)$$

The parameter γ_2 is given by:

$$\gamma_2 = \frac{1}{2}(kd + \sinh kd \cdot \sinh kd), \quad (7)$$

where h_{hinge} denotes the height of the hinge above the bottom. Fig. 6 presents the Biésel functions for the new piston type as well as the new flap type wave generator at TUB for a water depth of 0.4 m.

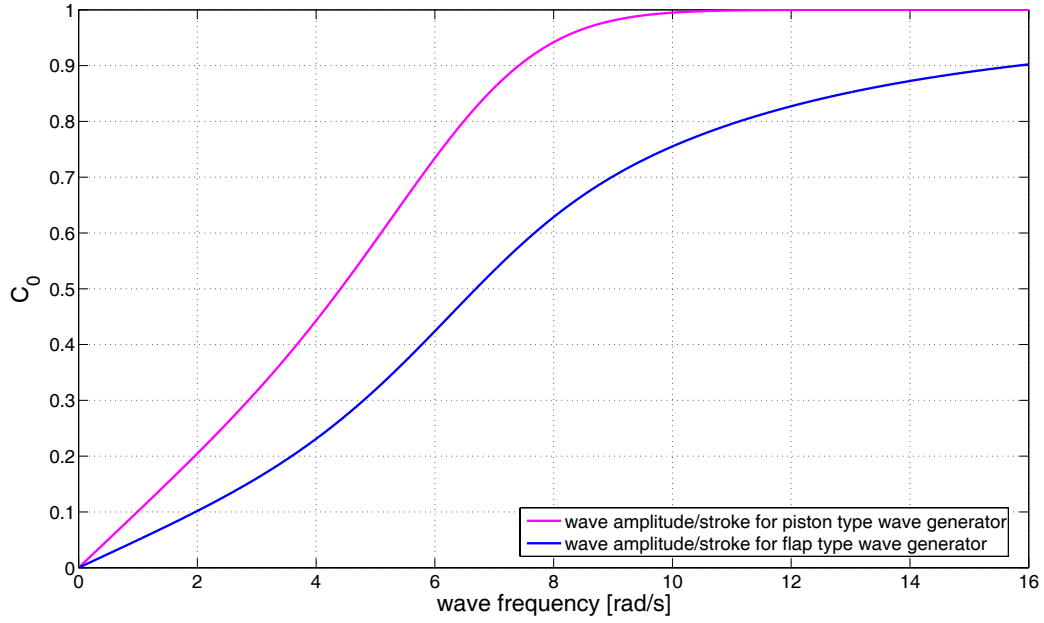


Figure 6: Biésel transfer function for the piston type (magenta line) as well as the flap type (blue line) wave generator for the small wave tank at TUB for a water depth of 0.4 m. With identical stroke, the piston type wave board generates larger waves due to the constant velocity profile over depth bringing more energy into the water.

Applying the Biésel transfer function for a given wave height, the corresponding stroke can be determined. For the piston type wave generator, Fig. 7 gives the stroke amplitude for the generation of the wave heights given in Fig. 5. The bend in the curve at $\omega = 6.1$ rad/s results from the maximum wave height of 0.2 m which refers to the wall height of the wave basin. For higher frequencies, the wave height and consequently the stroke of the wave board is restricted by the wave breaking limit. Nevertheless, for long waves, the stroke goes to infinity and is therefore limited to a maximum amplitude of 0.1 m.

In consequence, waves with periods larger than 1.53 s, i. e. with a wave length larger 2.68 m, cannot be generated up to 0.2 m wave height. Fig. 8 gives the maximum wave heights depending on the wave frequency that can be generated in the basin.

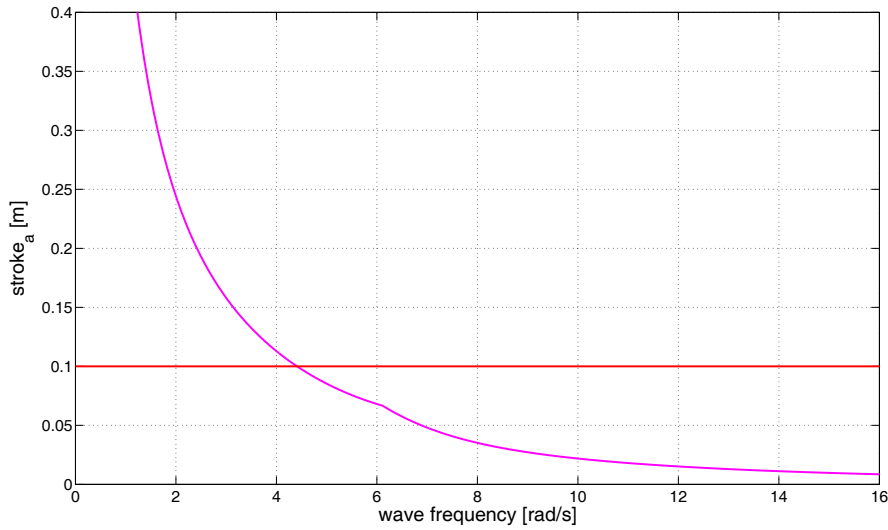


Figure 7: Stroke amplitude of the piston type wave maker. For the generation of long waves the stroke goes to infinity and is therefore restricted to 0.1 m.

Based on the maximum stroke of the wave board the power requirement of the wave maker can be assessed. It consists of three parts:

- Wave energy,
- Energy required for accelerating the moving parts of the wave board,
- Energy required for accelerating the hydrodynamic mass of the wave board.

Generated waves transport energy away from the board. The rate at which the energy is transferred – the average energy flux \mathfrak{S} – is the product of the total energy per wave and per unit width E , and the group velocity c_{gr} :

$$\mathfrak{S} = E \cdot c_{gr}. \quad (8)$$

For transitional water depth the group velocity is:

$$c_{gr} = \frac{1}{2} \sqrt{\frac{g}{k} \tanh kd} \cdot \left(1 + \frac{2kd}{\sinh 2kd}\right), \quad (9)$$

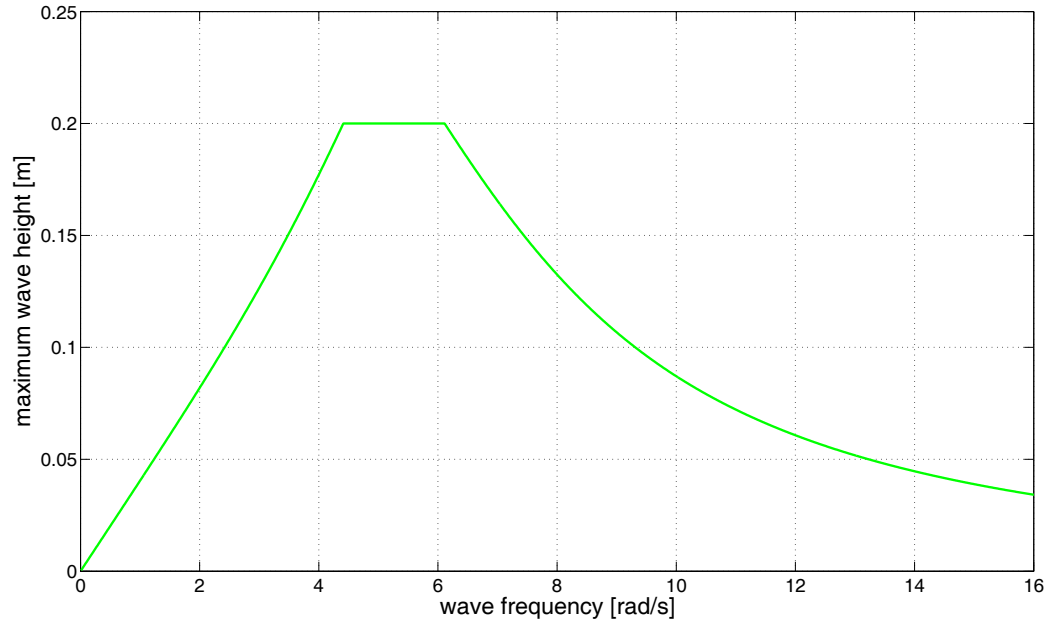


Figure 8: Maximum wave height that can be generated in the small wave tank by the piston type wave generator with a maximum stroke amplitude of 0.1 m.

and the total wave energy per unit surface area according to Dean and Dalrymple (2000) is:

$$E = \frac{1}{8} \rho g H^2, \quad (10)$$

with fluid density ρ . The maximum wave energy flux is determined by Clauss et al. (1988):

$$\mathfrak{S}_{max} = 1.5 \cdot \mathfrak{S}. \quad (11)$$

Beside the energy transported away from the wave board by the wave itself, the wave board as well as the hydrodynamic mass have to be accelerated and decelerated. Assuming a sinusoidal motion of the wave board, the motion is described as:

$$x(t) = a_m \cdot \sin \omega t. \quad (12)$$

Twice differentiating gives the acceleration of the wave board:

$$\ddot{x}_B(t) = -a_m \omega^2 \cdot \sin \omega t. \quad (13)$$

The work required to actuate the wave board is the actuation force F multiplied by distance: $W(t) = F(t) \cdot x(t)$, with $F(t) = m \cdot \ddot{x}_B(t)$, where m denotes the sum of the moving masses:

$$W(t) = -a_m^2 \omega^2 m \cdot \sin^2 \omega t. \quad (14)$$

By differentiation, the time dependent power can be deduced:

$$P(t) = -a_m^2 \omega^3 m \cdot 2 \sin \omega t \cos \omega t, \quad (15)$$

and the maximum power follows from extreme value analysis:

$$P_{max} = -a_m^2 \omega^3 m. \quad (16)$$

The mass of the mechanics is obtained by weighting of the components and the hydrodynamic or added mass m_{add} is estimated as the water mass under half a wave length:

$$m_{add} = \frac{1}{2} L B d \rho, \quad (17)$$

with B the width of the basin. As the added mass is of large order, it is important not to underestimate this dimension for the design of a wave generator. Therefore, measurements are performed to document that the given estimation of the added mass is sufficient. Fig. 9 gives the calculated and measured added mass depending on the wave frequency. For longer waves, the added mass is many times larger than the mass of the wave board mechanics. In addition, for a wave generator with wet back the hydrodynamic mass has to be considered twice, as water has to be accelerated on both sides of the board.

Now, the maximum power required P_{max} for actuation of the wave board can be derived. Fig. 10 presents a design power diagram for the piston type wave generator installed in the small wave basin. From the maximum wave height given in Fig. 8, the maximum power for the generation of the wave is derived (cyan line). The power required to accelerate the moving parts P_{mov} of the wave maker is given by the green line. Both power requirements are small

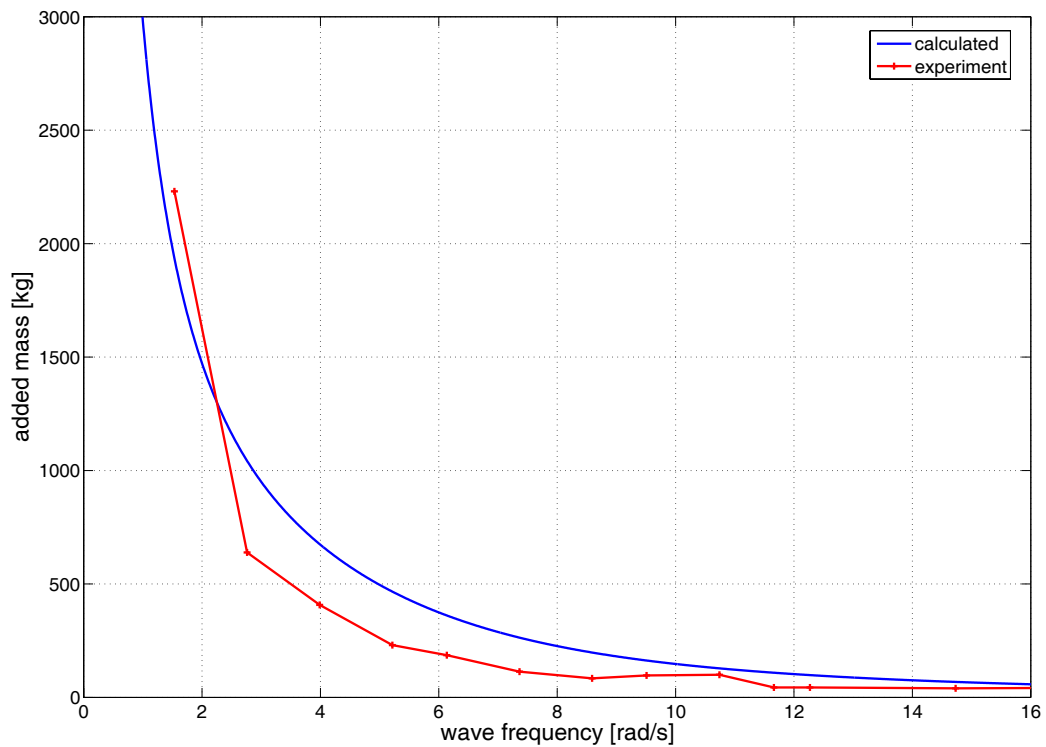


Figure 9: Added mass for the small wave tank at TUB. For small waves the added mass becomes dramatically large, resulting in an enormous power requirement for wave generation.

in comparison to the power needed for the acceleration and deceleration of the added mass $P_{m_{add}}$ (blue line). Thus, the power requirement for the wave generator is mainly depending on the dimension of the added mass. The total power is deduced as the sum of all three contributions. The maximum power is required at the turning points, when accelerations and forces are at a maximum. Based on the maximum power, a driving mechanism can be designed and an adequate driving motor is selected.

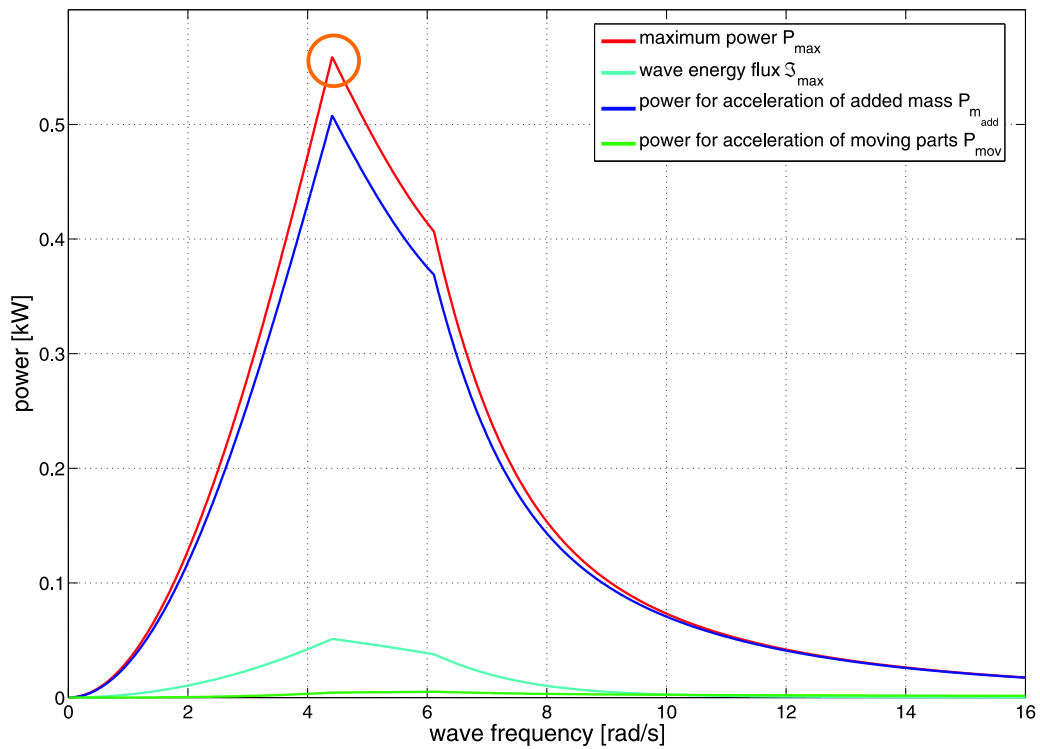


Figure 10: Design power diagram for the wet back piston type wave generator at the small wave tank of TUB with a water depth of 0.4 m and a tank width of 0.3 m. In consequence, the minimum required engine power of the electrical motor is 560 W indicated by the orange circle.